8-2010

Estimation and Control of Robotic Radiation-Based Processes

Fan Zeng
Clemson University, zengfan00@gmail.com

ESTIMATION AND CONTROL OF ROBOTIC RADIATION-BASED PROCESSES

A Dissertation
Presented to
the Graduate School of
Clemson University

In Partial Fulfillment
of the Requirements for the Degree
Doctor of Philosophy
Automotive Engineering

---

by
Fan Zeng
August 2010

Accepted by:
Dr. Beshahwired Ayalew, Committee Chair
Dr. Thomas R. Kurfess
Dr. Todd H. Hubing
Dr. Ardalan Vahidi
Dr. Mohammed A. Omar

ABSTRACT

This dissertation presents a closed-loop control and state estimation framework for a class of distributed-parameter processes employing a moving radiant actuator. These radiation-based processes have the potential to significantly reduce the energy consumption and environmental impact of traditional industrial processes. Successful implementation of these approaches in large-scale applications requires precise control systems. This dissertation provides a comprehensive framework for: 1) integration of trajectory generation and feedback control, 2) online distributed state and parameter estimation, and 3) optimal coordination of multiple manipulated variables, so as to achieve elaborate control of these radiation-based processes for improved process quality and energy efficiency.

The developed framework addresses important issues for estimation and control of processes employing a moving radiant actuator from both practical and theoretical aspects. For practical systems, an integrated motion and process control approach is first developed to compensate for disturbances by adjusting either the radiant power of the actuator or the speed of the robot end effector based on available process measurements, such as temperature distribution. The control problem is then generalized by using a 1D scanning formulation that describes common characteristics of typical radiant source actuated processes. Based on this 1D scanning formulation, a distributed state and parameter estimation scheme that incorporates a dual extended Kalman filter (DEKF) approach is developed to provide real-time process estimation. In this estimation scheme, an activating policy accompanying the moving actuator is applied in order to reduce the

computational cost and compensate for observability changes caused by the actuator's movement. To achieve further improvements in process quality, a static optimization and a rule-based feedback control strategy are used to coordinate multiple manipulated variables in open-loop and closed-loop manners. Finally, a distributed model predictive control (MPC) framework is developed to integrate process optimization and closed-loop coordination of manipulated variables. Simulation studies conducted on a robotic ultraviolet (UV) paint curing process show that the developed estimation and control framework for radiant source actuated processes provide improved process quality and energy efficiency by adaptively compensating for disturbances and optimally coordinating multiple manipulated variables.

DEDICATION

I dedicate this work to my dear parents and to the love of my life, Dandi, for their continuous and unconditional supports.

ACKNOWLEDGMENTS

I would like to acknowledge the continuous support and guidance from my academic advisor Dr. Beshahwired Ayalew during my three years Ph. D. studies. His professional direction and enthusiastic enlightenment enable me to achieve my desired academic and ideological objectives. I would also like to offer my sincerest thanks to my advisory committee members, Dr. Thomas R. Kurfess, Dr. Todd H. Hubing, Dr. Aradalan Vahidi, and Dr. Mohammed A. Omar for their helpful suggestions.

I would also like to acknowledge the support of Dr. Igor Luzinov and Dr. Guzeliya Korneva from the School of Material Science and Engineering at Clemson University. Their helpful suggestions and direct supports allow me to complete the essential sample tests included in the experiment part of this dissertation.

I would like to offer my special thanks to my fellow laboratory collaborators at Clemson University - International Center for Automotive Research for their continuous assistance and encouragement in every step I took to develop the experimental platform for this research work.

TABLE OF CONTENTS

Page

TITLE PAGE i

ABSTRACT ii

DEDICATION iv

ACKNOWLEDGMENTS v

LIST OF TABLES viii

LIST OF FIGURES ix

CHAPTER

1. INTRODUCTION 1

    1.1 Research Motivation 1
    1.2 Problem Statement 3
    1.3 Objectives and Contributions 5
    1.4 Dissertation Overview 6

2. REVIEW OF RELATED WORK 8

    2.1 Control Strategies for Processes Employing Moving Actuators 8
    2.2 Estimation Methods for Distributed-Parameter Processes 13
    2.3 Model Predictive Control for Distributed-Parameter Processes 18

3. ONLINE TRAJECTORY GENERATION AND FEEDBACK CONTROL 23

    3.1 Process Monitoring and Sensing 24
    3.2 Process-Feature Based Online Trajectory Generation 26
    3.3 Output Feedback Control Design 33
    3.4 Case Study: Temperature Feedback Control of a UV Curing Process 37
    3.5 Experimental Platform Development 50

4. DISTRIBUTED STATE AND PARAMETER ESTIMATION 60

    4.1 Problem Formulation 61
    4.2 Dual Extended Kalman Filter Design 68
    4.3 Demonstrative Example on Robotic UV Curing 75

Table of Contents (Continued)

Page

5. COORDINATED CONTROL AND PROCESS OPTIMIZATION 94

5.1 Open-loop Coordination 95
5.2 Rule-Based Coordinated Control 95
5.3 Distributed Model Predictive Control 99
5.4 Simulation Results 109

6. CONCLUSIONS AND FUTURE WORK 124

6.1 Conclusions 124
6.2 Future Work 127

APPENDICES 130

A. Derivation of the Equality Constraint Equation for the Open-Loop Coordination Implemented to the 1D Robotic UV Curing Process 130

REFERENCES 136

LIST OF TABLES

Page

Table 4.1 Simulation configurations 83

Table 4.2 Parameters of the UV curing process model 84

Table 4.3 Design parameters of the distributed DEKF estimation scheme 85

Table 5.1 Parameters associated with the open-loop coordination 111

Table 5.2 Optimization results for different weighting coefficients 111

Table 5.3 The control coordination rules 112

Table 5.4 Parameters associated with the rule-based coordinated control 113

Table 5.5 Simulation parameters for the distributed MPC 117

Table 5.6 The generation of the weighting matrix Q (Example) 118

Table 5.7 The selection of weighting matrices R_1 and R_2 (Example) 119

LIST OF FIGURES

Page

Figure 1.1 Convective-based (a) and radiation-based (b and c) processes 4

Figure 3.1 Online trajectory generation using process status feedback 26

Figure 3.2 Two practical approaches for online trajectory generation 27

Figure 3.3 Path transformation from operational space to the joint space 29

Figure 3.4 Trajectory of position, velocity and acceleration of the j^{th} joint 30

Figure 3.5 Status map of a 2D rectangular target at the end of the first run 31

Figure 3.6 The initial and adjusted trajectories of the position 32

Figure 3.7 The basic output feedback control structure 33

Figure 3.8 The cascade structure of the process controller 36

Figure 3.9 The robotic UV paint curing process 37

Figure 3.10 Simulation configuration for the UV irradiation process 40

Figure 3.11 (a) Temperature map of the target, open-loop curing (b) Temperature distribution along the centerline for the three methods (Scenario-1) 41

Figure 3.12 (a) Temperature map of the target, "look-and-move" strategy (b) Temperature map of the target, "run-by-run" strategy (Scenario-1) 41

Figure 3.13 Trajectory of the end effector for the three methods (Scenario-1) 42

Figure 3.14 (a) Temperature map of the target, open-loop curing (b) Temperature distribution along the centerline for the three methods (Scenario-2) 43

Figure 3.15 (a) Temperature map of the target, "look-and-move" strategy (b) Temperature map of the target, "run-by-run" strategy (Scenario-2) 43

Figure 3.16 Trajectory of the end effector for the three methods (Scenario-2) 44

Figure 3.17 Two alternative structures of the cascade PID controller 46

List of Figures (Continued)

Page

Figure 3.18 (a) Temperature map of the target, open-loop curing (b) Temperature distribution along the centerline for open-loop and feedback control (Scenario-1) 47

Figure 3.19 (a) Temperature map of the target, using power control (b) Temperature map of the target, using speed control (Scenario-1) 47

Figure 3.20 Time history of the power and the speed of the UV source (Scenario-1) 47

Figure 3.21 (a) Temperature map of the target, open-loop curing (b) Temperature distribution along the centerline for open-loop and feedback control (Scenario-2) 48

Figure 3.22 (a) Temperature map of the target, using power control (b) Temperature map of the target, using speed control (Scenario-2) 49

Figure 3.23 Time history of the power and the speed of the UV source (Scenario-2) 49

Figure 3.24 The general structure of the experimental platform 50

Figure 3.25 The control structure of the manipulator system 51

Figure 3.26 The control structure of the UV radiation system 52

Figure 3.27 The structure of the thermal vision system 53

Figure 3.28 The substrate and the film applicator 54

Figure 3.29 FTIR spectra of the painted samples (film thickness: 5 mils; distance to UV LED: 0.0254m) at different curing time (t=0s and t=30s) 55

Figure 3.30 The degree of cure conversion versus curing time for different distances between the sample and the UV LED head (d=0.0254m and d=0.0508m) ... 55

Figure 3.31 System configuration for the look-and-move strategy 57

Figure 3.32 Trajectory of the end effector and time history of temperature signal 58

Figure 4.1 The general 1D scanning problem 61

List of Figures (Continued)

Page

Figure 4.2 The structure of the DEKF estimation scheme..... 69

Figure 4.3 The operation mechanism of distributed local DEKFs 73

Figure 4.4 Cure-conversion level distributions when the actuator crosses different positions on the target strip: (a) x_a=0.35m, (b) x_a=0.9m..... 86

Figure 4.5 UV absorption coefficient distributions when the actuator crosses different positions on the target strip: (a) x_a=0.35m, (b) x_a=0.9m..... 86

Figure 4.6 Convective heat transfer coefficient distributions when the actuator crosses different positions on the target strip: (a) x_a=0.35m, (b) x_a=0.9m..... 87

Figure 4.7 (a) Time history of the cure-conversion level at x=0.9m (b) Time history of the error of the actual and estimated cure-conversion level at x=0.9m 89

Figure 4.8 (a) Time history of the UV absorption coefficient at x=0.9m (b) Time history of the error of the actual and estimated absorption coefficient at x=0.9m..... 89

Figure 4.9 (a) Time history of the convective heat transfer coefficient at x=0.9m (b) Time history of the error of the actual and estimated heat transfer coefficient at x=0.9m..... 90

Figure 5.1 The general structure of the rule-based coordinated control..... 96

Figure 5.2 Sampling windows used for local feedback signal generation..... 97

Figure 5.3 The simplified energy transmission model..... 100

Figure 5.4 The basic operation mechanism of MPC..... 104

Figure 5.5 Cure-conversion level distributions on the target strip (Scenario-1): (a) open-loop curing; (b) rule-based coordinated control 114

Figure 5.6 Time history of control signals (Scenario-1): (a) radiant power; (b) speed .. 115

Figure 5.7 Cure-conversion level distributions on the target strip (Scenario-2): (a) open-loop curing; (b) rule-based coordinated control 116

List of Figures (Continued)

Page

Figure 5.8 Time history of control signals (Scenario-2): (a) radiant power; (b) speed .. 116

Figure 5.9 Cure-conversion level distributions for three curing methods (Scenario-1): (a) Full-range view (b) Zoomed around the set-point 120

Figure 5.10 Time history of control signals for three curing methods (Scenario-1): (a) radiant power; (b) speed 120

Figure 5.11 Cure-conversion level distributions for three curing methods (Scenario-2): (a) Full-range view (b) Zoomed around the set-point 121

Figure 5.12 Time history of control signals for three curing methods (Scenario-2): (a) radiant power; (b) speed 121

CHAPTER ONE

INTRODUCTION

1.1 Research Motivation

This research is motivated by the potential benefits of a class of radiation-based processes which can help establish resource-economical and environmental-friendly production patterns for modern industry. The main objective of this dissertation is to investigate and develop formal approaches for implementing control and estimation for these process employing moving radiant actuators.

Energy and environmental issues are two major challenges faced by many industrial sectors, such as chemical and food processing, motor vehicle manufacturing, and so on. They contribute to increasing proportions of energy consumption and pollutant emissions. The 2008 Annual Energy Review provided by the Energy Information Administration (EIA) of the U. S. Department of Energy (DOE) showed that, in 2008, the total industrial energy consumption (amounting to 31% of all domestic energy consumptions) remained greater than the total energy consumptions in other end use categories [1]. On the other hand, the 2008 Annual Greenhouse Gases Emissions Report provided by U. S. Environmental Protection Agency (EPA) showed that the industrial sector was the largest source of energy-related CO_2 emissions in 2008 [2].

In many conventional industrial sectors, fossil fuels such as coal, petroleum and natural gas are used to provide energy in the term of heat for various thermal-related processes, such as the batch reactions in chemical manufacturing, frying or drying in food processing, and paint drying and curing in automotive manufacturing [3]. Typically, the

heat generated from combusting fossil fuels is delivered to the target items through conduction and/or convection. However, these conventional processes involve large amounts of greenhouse gases emissions and considerable energy losses in fuel combustion and subsequent heat transfer. These processes also require large investments in the installation and maintenance of these burning/heating facilities. In addition, these conduction/convection-based methods usually require the whole product to stay in a high-temperature environment for extended periods of time. This may lead to quality defects in the product, such as stress gradient, geometric changes, and so on.

The alternative approach for these thermal-related manufacturing processes is to use various radiation-based technologies, such as infrared (IR) / microwave drying [4-6], ultraviolet (UV) / electron beam (EB) curing [7-9], laser processing [10, 11], etc. Compared to traditional conduction/convection methods, these radiation-based processes provide the following potential advantages: 1) higher energy efficiency; 2) less pollutant emissions 3) improved productivity; 4) less space use and maintenance cost; 5) more controllability. As an example, a case study reported in [12] showed that the replacement of the convection oven by a new IR oven allowed a metal finishing plant to increase its production by 50% and reduce natural gas consumption by 25% annually. Another study from U. S. Department of Energy showed that the implementation of UV-curable coating for aluminum can production may save as much as 55% in capital and installation costs over thermal curing and reduce 47,000 tons / year of CO_2 emission if implemented industry-wide [13].

1.2 Problem Statement

Although these radiation-based methods have numerous potential advantages as described above, the implementation of these methods in mass production faces the following challenges. First, some spatially large target items (e.g. automobiles) usually require the use of many radiant actuators that operate simultaneously during the process. This will in turn increase the equipment cost and compromise the energy savings. Using large radiant sources can reduce the number of actuators but may affect the process uniformity [14]. Second, the alignment of these distributed actuators must be carefully designed to ensure that the radiant energy is delivered to the target evenly and properly. Inappropriate disposition of these radiant actuators will cause unevenness in process quality due to shadow effects, particularly on short wavelength radiation, such as UV light [14]. Moreover, the designed actuator alignment needs to change with product shapes and dimensions to ensure process quality. The redesign process will increase the maintenance cost and affect the process efficiency.

An alternative approach, which uses industrial robots to manipulate high-power mobile radiant actuators, has been attracting more attention recently [14-16]. Compared to the configuration that uses multiple fixed actuators, this approach only employs a single radiant actuator, which can be carried by the robot to move around the target and complete the desired processing task. This robotic method can help reduce the equipment cost and energy consumption by minimizing the number of radiant actuators. It can also help accommodate the orientation of the radiant actuator to complex target geometries thanks to additional control options provided by the robot manipulator. Furthermore, the

robotic approach provides adaptability for switching among various product models by only reprogramming the robot without changing the hardware configuration.

The three alternative configurations discussed above are summarized and illustrated in Figure 1.1.

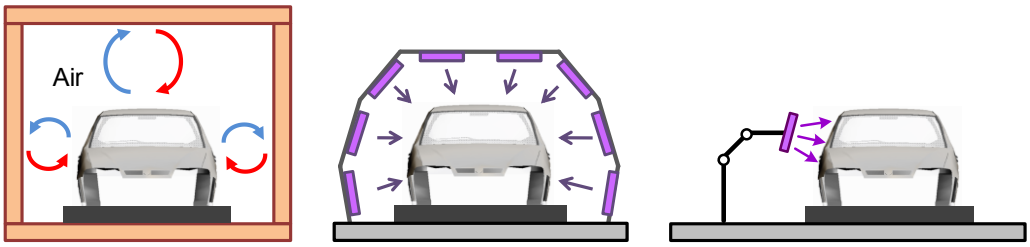

Figure 1.1 Convective-based (a) and radiation-based (b and c) processes

However, the introduction of a moving radiant actuator demands elaborate control systems to achieve the desired process quality. The main problems to be addressed in this dissertation are identified and summarized as follows.

1. Closed-loop control systems that integrate the motion and process control are needed to maintain process quality and effectively compensate for disturbances, such as geometric variations and material property changes.
2. There is a lack of robust and cost-effective direct sensing alternatives for measuring key state variables in robotic radiation-based processes. Therefore, effective distributed estimation schemes should be developed for monitoring and control of the process. This effort should also consider the changing observerbiltiy associated with this moving radiant actuator configuration and take into account the reduction of computational cost for the estimation scheme.

3. The motion of the robot and the radiant power of the actuator should be carefully coordinated to achieve further improvement and optimization of the process. A novel approach is needed to optimally resolve the coordination problem online by taking into account both process quality and energy efficiency.

All of these challenges above motivate the development of a framework that can guide the control, estimation, and optimization of these robotic radiation-based processes.

1.3 Objectives and Contributions

The objective of this dissertation is to address these robotic radiation-based processes and develop a framework for guiding the control, estimation, and optimization of these processes. This framework should provide solutions to the major challenges described above. It should guide the design of close-loop control systems to guarantee essential process quality in the presence of disturbances. It should also provide methods for estimating distributed process states and parameters under the lack of feasible direct sensing alternatives. In addition, this framework should provide a systematical approach that coordinates multiple manipulated variables optimally in order to achieve process improvement.

The major contributions of this dissertation are summarized as follows:

1. A generalized 1D scanning framework for addressing the control and estimation issues for processes employing moving radiant actuators.
2. A distributed-parameter state/parameter estimation scheme developed under the 1D scanning framework for process monitoring and control.

3. A distributed-parameter model predictive control (MPC) strategy that systematically addresses the optimal coordination of multiple manipulated variables for processes with moving radiant actuators.
4. A simplified rule-based feedback control strategy that integrates static process optimization and closed-loop coordination of multiple manipulated variables through designed control rules.
5. A novel online trajectory generation approach integrating motion control and process status feedback, specifically suitable for practical robotic radiant-based processes to compensate for disturbances.
6. An experimental platform that could be used to evaluate and validate the developed strategies and methods for estimation, control, and optimization of robotic radiation-based processes.

1.4 Dissertation Overview

The rest of this dissertation is organized as follows:

In Chapter 2, a review of related work is presented, including the state of the art control algorithms for processes employing moving actuators, state and parameter estimation methods for distributed-parameter processes, and applications of model predictive control to distributed-parameter processes.

Chapter 3 discusses online trajectory generation and output feedback control for practical robotic radiation-based processes. A survey of current technologies for process monitoring and sensing is presented. A process-feature based online trajectory generation method is also presented. This is followed by the development of an output feedback

control strategy that employs individual input manipulation. A case study of irradiation control for a robotic UV curing process is then used to illustrate the proposed trajectory generation method and output feedback control strategy. In addition, an experimental platform for demonstrating the UV irradiation case is presented and discussed.

In Chapter 4, a distributed-parameter state and parameter estimation scheme is developed. The proposed scheme uses a dual extended Kalman filter to estimate the key process states and associated parameters based on the measurement of distributed process outputs. The estimation scheme is then demonstrated on the robotic UV curing process described in Chapter 3.

Chapter 5 presents various coordinated control strategies for robotic radiation-based processes. A rule-based control strategy that combines static process optimization and closed-loop coordination of multiple manipulated variables of the moving radiant actuator is presented and discussed. This chapter also details the development of a distributed-parameter model predictive control strategy that can systematically coordinate multiple manipulated variables to optimize process quality and energy efficiency.

Finally, Chapter 6 summarizes the research work and presents concluding remarks, future research trends, and directions for applying the topics covered here to other areas.

CHAPTER TWO

REVIEW OF RELATED WORK

In this chapter, a review of existing research work related to this dissertation is presented. The relevant work is categorized into three areas. First, an overview of control strategies proposed for processes with moving actuators is presented. Then, a review of estimation methods applied for distributed-parameter processes is presented. This is followed by a review of model predictive control applications in this area.

2.1 Control Strategies for Processes Employing Moving Actuators

A comprehensive introduction on the modeling and control of manufacturing processes has been provided by Hardt in [17]. In this paper, various fundamental topics were discussed, including the classification of manufacturing processes, the modeling and identification methods, and the comparison between two basic control approaches. According to the theories provided in [17], most of these manufacturing processes with moving actuators (e.g. painting, welding, etc.) are categorized into the class of *serial processes*, in which the dominant transformation, either material or energy, occurs in a small region usually localized around a moving material or energy source. The control of these serial processes can be achieved with two different approaches. One uses direct measurement or estimation of the controlled process states, and the other employs intermediate states or process outputs, such as displacement, temperature, and so on [17]. Numerous control strategies for these serial manufacturing processes have been developed based on the fundamental concepts discussed in [17], and an overview of these strategies will be presented below from two aspects.

2.1.1 Theoretical Study

From the theoretical perspective, many industrial processes that involve the use of robot manipulators or similar devices can be simplified as a distributed-parameter system employing a moving actuator. Based on this assumption, some theories and methods have been proposed for guiding the design and control of such processes.

The earliest research was conducted by Butkovskii et al [18, 19]. They proposed the concept of *mobile control* and established some fundamental theories for modeling and control of distributed-parameter systems with a mobile source. The control problem is approximately solved by using Poisson's resummation formula and the method of stationary phase [18]. The solution enables the law of motion and the intensity of the mobile source to be determined [19]. Applications including process control in zonal heating, welding, and melting were also discussed in [19].

A similar approach has also been discussed by Khapalov in [20]. A mobile point control approach was proposed and compared to locally distributed methods. In this approach, the trajectory of the mobile point is pre-assigned and the control input becomes a function of time only. This research work also discussed the controllability and observability for the case of using two mobile points to control a class of distributed-parameter systems described by semi-linear parabolic equations.

Demetriou et al. also reported on series of work on control of distributed-parameter processes employing moving actuators [21-25]. In one of these strategies, both the position and the signal intensity of the actuator are manipulated by an LQR controller based on some pre-defined performance indexes, but the actuator has to move discretely

between some allowable locations [21]. These locations are determined according to some controllability and performance enhancing criteria [21, 22]. A moving collocated actuator/sensor method has also been developed to achieve simplified local static feedback control by using this actuator/sensor pair [23, 24]. Implementations of these control strategies to practical manufacturing processes, such as arc welding, were also discussed [25].

These theories presented above provide guidance for designing control systems for distributed-parameter processes employing moving actuators, but the physical factors of the moving actuator, such as the input distribution, power or speed limitations, etc., are seldom discussed. These factors should be integrated into the control design when dealing with actual processes.

2.1.2 Control Application

On the other hand, numerous practical control strategies have been developed and implemented to various industrial processes employing moving actuators. Compared to the theoretical study, most of these control applications focus on providing solution to a particular process by using either direct output feedback approaches or some model-based control methods. The following presents a review of these control applications in the areas of welding, painting, and so on.

Welding is a typical serial manufacturing process that involves material (rod or wire) and/or energy (heat) transformation between the moving actuator (torch) and the target. The major control inputs of the welding process include the power supply voltage, the wire feed-rate, travel speed of the torch, and the distance between the contact tip and

the target [26]. The outputs of the welding process include both geometric features of the bead (e.g. bead width, depth and height) and thermal characteristics, such as heat-affected zone, cooling rate and so on [27]. Based on these inputs and outputs, a number of strategies have been developed to achieve closed-loop control of the welding process. General multiple-input and multiple-output (MIMO) control frameworks have been discussed by Hardt [17], Huissoon [26], and Moore [28]. Their work provided basic structures for control of the welding process from equipment, geometry and thermal properties. Many of these closed-loop control strategies involve the use of geometric features as feedback signals. One of them uses a real-time full-penetration monitoring method through vision sensing and neural networks to control a robotic arc welding system [29]. Thermal-based depth estimation method has also been used to develop closed-loop strategies for weld pool depth control [27]. Another significant issue in these control applications is the modeling of the welding process. A short survey of different types of welding process model has been presented in [30]. Multivariable adaptive control strategies have also been developed to achieve improved welding quality based on identification of unknown process parameters in real time [31-33].

Similar research can be found in other manufacturing applications, such as painting, spray forming, and so on. A semi-autonomous robotic coating system, using thickness detection through multiple cameras and a laser point, has been developed by Seelinger, et al. to guide a coating robot [0]. Thermal machine vision is also used to monitor real-time painting status and control the painting robot in terms of nozzle path, speed, and so on [35]. For a spray forming process, Jones, et al. designed a time-varying

H_2 controller to regulate the temperature profile of the target by adjusting the spray rate based on thermal image feedback through an infrared camera [36]. In a robotic cutting process, a combined control strategy (adaptive position control, a switching logical velocity control, and a learning algorithm for force control) that uses position/velocity feedback and force compensation has been developed by Zeng, et al. to ensure the cutting quality [37]. To improve the dimensional accuracy and surface finish of targets in a laser cladding manufacturing process, Liu and Li developed an in-time motion adjustment strategy that manipulates the speed and orientation of the robot based on measured status of the existing clad layer, stand-off distance, and melt pool through multiple sensors [38]. Moreover, feedback control of the moving actuator has also been applied to a metal forming process, in which a stereovision camera is used to provide geometric feedback for controlling the mobile tool based on a reduced process model [39].

Although these control applications described above involve various manufacturing processes employing one or more moving actuators, the common objective of most of these applications can be summarized as: To achieve improved process quality by adjusting one or more manipulated variables of the moving actuator based on measured or estimated process states. Since the direct sensing of essential process states is not always available, estimation from measurable process outputs becomes important to for monitoring the on-going process status. The next section will provide a review of some estimation methods applied to distributed-parameter processes.

2.2 Estimation Methods for Distributed-Parameter Processes

As already pointed out, the use of state observer or estimator is essential for many manufacturing process due to the lack of robust and cost-effective direct sensing alternatives for some key process states. The major challenges in developing appropriate estimation methods for these distributed-parameter processes arise in the three fundamental issues [40]. First, the process model has to be reduced or simplified so that it can be used for designing the estimator. Then, the type and structure of the estimator should be carefully selected and designed. Moreover, uncertainties of the models used for estimation should be compensated for robustly and adaptively. The following sections will present a review of estimation methods for distributed-parameter processes in consideration of the three issues.

2.2.1 Model Reduction and Simplification

Many model reduction and simplification methods have been used for estimation of distributed-parameter processes. A survey of general model reduction methods can be found in [41, 42]. The applications of these methods to distributed parameter process have been discussed in [43-47]. Rafaralahy, et al. used Generalized Orthogonal Polynomials (GOP) to reduce the distributed-parameter system governed by partial differential equations (PDEs) to a finite dimensional non-linear system and designed a state observer based on the reduced process model [43]. This method was then implemented to a 1D heat transfer problem, but no external control input was applied. A similar study has been conducted by Lilly in [44]. A linear distributed parameter system was reduced by using a set of orthogonal basis functions and then an adaptive observer

was designed for state and parameter estimation. Alaeddine and Doumanidis developed a finite dimensional model for a class of thermal-based processes by using Galerkin optimization method which minimizes the error between the approximated and actual models [45]. Another Galerkin-based method (Galerkin weighted residual projection) has been used by Shvartsman et al. in [46] to simplify a 2D reaction model and use it for estimation and control design. The approximate inertial manifold (AIM) method has also been used for model reduction by Christofides and Daoutidis in [47]. This method approximates the original system by using its dominant dynamics called inertial manifold, and the corresponding PDEs are reduced to a set of ordinary differential equations (ODEs).

2.2.2 Types and Structures of the Estimator

The overview of different types of estimators used for distributed-parameter process control can be found in [40, 48]. Soroush provided a comprehensive introduction of various observers applied to linear, nonlinear, and multi-rate estimations in [48]. Dochain discussed three types of estimators (Kalman, Luenberger, and Asymptotic observers) and gave detailed applications of these estimators to a chemical reaction process in [40]. In this dissertation, we choose to use the Kalman filter for state and parameter estimation, and thus the following paragraphs present a review of various applications of the Kalman filter for estimation and control of distributed-parameter processes.

One of the most popular Kalman type filters used for state and parameter estimation is the extended Kalman filter (EKF), which has been widely used for

estimation and control of various nonlinear distributed-parameter processes. In one of these applications, Soucy and Holt used the EKF algorithm to estimate the extent of reaction in a polymer composite processing system from temperature measurements and proposed a closed-loop control approach [49]. The EKF design is based on an approximation of the kinetic and heat transfer models. Similar research involving the control of a reactive distilling system based on estimated process state through the EKF algorithm can be found in [50]. The influence of model uncertainties on the estimation performance was also discussed in this study, but no uncertainty compensation was applied to the estimator. Xiong, et al. discussed the implementation of the EKF to a chemical vapor deposition process for estimating film thickness, roughness, and growth rate from film surface reflectance measurements captured by an in situ sensor [51]. The EKF algorithm has also been used in a freeze-drying process to estimate the temperature profile along the frozen product based on a simplified process model and single point temperature measurement [52].

Other structures of the Kalman filter, adapted from the original form, have also been used for process estimation and control. Lendek, et al. developed a distributed Kalman filtering strategy to estimate the state of a linear distributed-parameter process [53]. In this strategy, a decomposition of the process model into a set of subsystems allows the use of individual Kalman filter on each of these subsystems. This distributed strategy reduces the complexity and computational costs at the price of suboptimal performance. Li and his co-workers designed a hierarchical EKF structure to estimate unmeasured states and key kinetic parameters in an ethylene–propylene–diene polymer

(EPDM) polymerization process [54]. In this hierarchical structure, two EKFs, using different measuring rates, were designed and applied to two subsystems involving the dominant dynamics of the process. Rezaei, et al. used a hybrid EKF strategy, including a conventional lumped Kalman filter and an off-line process model, to estimate the end-state distribution along a tubular plug-flow reactor [0]. This hybrid method reduces the computational cost, but it is limited to the estimation of the end-states.

2.2.3 Model Uncertainty Compensation

Model uncertainty, caused by inaccurate modeling or unknown model parameters, is one of the biggest challenges faced by most of the estimation methods discussed above. One approach to compensate for these uncertainties is to design a class of estimators that do not require accurate modeling, such as asymptotic observers [56]. The main drawback of this approach is that the convergence rate of the estimation is fully determined by operating conditions [40, 57]. The alternative way is to use a basic model with known structure but unknown or inaccurate parameters and estimate these parameters online. The estimated parameters are then incorporated into the state observer to improve estimation performance [40, 57]. This online parameter estimation approach is chosen in this dissertation to compensate for model uncertainties involved in the design of the Kalman type state estimator. An overview of various online parameter estimation methods is given below.

Some of these methods use the EKF algorithm to estimate state and parameter simultaneously. There are two basic approaches to achieve simultaneous state and parameter estimation: Joint EKF and Dual EKF [58]. The Joint EKF incorporates the

unknown parameters into the state vector and uses a single extended Kalman filter to estimate the new combined state and parameter vector. In contrast, the Dual EKF uses two cooperating extended Kalman filters to estimate the state and parameter in parallel. Applications of these two EKF strategies are found in the estimation and control of some biochemical or mechanical processes [57, 59]. Hulhoven, et al. discussed the application of the joint state and estimation strategy to a macroscopic bioprocess in [57]. They used the combination of a Joint EKF and an asymptotic observer for improved estimation performance and uncertainty compensation. Similarly, Moireau, et al. developed a joint state-parameter estimation procedure based on a collocated feedback strategy and a Kalman filter for parameter estimation [59]. This procedure was then implemented to a linear and a bilinear mechanical system, respectively. They also discussed the potential of extending this framework to other state observers. The Dual EKF approach has been applied to the estimation of traffic flow, vehicle status, noisy speech signals, etc [60-62]. However, applications of the Dual EKF are seldom found in literature that discussed distributed-parameter processes.

Other estimation methods, such as particle filters, are also used for online parameter estimation. Chen, et al. developed a framework for online state and parameter estimation for a batch process by using a particle filter algorithm along with an auxiliary sampling importance re-sampling (ASIR) filter and a kernel smoothing method [63]. However, the computational cost will be increased significantly when this approach is implemented to distributed-parameter processes due to the increasing model dimension. Sawo, et al. proposed an online estimation strategy for both the states and parameters of a

2D distributed-parameter system described by linear PDEs [64]. The simultaneous state and parameter estimation is decomposed into a linear and a non-linear problem by using the sliced Gaussian mixture filtering. Damak developed and applied an asymptotic state and parameter estimation method to a distributed biochemical process [65]. The estimation strategy was designed based on local asymptotic stability properties, and a reduced process model obtained by using the orthogonal collocation method.

In summary, the above three subsections reviewed the existing estimation methods from aspects of model reduction, estimator type and structure, and uncertainty compensation. These methods provide fundamental frameworks for guiding the design of appropriate state and parameter estimators for robotic radiation-based processes that are studied in this dissertation.

2.3 Model Predictive Control for Distributed-Parameter Processes

For most robotic radiation-based processes, the process quality is usually influenced by multiple manipulated variables of the actuator, such the radiant power, the moving speed, and so on. Therefore, it inherently requires the optimization of these manipulated variables to achieve the desired performance indexes, for example, the acceptable quality, minimum energy use, etc. One widely-used method that can help achieve this objective is the model predictive control (MPC) approach. This method uses the model-based process prediction and the moving finite-horizon optimization algorithm to achieve the control objective. In this section, a review of MPC-related methods and their applications to distributed-parameter processes is presented.

Model predictive control strategies have been used for various industrial processes that are described by distributed-parameter models. Dufour, et al. developed a MPC framework for the control of a class of distributed-parameter processes modeled by PDEs [66, 67]. The proposed framework is composed of an off-line trajectory optimization based on a nonlinear PDE model and an online MPC strategy based on linearized model and process measurements. Shang, et al. presented another MPC approach for the control of distributed-parameter systems based on the method of characteristics [68, 69]. In this strategy, the PDEs describing the process model are transformed into ODEs along the characteristic curves, and a high-accuracy process prediction is used to formulate the MPC algorithm. However, constraints are not considered in this characteristics-based MPC approach. Aggelogiannaki and Sarimveis developed a nonlinear MPC strategy based on radial basis function neural network and applied it to a tubular reactor in [70]. This method uses the neural network trained by input-output data to describe the temporal and spatial behaviors of the system instead of using PDEs, so it helps reduce the computational cost when implementing the MPC strategy in real time. A hybrid singular value decomposition and radial basis function model used for MPC design was also discussed in this study. Bernard and Moghaddam proposed a nonlinear MPC approach to control a complex glass forming process, based on a PDE type process model solved by Finite Element Method (FEM) [71]. The MPC strategy is developed in consideration of the trade-off between the control performance and computational cost. The potential of this method for real industrial applications was also outlined.

Model predictive control applications are also found in processes involving moving actuators. Dubljevic developed a model predictive control framework for a class of diffusion-reaction processes with multiple collocated actuators and sensors [72]. The MPC strategy generates an optimal control action to switch these actuators which are located at a set of pre-specified positions. Model decomposition was also considered in the MPC formulation. Although this multiple fixed actuators architecture can be equivalent to the one employing a single moving actuator, the constraint on the speed of the moving device should be integrated into the MPC controller since it has to travel from one position to another physically. Qian and Zhang developed a two-input single-output MPC strategy to control a quasi keyhole plasma pipe welding process based on a linear model [73]. An online recursive least squares algorithm was used to identify uncertain model parameters. The designed MPC strategy has also been implemented in real time. The control of the speed of the welding torch wasn't discussed in this study. Moreover, a neural-network based nonlinear MPC strategy applied to a cutting process was discussed in [74]. In this work, a neural-network process model and a robust generic-algorithm-based optimizer were developed. The proposed MPC strategy was then applied to control the tool support shifting in the cutting process to achieve desired process quality and prevent tool oscillation. The manipulation or control of the cutting speed control wasn't discussed in this work.

These reviewed MPC methods which are used to control various distributed-parameter processes employing either fixed or moving actuators provide essential guidance for developing a distributed-parameter MPC framework for the control of

robotic radiation-based processes in this work. The proposed MPC framework that focuses on addressing the optimal coordination of multiple manipulated variables will be detailed in Chapter 5.

Chapter Summary

This chapter provided a review of related work on: 1) control algorithms and applications for processes employing moving actuators; 2) estimation methods for distributed-parameter processes; 3) model predictive control strategies and applications for distributed-parameter processes. The first section of this chapter summarized existing theories and applications for the control of moving-actuator-based processes. Most of these control methods involve online sensing or estimation of process states, and coordination of multiple manipulated variables. Different estimation methods for distributed-parameter processes were reviewed in the second section from the aspects of model reduction, estimator type and structure, and uncertainty compensation. The Kalman type estimators for both state and parameter estimation are found popular in various applications. The final part of this chapter reviewed the use of various model predictive control methods in distributed-parameter processes employing fixed or moving actuators. These theories and methods reviewed in this chapter provided significant guidance for the continuing investigations in some of these areas, which will be detailed in the rest of this dissertation.

The following chapters will present the continuing work in developing a general framework, including closed-loop control design, online state and parameter estimation, and coordinated control and optimization for robotic radiation-based processes. This

framework integrates some of the theories and methods discussed above with essential adaptations to the moving-actuator problem addressed in this dissertation. Case studies on a robotic UV curing process will also be presented to illustrate the developed framework.

CHAPTER THREE

ONLINE TRAJECTORY GENERATION AND FEEDBACK CONTROL

As pointed out in Chapter 1, the performance of these robotic radiation-based processes is significantly influenced by the relative configuration between the moving radiant actuator and the target item. In traditional trial-and-error methods, this issue is usually handled by taking a lot of off-line training or calibration on the practical robotic system, which may not be robust enough for disturbance rejection. The alternative way is to implement some of the feedback control approaches summarized in the first section of Chapter 2, which can help improve the process performance and compensate for disturbances by adaptively adjusting either the motion of the robot or the power of the radiant actuator.

This chapter will discuss the application of feedback control methods to practical robotic radiation-based processes from the following aspects: 1) online motion/trajectory planning for the robot; 2) basic output feedback process control. The two approaches developed in this chapter combine the fundamental feedback control theories and some novel practical strategies proposed for this particular problem. A survey of state of the art sensing technologies that can be used for real-time process monitoring is presented at first. This is followed by the development of an online trajectory generation method for manipulating the motion of the robot in real time. In addition, a basic output feedback control strategy is proposed to achieve disturbance rejection by adjusting either the motion of the robot or the power of the radiant actuator. Both the online trajectory generation method and the output feedback control strategy are implemented to a robotic

UV curing process through simulation, and an experimental platform is also developed for demonstration.

3.1 Process Monitoring and Sensing

To achieve the closed-loop control objective, online monitoring and sensing of the process is needed to provide essential feedback information. A review of existing methods that are widely used for online process monitoring and sensing is presented below.

3.1.1 Mechanical Methods

There are a lot of methods that depend on detecting mechanical properties of the product, such stress, stiffness, etc., to monitor on-going status of industrial processes. For example, for a film drying process, Chen, et al. used stress measurement method to monitor the moisture loss during the drying process [75]. Another example is the use of ultrasonic technologies to monitor online cure status for epoxy-based polymerization processes [76, 77].

3.1.2 Optical Methods

For some industrial processes, the on-going process status can be monitored by using various passive or active optical methods, such as optical imaging through cameras [78, 79], refractive index measurement [80], etc. These methods are widely used in online process monitoring and sensing because of their nondestructive mechanism and high accuracy. However, the performance of these optical methods may be significantly influenced by the environmental factors, such as fog, dust, and etc.

3.1.3 Electrical Methods

Another approach for online process monitoring and sensing is to use various electrical or electromagnetic methods, such as dielectrometry, electromagnetic pulse detection, etc. The dielectric methods have been used for process monitoring during the curing of adhesively bonded joints [81] and glass fiber-epoxy composites [82]. However, the dielectric sensors used in these methods have to be embedded into the monitored target. For a film painting process, a noncontact method has been developed to monitor the film thickness by measuring the echo signal of a terahertz (THz) electromagnetic pulse [83]. Other electrical methods, such as triboelectric sensing, have also been used for process monitoring in industrial granulation and drying processes [84].

3.1.4 Spectrometry Methods

Various spectrometry methods, such as real-time infrared spectroscopy (RTIR), near-infrared spectroscopy (NIR), etc., are also used for online process monitoring [85-87]. However, most of these methods are not suitable for industrial applications due to the high equipment cost and the lack of appropriate physical form factors of the devices.

3.1.5 Thermal Methods

Many industrial processes, such as drying, curing, and welding, involve associated thermal evolution represented by temperature changes during the process. Such thermal characteristics can be used for process monitoring. These thermal-based methods can be divided into two major categories. One is the calorimetry-based methods that are used for monitoring cure status of polymerization processes [88, 89]. The other is a class of thermograph-based methods that use various infrared (IR) sensing technologies.

These methods have been widely used in various industrial applications due to their fast response, nondestructive nature, reasonable cost and feasible physical form factors [90, 91].

3.2 Process-Feature Based Online Trajectory Generation

For most robot-based manufacturing processes, the motion of the robot manipulator is pre-determined before it is implemented to these processes. In this approach, both the path (*spatial* domain) and trajectory (*temporal* domain) of the robot manipulator are usually designed through trial-and-error or calibration. The drawbacks of this off-line approach include: 1) low process efficiency caused by time-consuming calibrations; 2) poor disturbance-rejection capability due to the open-loop control nature. These drawbacks could be further aggravated for robotic radiation-based processes, since these processes may run faster and have higher quality requirements than others.

In this section, an online trajectory generation method will be developed to deal with these issues by incorporating process status feedback through some of the sensing or monitoring methods discussed in the previous section. The general structure of the proposed online trajectory generation strategy is illustrated in Figure 3.1.

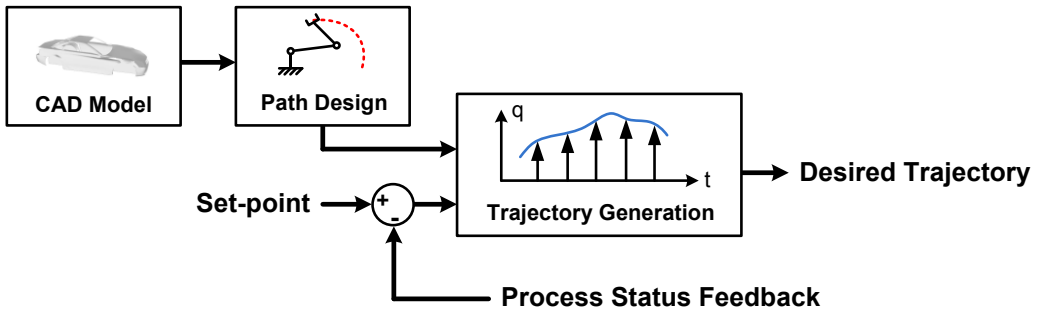

Figure 3.1 Online trajectory generation using process status feedback

The path design shown in Figure 3.1 can be done off-line considering the geometric model (given in various computer-aided design (CAD) formats) of the target product. In this process, the desired *spatial* profile of the end effector of the robot is generated in the operational space. The next step is to generate the trajectory in the *temporal* domain. In the proposed approach illustrated in Figure 3.1, the trajectory generation not only uses the designed spatial path as starting input, but it also takes into account the real-time process status. To implement this online trajectory generation strategy, two practical approaches can be considered as illustrated in Figure 3.2.

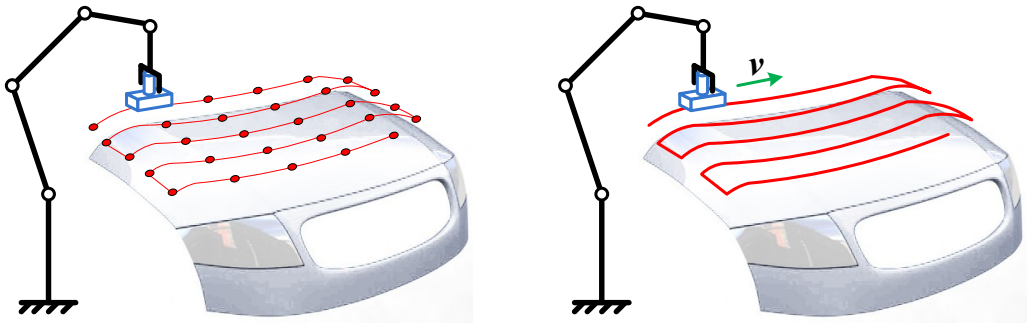

Figure 3.2 Two practical approaches for online trajectory generation

In the first approach shown in Figure 3.2(a), the sensor used for measuring process status is co-located with the moving actuator (denoted by the blue box). A look-and-move strategy can be used to determine the trajectory based on this actuator/sensor configuration. The complete path profile is divided into a set of segments, and the actuator moves through these segments in a discrete manner. In the meantime, the sensor keeps monitoring ("look") the process status of the current segment where the actuator stays, and determines when it should move to the next segment.

The second approach depicted in Figure 3.2(b) uses a run-by-run strategy to achieve the online trajectory generation. In this case, the process status is monitored in a global manner by using either multiple distributed sensors embedded in the product or a single overhead sensor which has a full view of the product. Compared to the first approach in which the task is divided spatially, this strategy breaks down the task into a series of sequential actions. The actuator has to move through the product multiple times to complete the desired task. The trajectory of the actuator at each run is determined based on the measured process status at the end of the previous run.

The following subsections provide more details on the two trajectory generation strategies [92, 93].

3.2.1 Look-and-Move Strategy

In the look-and-move strategy, the total path is divided into a set of segments that can be characterized by the position and orientation of their central normal vectors in the operational space. These kinetic characteristics are represented by a series of transformation matrices defined below [94].

$$T_i = \begin{bmatrix} n_{xi} & o_{xi} & a_{xi} & p_{xi} \\ n_{yi} & o_{yi} & a_{yi} & p_{yi} \\ n_{zi} & o_{zi} & a_{zi} & p_{zi} \\ 0 & 0 & 0 & 1 \end{bmatrix}, \quad i = 1, 2, \cdots \tag{3.1}$$

$$\begin{aligned} &\mathbf{n}_i = \{n_{xi}, n_{yi}, n_{zi}\}^{\mathbf{T}},\ \mathbf{o}_i = \{o_{xi}, o_{yi}, o_{zi}\}^{\mathbf{T}},\ \mathbf{a}_i = \{a_{xi}, a_{yi}, a_{zi}\}^{\mathbf{T}}, \\ &\mathbf{p}_i = \{p_{xi}, p_{yi}, p_{zi}\}^{\mathbf{T}} \end{aligned} \tag{3.2}$$

Here, the number of segments is denoted by N_s. The vector $\mathbf{p}_i$ represents the position of the central normal vector of the i^{th} segment in the operational space. The

associated orientation is described by three vectors named $\mathbf{n}_i$, $\mathbf{o}_i$, and $\mathbf{a}_i$. These transformation matrices can also be described in the joint space by using the following nonlinear functions.

$$T_i = J(q_{1i}, q_{2i}, \cdots \qquad \cdots \tag{3.3}$$

In equation (3.3), the joint variables $q_{1i}, q_{2i}, \cdots$ are defined with respect to their own local coordinate frames. The subscript n denotes the degree-of-freedom (DOF) of the robot. To make the robot end effector target each segment in the designed position and orientation, the following inverse kinematics problem should be solved to find the joint variables corresponding to a given position and orientation [95].

$$\begin{aligned} \mathbf{q}_i &= J^{-1}(T_i), \quad i = 1, 2, \cdots \\ \mathbf{q}_i &= \{q_{1i}, q_{2i}, \cdots \end{aligned} \tag{3.4}$$

Here, the vector $\mathbf{q}_i$ is composed of all joint variables and it determines the posture of the robot corresponding to the current segment it will move through. The above transformation from the operational space to the joint space is illustrated in Figure 3.3.

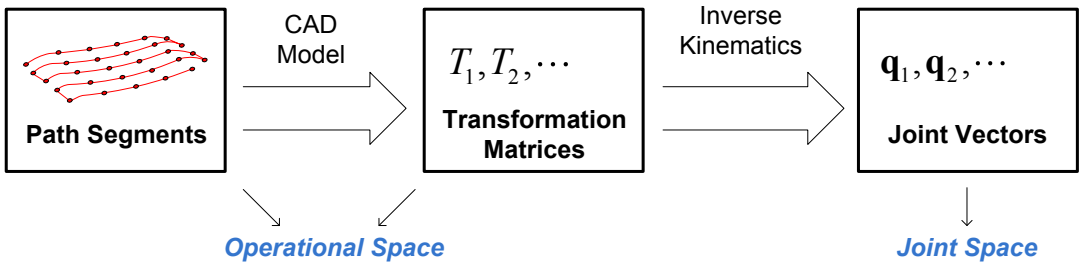

Figure 3.3 Path transformation from operational space to the joint space

Once the joint vectors for all segments of the path have been calculated, the trajectory of each joint can be generated in a discrete manner as illustrated in Figure 3.4.

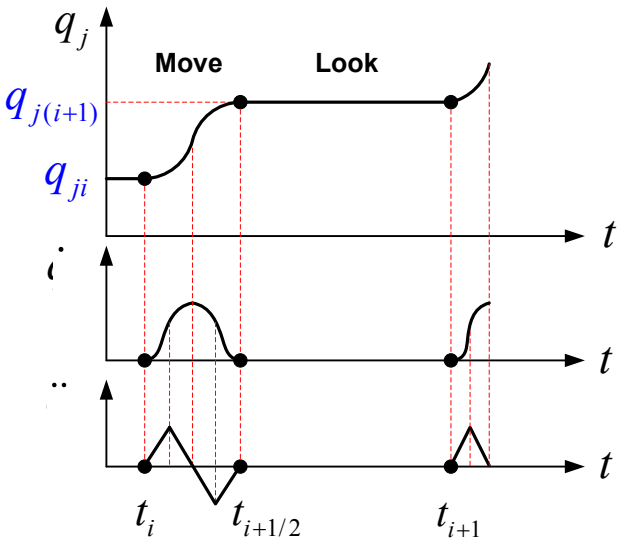

Figure 3.4 Trajectory of position, velocity and acceleration of the j^{th} joint

In Figure 3.4, the position, velocity and acceleration of the j^{th} component of the joint vector is denoted by q_j, $\dot{}$, and $\ddot{}$, respectively. The joint positions corresponding to two adjacent path segments are represented by q_{ji} and $q_{j(i+1)}$ ($i = 1, 2, \cdots$). The position trajectory shown in Figure 3.4 illustrates a single look-and-move cycle. First, the position of the j^{th} joint changes from q_{ji} to $q_{j(i+1)}$ when the end effector moves from the previous segment to the current one. Then the j^{th} joint and others rest at their current positions to allow the actuator and sensor to process and monitor the product. Once the operation on the current segment has been completed, another look-and-move cycle is activated to repeat this process on the next segment. As shown in Figure 3.4, the trajectory of a single cycle is composed of two parts. The first part ("move") is designed

as a spline type to smooth the movement of the end effector between two adjacent segments. The duration of this part is defined as Δt_m ($\Delta t_m = t_{i+1/2} - t_i$). This duration is designed off-line based on the dynamic characteristics of the robot manipulator. In the second part ("look"), the joint will hold its current position for a while until the next cycle is activated. The duration of this part ($\Delta t_p = t_{i+1} - t_{i+1/2}$) is determined *online* based on the comparison of the measured process status and the set point (feedback error).

3.2.2 Run-by-Run Strategy

In the run-by-run strategy, the end effector with the radiant actuator will move through the whole product continuously at each run. In the mean time, a single global sensor or multiple distributed local sensors are used to measure the process status at the end of each run. For the first run, the robot moves the actuator by following a pre-designed trajectory, and the sensor captures status map of the whole product at the end of this run. The status map is then compared with the reference and some adjustments are applied to the trajectory of the robot to improve the performance for the next run. A simple 2D processing example is given below to illustrate this strategy. The initial trajectory uses a constant moving speed (shown in Figure 3.6(a)) and the measured status map after the first run is depicted in Figure 3.5.

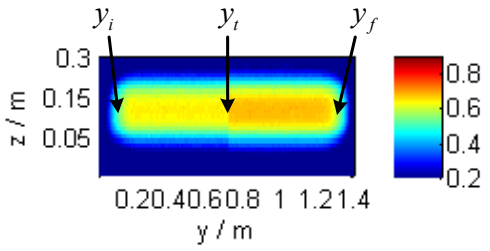

Figure 3.5 Status map of a 2D rectangular target at the end of the first run

As shown in Figure 3.5, the process uniformity after the first run is poor due to some uneven properties of the surface (e.g. uneven finishing, etc.). Since the right half of the plane has a higher degree of process completion than the left one, the initial trajectory should be adjusted to help compensate for this unevenness during the next run. The updated trajectory is illustrated in Figure 3.6(b).

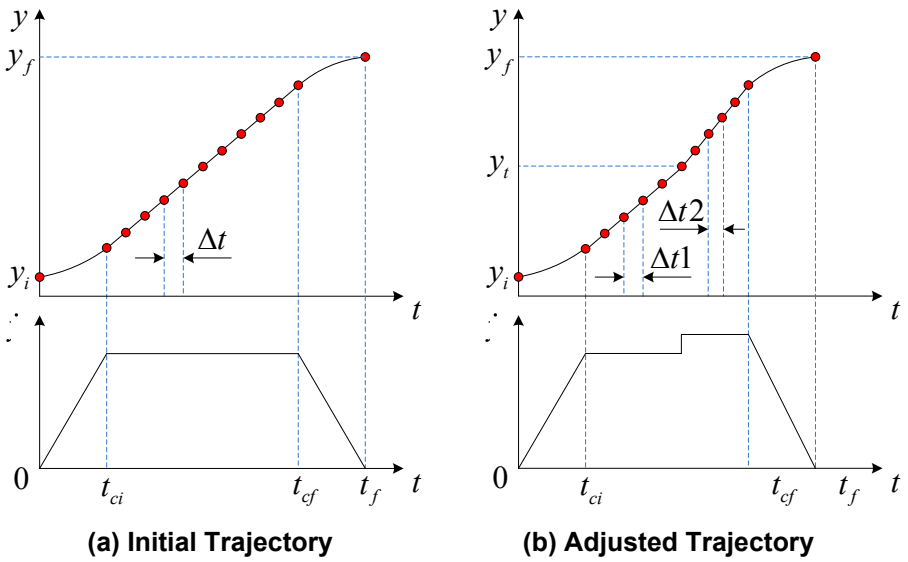

(a) Initial Trajectory **(b) Adjusted Trajectory**

Figure 3.6 The initial and adjusted trajectories of the position and the velocity of the robot end effector

In the initial trajectory shown in Figure 3.6, the end effector with the actuator starts from the initial position y_i with zero velocity and then accelerates to a constant speed. When it is close to the final position y_f, the end effector will decelerate and reach the end with zero velocity. In practice, this continuous trajectory is approximated by a series of points with a pre-determined time interval Δt. The duration of acceleration (t_{ci}) and deceleration ($t_f - t_{cf}$) is also designed off-line based on the dynamic characteristics of the manipulator. In the adjusted trajectory, two time intervals ($\Delta t1$ and $\Delta t2$) are used

to switch the speed of the end effector when it moves across the boundary position denoted by y_t. In this case, a higher speed ($\Delta t2 < \Delta t1$) is implemented to the end effector when it enters the right half part of the target plane so that the unevenness of the process can be compensated for. The above online trajectory adjustment can be repeated during the remaining runs until the desired process quality is achieved.

3.3 Output Feedback Control Design

The online trajectory generation method discussed in the previous section provides one approach to improve process quality by adjusting the motion of the actuator gradually. This section details a more comprehensive closed-loop control approach that employs the measured process output for feedback. The proposed control strategy combines both the moving/local sensing and the global monitoring configurations. It aims to improve the process quality in the presence of disturbances by manipulating one of the manipulated variables of moving radiant actuator [0]. The general structure of the proposed control strategy is illustrated in Figure 3.7.

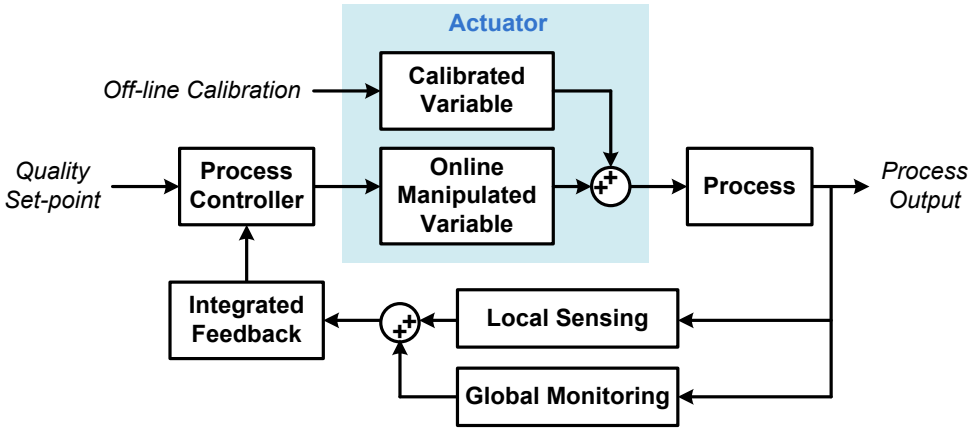

Figure 3.7 The basic output feedback control structure

In the control structure shown in Figure 3.7, the process output (e.g. temperature, etc.) is measured by using both the local and global sensors. The feedback signal is then generated and sent to the process controller. The actuator has two types of manipulated variables. The calibrated variable is determined off-line, while the online manipulated variable is regulated by the process controller based on the comparison of quality set-point and process output feedback. The following paragraphs detail the generation of the feedback signal and the selection of different manipulated variables for control of the process.

3.3.1 Generation of the Feedback Signal

Considering a radiation-based process on a simple 2D rectangular target, the local and global measurement of the process output can be represented in a general form:

$$V(x,y,t) = \xi(x,y)Y(x,y,t), \quad x \in [x_{lb}, x_{ub}],\ y \in [y_{lb}, y_{ub}] \tag{3.5}$$

Here, the boundaries of the rectangular area are defined by $x = x_{lb}$, $x = x_{ub}$, $y = y_{lb}$, and $y = y_{ub}$. The distributions of the actual and measured process output are represented by $Y(x,y,t)$ and $V(x,y,t)$, respectively. The relationship between them is described by a spatial distribution function $\xi(x,y)$. The following definitions of $\xi(x,y)$ are used for the local and global measurement configurations, respectively.

$$\text{Local Measurement:} \quad \xi(x,y) = \begin{cases} 1, & \text{if } x \in [x_a - w_x, x_a + w_x],\ y \in [y_a - w_y, y_a + w_y] \\ 0, & \text{otherwise} \end{cases} \tag{3.6}$$

$$\text{Global Measurement:} \quad \xi(x,y) = 1, \quad \forall x \in [x_{lb}, x_{ub}],\ \forall y \in [y_{lb}, y_{ub}] \tag{3.7}$$

In equation (3.6), a rectangular window function is defined to describe the local measurement configuration in which the sensor is co-located with the moving actuator. The position of the actuator is denoted by (x_a , y_a), which is also the center of the measuring window. The length and width of the window are represented by w_x and w_y , respectively. For the global measurement configuration, the observation window is expanded to the whole processing zone, so the measured distribution of the process output covers the whole zone.

The measured distribution of the process output through the local and global configurations is usually averaged in the following manner to generate appropriate feedback signals.

$$\vartheta(t) = \frac{1}{A_\Omega} \iint_{x,y \in \Omega} w(x,y) V(x,y,t) dxdy \tag{3.8}$$

Now the feedback signal becomes only the function of time by averaging the spatially distributed process output within the measuring window Ω . The area of the measuring window is denoted by A_Ω . The term $w(x,y)$ is a spatially distributed weight coefficient. The selections of $w(x,y)$ for both the local and global measurement configurations are determined by the designed control strategy. This issue is discussed in the next subsection.

3.3.2 Feedback Control by Using Different Manipulated Variables

The feedback signals generated from the local and global sensors are then used to achieve closed-loop control of these robotic radiation-based processes. Here, two

manipulated variables are considered for the feedback control: the radiant power of the actuator and the speed of the robot end effector. Given the control structure shown in Figure 3.7, either of the two can be selected as the online manipulated variable while the other is calibrated off-line and kept constant during the process.

A cascade control structure is designed to exploit both the local and global feedback information. This cascade control structure is illustrated in Figure 3.8.

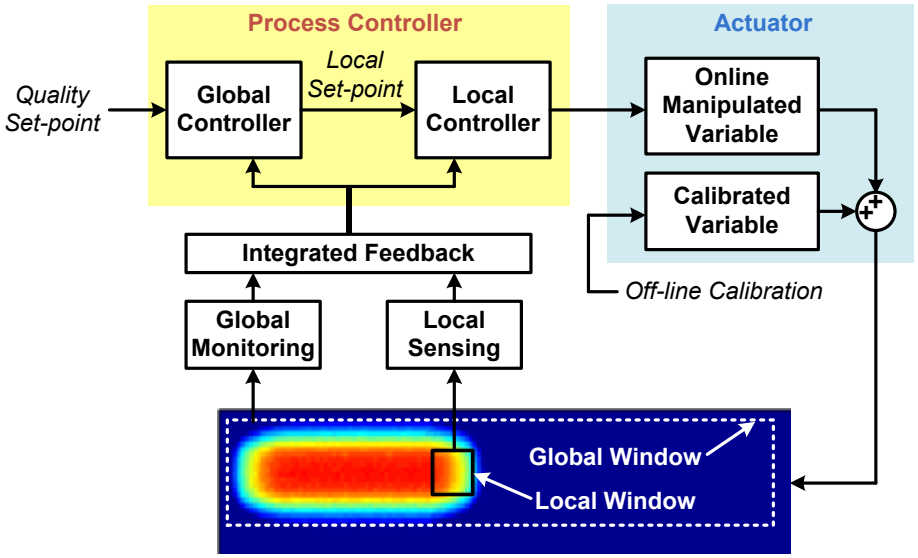

Figure 3.8 The cascade structure of the process controller

The rectangular color map in Figure 3.8 represents the distribution of the measured output of a 2D process. The processed and unprocessed areas are denoted by the red and blue color, respectively. The currently processed area is enclosed by a small black frame, which also defines the measuring window for the local sensor. Since the currently processed area includes both the processed and unprocessed parts, the average process output within the local measuring window is typically lower than the quality set-point. Therefore, a secondary set-point, named local set-point, may be generated for

regulating the local process output. This local set-point is generated by the global controller. Although the global sensor can monitor the complete area enclosed by the white dash-line frame, the weight coefficient $w(x, y)$ mentioned in the previous subsection will be introduced to ensure that the average process output within the global measuring window is calculated dominantly from the processed area rather than unprocessed area.

The cascade controller can manipulate either the radiant power of the actuator or the speed of the robot end effector. The main advantage of this control structure is that it takes into account both the local and global process information. The control performance is demonstrated in the case study below.

3.4 Case Study: Temperature Feedback Control of a UV Curing Process

The case study presented in this section illustrates the implementation of the online trajectory generation method and the output feedback control strategy to a robotic ultraviolet (UV) paint curing process, as illustrated in Figure 3.9.

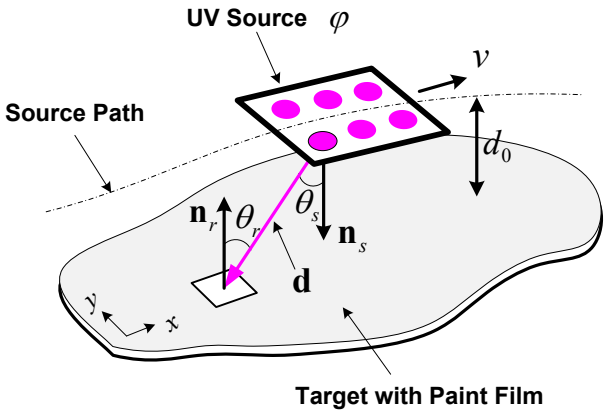

Figure 3.9 The robotic UV paint curing process

As one of the most significant radiation-based processes, the UV curing method depicted in Figure 3.9 has the potential to replace conventional oven-based curing methods due to its low energy cost and short processing time. In this process, the cure quality is mainly influenced by the distribution of the UV irradiance on the processed product. Therefore, the irradiance distribution has to be precisely controlled to ensure that the UV energy is delivered to the target surface properly and uniformly. The online trajectory generation method and the output feedback control strategy developed in the previous section will be used to deal with this issue.

3.4.1 Modeling of the UV Irradiation Process

The case study here only considers the irradiation part of the UV curing process. The basic UV irradiation mechanism can be described by using the monochromatic Lambertian point source model [97] and fundamental radiative heat transfer theory [98]. The irradiance distribution on the 2D surface shown in Figure 3.9 is represented by:

$$I(x,y,t)=\sum_{i=1}^{N}k(x,y)\frac{\varphi(t)\cos\theta_s^i(x,y,t)\cos\theta_r^i(x,y,t)}{N\pi\left|\mathbf{d}_i(x,y,t)\right|^2} \tag{3.9}$$

The UV source used here (an LED panel) is composed of multiple cells (LEDs) and each of them is modeled as a Lambertian point source. The number of the cells and the total radiant flux (W) of the UV source is denoted by N and $\varphi(t)$, respectively. The coefficient $k(x,y)$ is used to describe the UV absorption variety throughout the target surface. The irradiation from a single UV cell is significantly influenced by the relative configuration between the cell and the target surface. This configuration is characterized by three fundamental parameters: the position vector $\mathbf{d}(x,y,t)$, the emission angle

$\theta_s(x,y,t)$, and the incidence angle $\theta_r(x,y,t)$. The superposition principle is applied to obtain the total irradiation distribution $I(x,y,t)$. The energy density distribution on the target surface ($E(x,y,t)$) is then represented by:

$$E(x,y,t) = \int_0^t I(x,y,\tau)d\tau \tag{3.10}$$

The accumulated energy will cause a temperature increase on the target surface. In this case study, conductive and convective heat transfer components are simply ignored, considering the dominant energy delivery through UV radiation. Then the thermal dynamics can be roughly described by:

$$\rho c l \frac{dT(x,y,t)}{dt} = I(x,y,t) \tag{3.11}$$

Here, ρ, c, and l denote the density, the specific heat capacity, and the thickness of the paint film, respectively. Equation (3.11) can be further transformed into:

$$T(x,y,t) = T(x,y,t_0) + \frac{1}{\rho c l}\int_0^t I(x,y,\tau)d\tau = T(x,y,t_0) + \frac{1}{\rho c l}E(x,y,t) \tag{3.12}$$

The correlation between the temperature $T(x,y,t)$ and the accumulated energy $E(x,y,t)$ on the target surface makes it possible to use temperature feedback to control the UV irradiation process.

3.4.2 Application of the Online Trajectory Generation

To demonstrate the online trajectory generation method, a simulation study is conducted in this subsection, using the irradiation model implemented in MATLAB/Simulink and a dynamic model of the robot manipulator established in

SIMPACK (a multi-body dynamics simulation package). The process target used in this simulation is a 2D rectangular plane. The simulation configuration is illustrated in Figure 3.10.

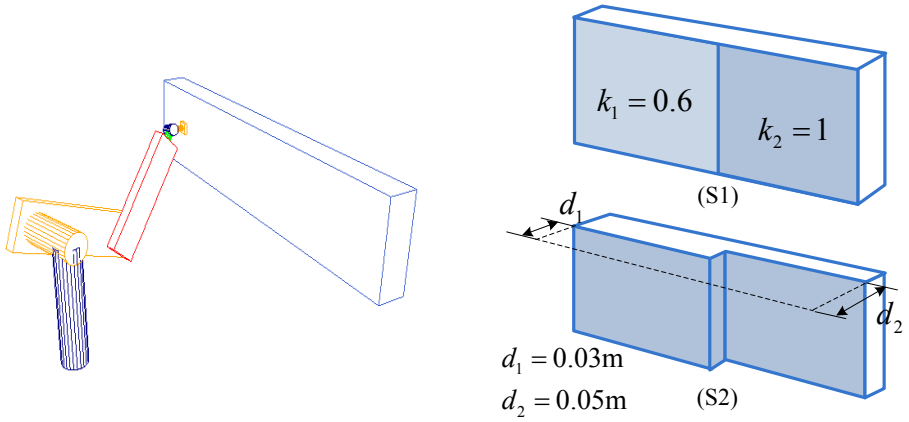

Figure 3.10 Simulation configuration for the UV irradiation process

The robot manipulator and the 2D rectangular target are illustrated in Figure 3.10(a). The spatial path of the end effector is designed as a linear one, starting from the left side of the target to the right side. The UV source (an LED panel) model is developed based on equation (3.9). The output variable of the source model is the irradiance distribution on the target. The input variables include the radiant flux and the relative geometric configuration of the UV LED panel. Two simulation scenarios (shown in Figure 3.10(b)) will be conducted to demonstrate the online trajectory generation method. In the first scenario (S1), the target surface is divided into two regions with different UV absorption coefficients (denoted by k_1 and k_2). In the second scenario (S2), the variation ($d_2 > d_1$) occurs in the distance between the target surface and the moving actuator. The two scenarios represent typical disturbances existing in the curing process caused by

material and geometric factors, such as uneven paint, finishing variations, etc. The two online trajectory generation strategies ("look-and-move" and "run-by-run") described in Section 3.2 are applied to robotic curing system in these scenarios, and then compared with the open-loop curing method (the trajectory is pre-determined). The simulation results for the first scenario are given in Figure 3.11 ~ Figure 3.13.

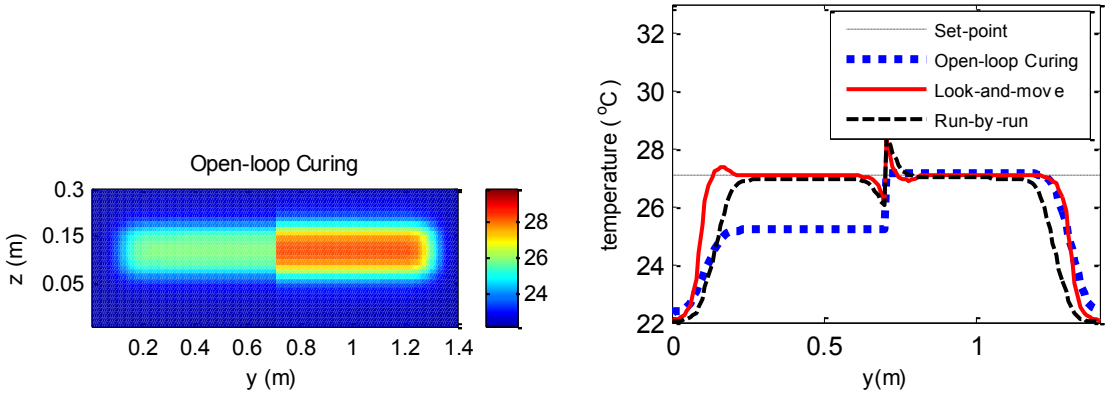

Figure 3.11 (a) Temperature map of the target, open-loop curing (b) Temperature distribution along the centerline for the three methods (Scenario-1)

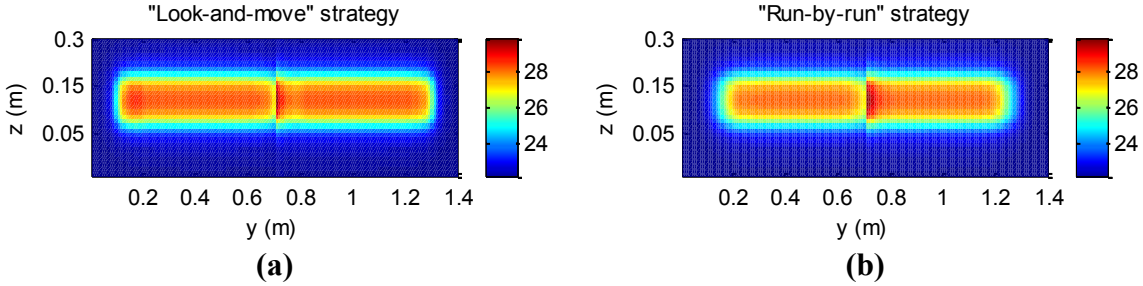

Figure 3.12 (a) Temperature map of the target, "look-and-move" strategy (b) Temperature map of the target, "run-by-run" strategy (Scenario-1)

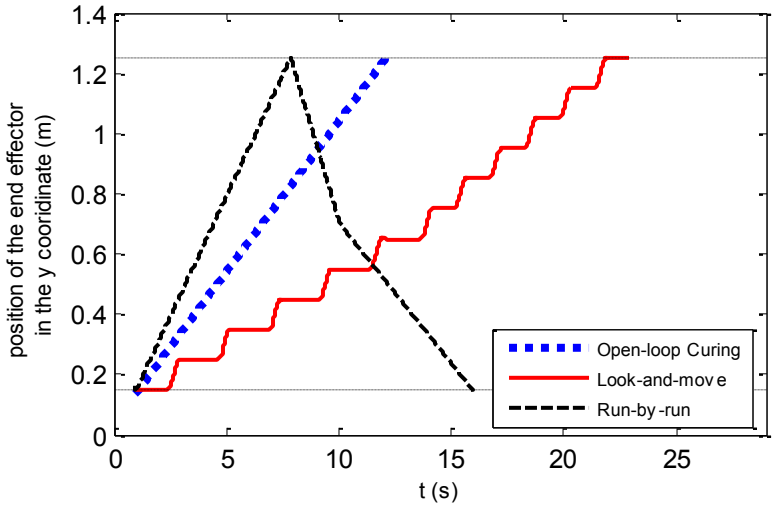

Figure 3.13 Trajectory of the end effector for the three methods (Scenario-1)

The temperature map illustrated in Figure 3.11(a) shows that the open-loop curing method cannot maintain process uniformity due to the uneven distribution of the UV absorption coefficient along the target in Scenario-1. The process uniformity is improved by implementing the two online trajectory generation strategies, as seen from the temperature maps in Figure 3.12 (a) and (b). There is only a slight unevenness occurring at the intermediate area between the left and right parts of the target. The comparison of the temperature distribution along the centerline of the target among the three curing methods is presented in Figure 3.11(b). The trajectories of the robot end effector for the three methods are depicted in Figure 3.13. Compared to the open-loop curing method which employs a constant moving speed, the look-and-move strategy reduces the duration of curing at each segment when the actuator begins illuminating the area with higher UV absorption coefficient. Similarly, the run-by-run strategy uses two different velocities when the actuator sweeps back (the second run) to compensated for the uneven

UV absorption distribution. The simulation results for the second scenario are illustrated in Figure 3.14 ~ Figure 3.16.

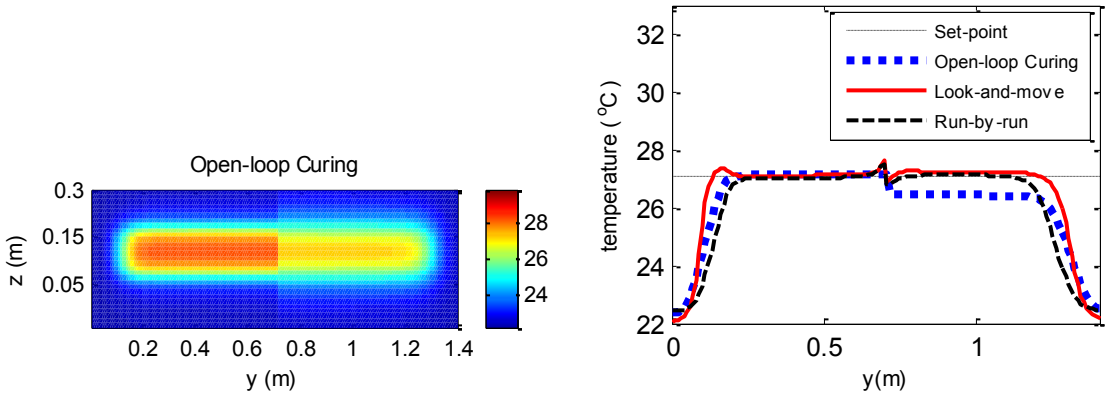

Figure 3.14 (a) Temperature map of the target, open-loop curing (b) Temperature distribution along the centerline for the three methods (Scenario-2)

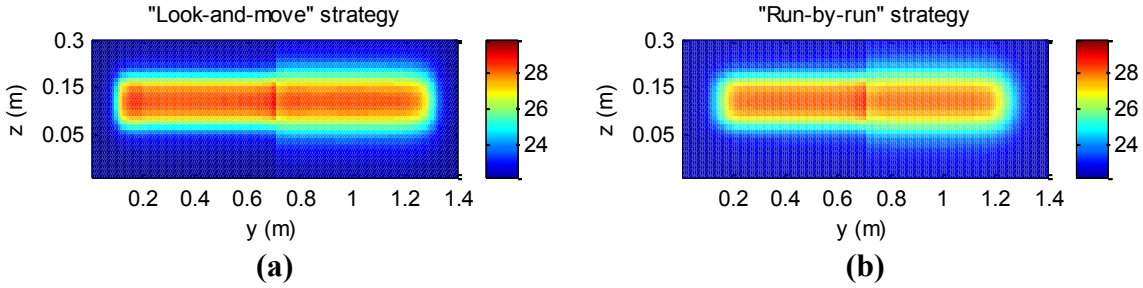

Figure 3.15 (a) Temperature map of the target, “look-and-move” strategy (b) Temperature map of the target, “run-by-run” strategy (Scenario-2)

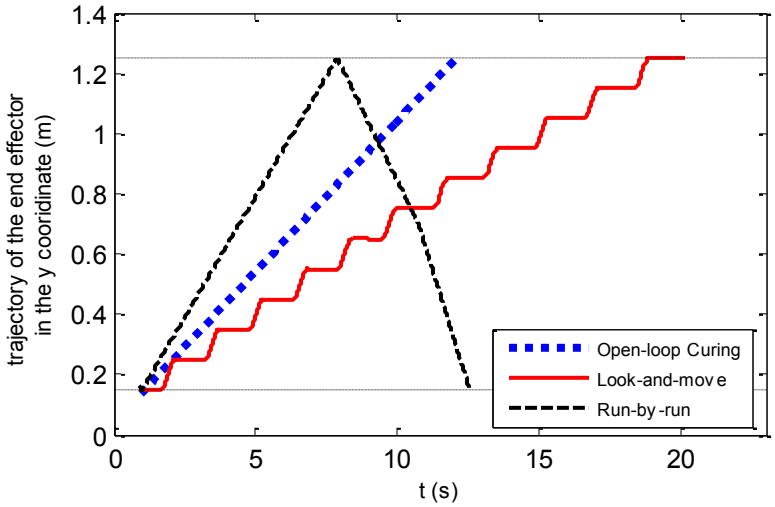

Figure 3.16 Trajectory of the end effector for the three methods (Scenario-2)

In Scenario-2, the open-loop curing method fails to maintain the process uniformity due to the varying distance between the actuator and the target. The improved results by using the two online trajectory strategies are presented in Figure 3.15. This can be explained by the trajectory adjustment illustrated in Figure 3.16. The look-and-move strategy increases the duration of curing at each segment when the end effector enters the area with a larger distance to the target. The run-by-run strategy also adjusts the speed of the end effector adaptively to compensate for the distance variations.

The two scenarios discussed above demonstrate that the proposed online trajectory generation method can help improve process uniformity in the presence of different types of disturbances.

3.4.3 Application of the Temperature Feedback Control

This subsection presents the implementation of the temperature feedback control strategy discussed in Subsection 3.3.2 to the robotic UV curing process through

simulation. Two infrared (IR) cameras are used to provide the local and global temperature measurements in this application. The feedback signals corresponding to the local and global configurations are generated based on the average method described by equation (3.8). The detailed feedback signal generation is given below:

$$\bar{T}(t) = \frac{1}{(i_{ub} - i_{lb} + 1)(j_{ub} - j_{lb} + 1)} \sum_{j=j_{lb}}^{j_{ub}} \sum_{i=i_{lb}}^{i_{ub}} T(i, j) \tag{3.13}$$

In equation (3.13), the average temperature is denoted by $\bar{T}(t)$, which is calculated within the following defined processing window for the local and global cameras, respectively.

Local Processing Window:
$$\begin{aligned} i_{lb} &= i(x_a) - \omega_{Lx},\ i_{ub} = i(x_a) + \omega_{Lx}, \\ j_{lb} &= j(y_a) - \omega_{Ly},\ j_{ub} = j(y_a) + \omega_{Ly} \end{aligned} \tag{3.14}$$

Global Processing Window:
$$\begin{aligned} i_{lb} &= \left[i(x_a) - \delta\right] - \omega_{Gx},\ i_{ub} = \left[i(x_a) - \delta\right] + \omega_{Gx}, \\ j_{lb} &= j(y_a) - \omega_{Gy},\ j_{ub} = j(y_a) + \omega_{Gy} \end{aligned} \tag{3.15}$$

Again, the current position of the actuator is described by x_a and y_a. This is also the center of the local processing window. The length and width of the local processing window are defined by $2\omega_{Lx}$ and $2\omega_{Ly}$, respectively. The center of the global processing window is shifted in the opposite direction of the actuator's movement by a distance δ, to make sure that the global camera only processes data from the cured area. The length and width of the global processing window are defined by $2\omega_{Gx}$ and $2\omega_{Gy}$, respectively.

The cascade controller discussed in Subsection 3.3.2 is detailed for this application. Two proportional–integral–derivative (PID) controllers are used to regulate

both the local and global temperature levels. The cascade controller can manipulate either the radiant power of the actuator or the speed of the end effector. The two alternative control structures are illustrated in Figure 3.17.

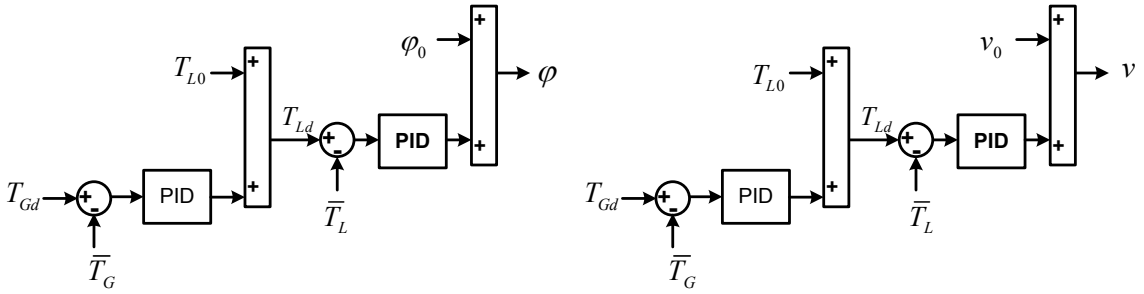

(a) Radiant Power Control **(b) Speed Control**

Figure 3.17 Two alternative structures of the cascade PID controller

In Figure 3.17, the global temperature set-point and the measured average temperature through the global camera are denoted by T_{Gd} and $\overline{T}_G$, respectively. The first PID controller is used to adjust the local temperature set-point T_{Ld} around a nominal value T_{L0}. The measured average temperature through the local camera is represented by $\overline{T}_L$, which is compared with T_{Ld} to determine either the radiant power or the speed. The nominal speed and radiant power are denoted by v_0 and φ_0, respectively. The above two control approaches are demonstrated by using the scenarios described in the previous subsection. The simulation results for Scenerio-1 are given in Figure 3.18 ~ Figure 3.20.

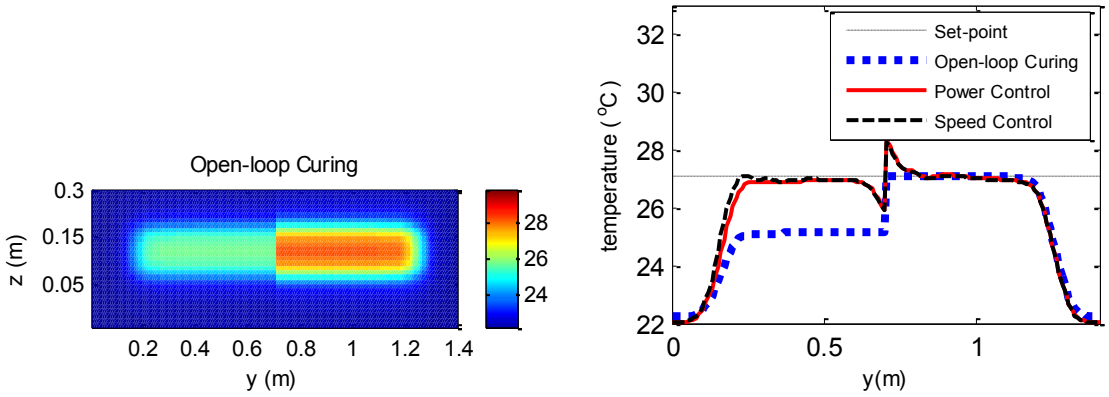

Figure 3.18 (a) Temperature map of the target, open-loop curing (b) Temperature distribution along the centerline for open-loop and feedback control (Scenario-1)

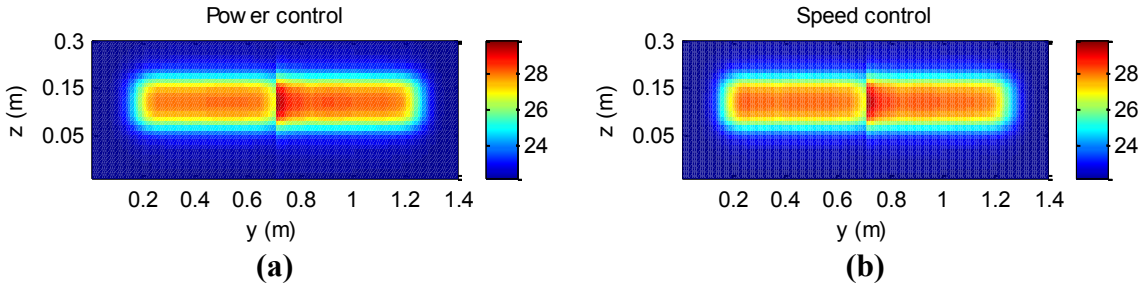

Figure 3.19 (a) Temperature map of the target, using power control (b) Temperature map of the target, using speed control (Scenario-1)

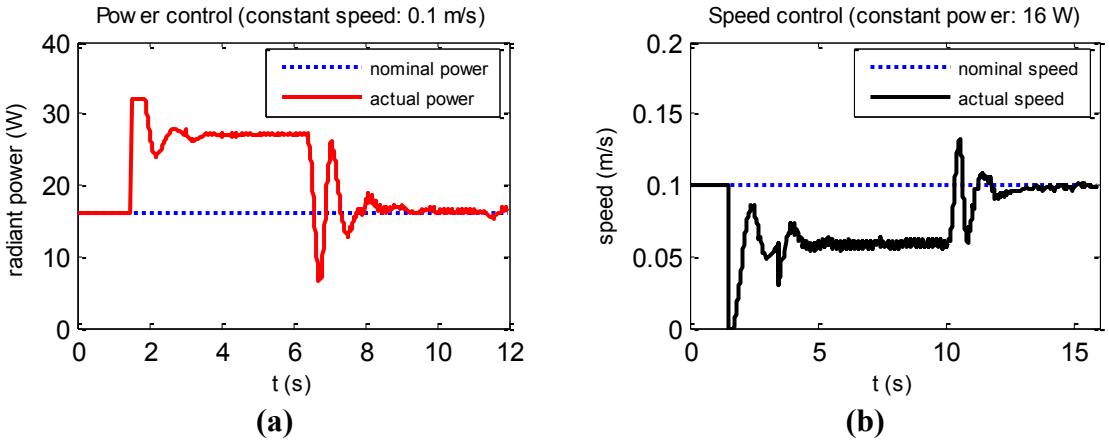

Figure 3.20 Time history of the power and the speed of the UV source (Scenario-1)

The temperature maps depicted in Figure 3.19 and the temperature distribution along the centerline illustrated in Figure 3.18(b) show that the uneven UV absorption distribution can be compensated for by adjusting either the power or the speed of the UV source based on the local and global temperature feedback. This can be explained by the time history of the power and the speed of the UV source shown in Figure 3.20. In the power control strategy, a constant speed is used and the radiant power is adjusted around a nominal value. The time history in Figure 3.20(a) shows that a higher radiant power is applied when the UV source passes the area with lower absorption coefficient. This manipulation is equivalent to the speed decrease shown in Figure 3.20(b). For the speed control approach, the radiant power is kept constant during the whole process.

The simulation results for Scenario-2 are presented in Figure 3.21 ~ Figure 3.23.

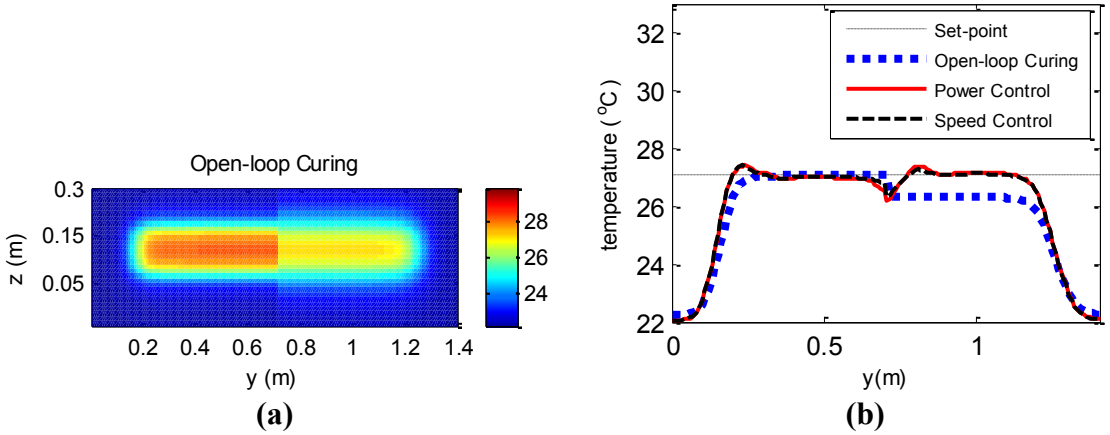

Figure 3.21 (a) Temperature map of the target, open-loop curing (b) Temperature distribution along the centerline for open-loop and feedback control (Scenario-2)

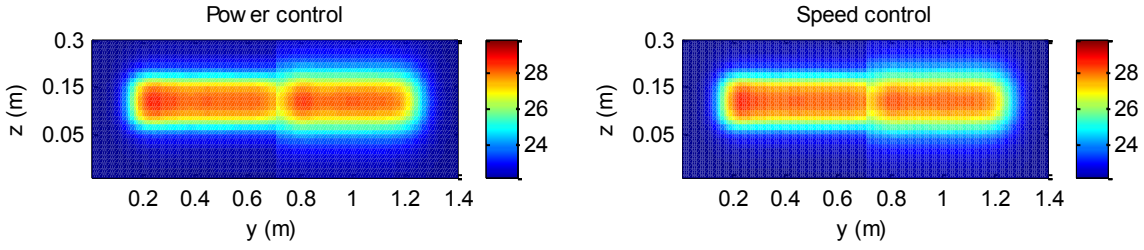

Figure 3.22 (a) Temperature map of the target, using power control (b) Temperature map of the target, using speed control (Scenario-2)

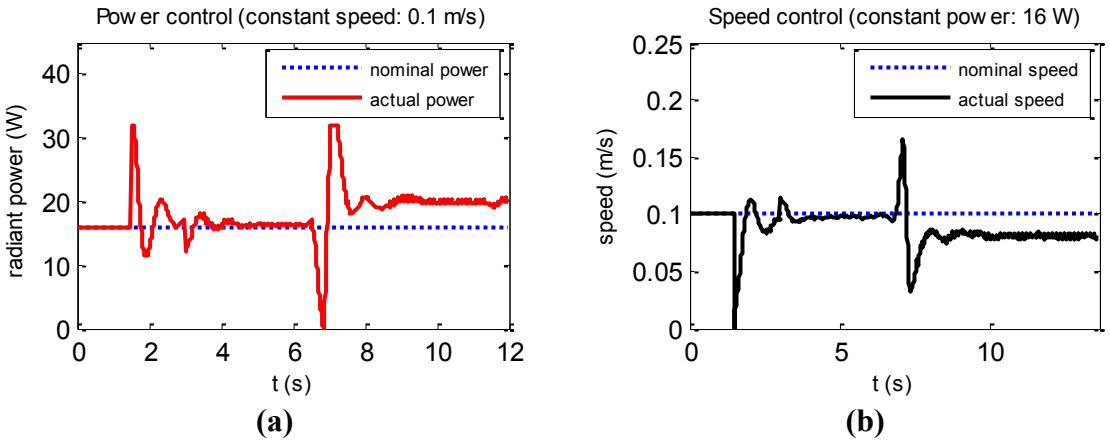

Figure 3.23 Time history of the power and the speed of the UV source (Scenario-2)

In this scenario as well, the unevenness caused by the varying distance can also be reduced with either the power or speed control strategies. The time history of the power and the speed of the UV source given in Figure 3.23 shows that the distance increase is compensated for by applying higher radiant power or reducing the speed of the UV source.

The above simulation results for the two different scenarios demonstrate that these temperature feedback control strategies can significantly improve the process uniformity by manipulating either the radiant power or the speed of the moving actuator.

3.5 Experimental Platform Development

This section presents the development of an experimental platform which can be used to validate some of the methods and strategies described in the previous sections for the UV curing process. The developed experimental system also provides a basic platform for conducting relevant research on robotic UV curing and other radiation-based processes. The general structure of this experimental platform is illustrated in Figure 3.24.

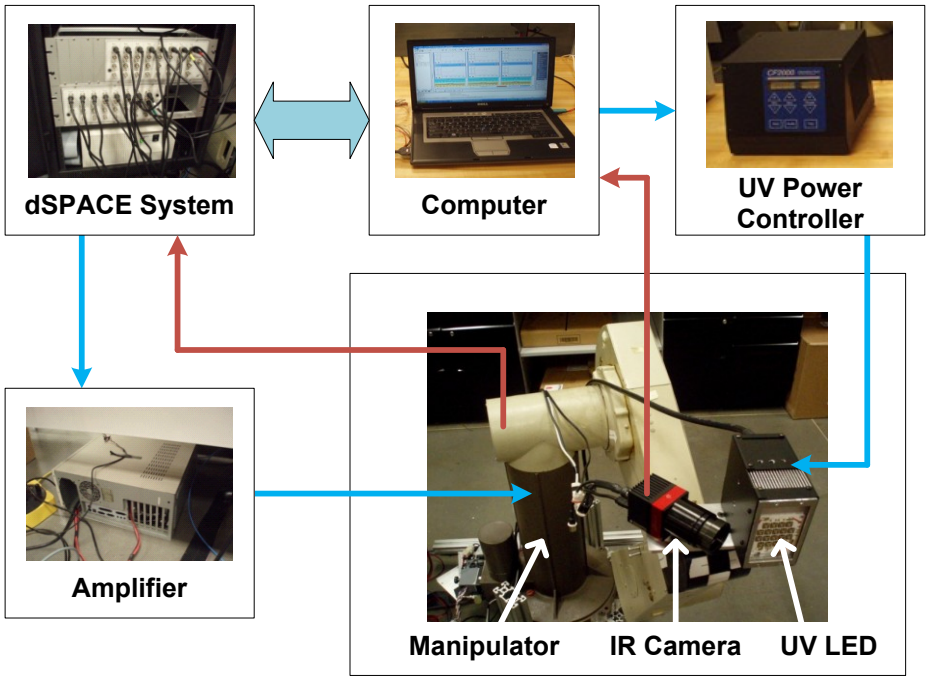

Figure 3.24 The general structure of the experimental platform

As shown in Figure 3.24, the experimental platform is composed of three basic parts: a manipulator system, a UV radiation system, and a thermal vision system. All of these systems are coordinated by a dSPACE rapid control prototyping system and a computer. The three subsystems are detailed below.

3.5.1 Manipulator System

A six degree-of-freedom (DOF) PUMA560 manipulator is used in this experimental platform. The original servo drives of the manipulator have been replaced by six new pulse-width modulation (PWM) amplifiers. These amplifiers are controlled by the dSPACE system to drive the motor of each joint in such a way that the end effector of the manipulator can follow the desired trajectory. The control structure of the manipulator system is illustrated in Figure 3.25.

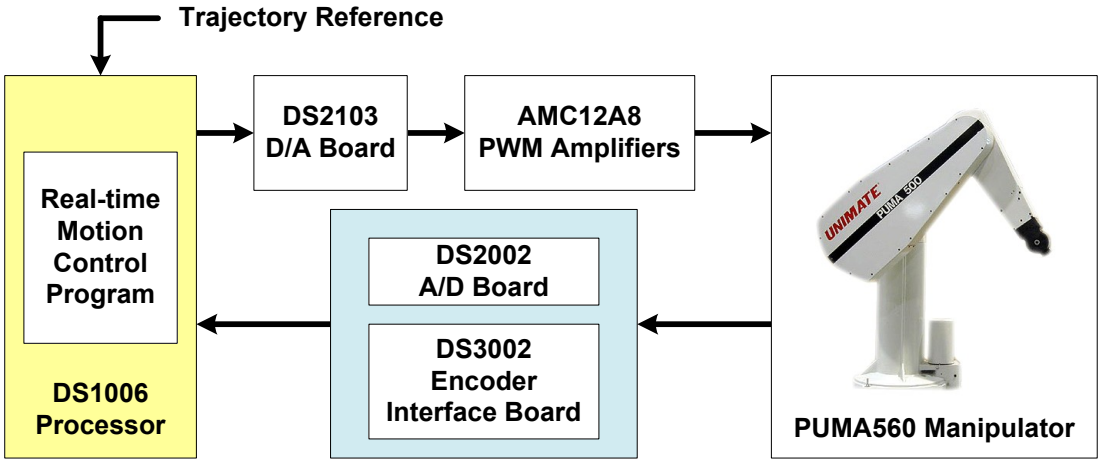

Figure 3.25 The control structure of the manipulator system

In the control structure shown in Figure 3.25, the joint position signals are captured by six built-in encoders and sent to the controller through an encoder interface board and an analog-to-digital (A/D) board. The central processor, directed by the real-time motion control program, calculates the control signal based on the trajectory reference and the motion feedback. The amplifiers obtain the converted control signal from a digital-to-analog (D/A) board and drive the manipulator to follow the desired trajectory.

3.5.2 UV Radiation System

The UV radiation system is composed of a Clearstone 42-cell UV LED head and the associated power controller. This UV LED head can be turned on/off instantly and has suitable shape factor for mobile use. The dominant emission wavelength of the LED head is 365 nm and its maximum power is 16.1 W. The LED head is connected with a CF2000 power controller which provides various options for manipulating the output of the UV power. The control structure of the UV radiation system is depicted in Figure 3.26.

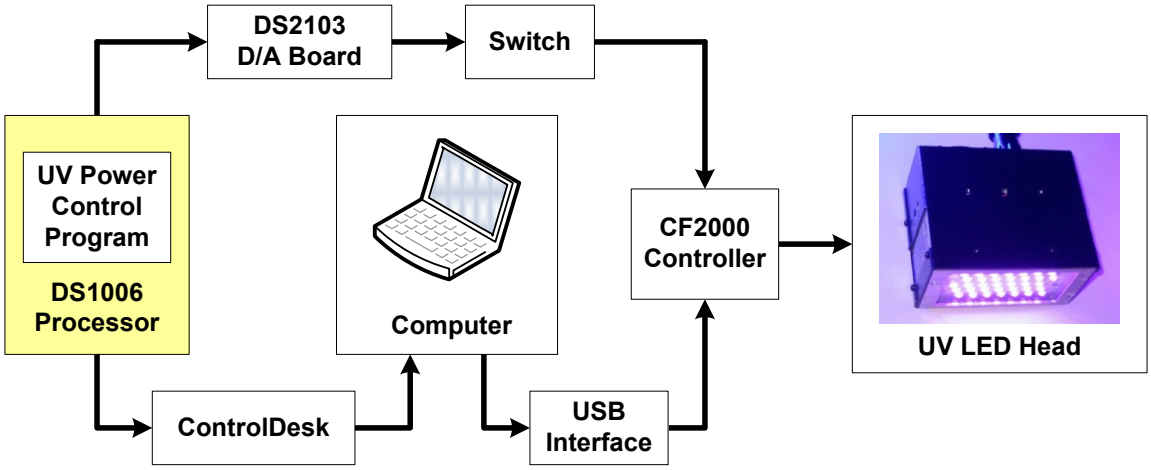

Figure 3.26 The control structure of the UV radiation system

As illustrated in Figure 3.26, the dSPACE processor has two channels to control the UV LED Head. It can either send a simple on/off command to the CF2000 power controller through DS2103 D/A board and a switch, or adjust the UV power level from zero to its maximum value through ControlDesk (software package associated with the dSPACE system), the computer and the USB interface.

3.5.3 Thermal Vision System

A thermal vision system is utilized in this platform to capture the temperature distribution on the target surface. The main component of this system is a Thermoteknix infrared (IR) camera. It has a 640×320 pixel array and can measure the temperature range from -20 to 150 °C. This camera can communicate with the computer through the USB interface and send out digital video at a frame rate of 30 Hz. The captured thermal images are processed as a series of 640×320 matrices in MATLAB/Simulink and then converted to real-time temperature signals. The basic structure of the thermal vision system is shown in Figure 3.27.

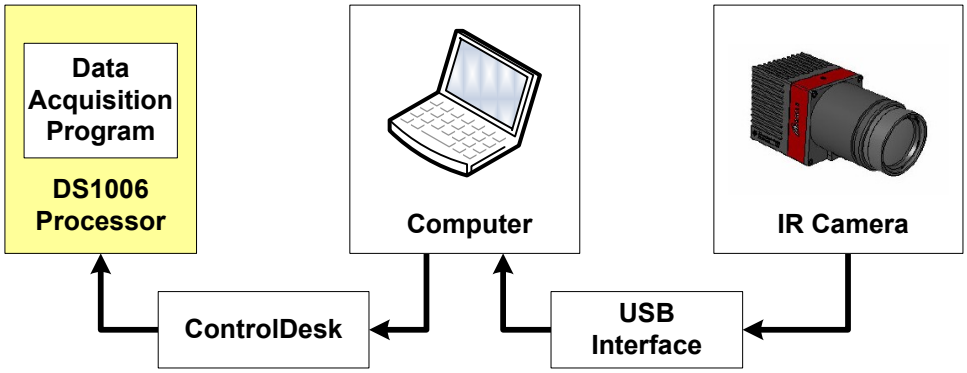

Figure 3.27 The structure of the thermal vision system

In the actual system, the IR camera is connected with the computer through two USB cables, one of which is used to transfer thermal images and the other carries the control signal. The image processing is performed in the computer and the converted temperature signal is sent to the central processor of the dSPACE system through a cross-over patch cable and ControlDesk interface. The thermal vision system provides essential

temperature feedback information for the control system to manipulate the motion of the robot or the power of the UV LED head.

3.5.4 Preliminary Experiments

In this subsection, some preliminary experiments including the sample curing test and the demonstration of the look-and-move strategy will be presented. In the sample curing test, the open-loop characteristics of the UV irradiation and the photo-initiated polymerization are evaluated. This is followed by an experimental demonstration of one of the online trajectory generation strategies (look-and-move), in which the motion of the robot end effector is adjusted in real-time by using local temperature feedback through the thermal vision system.

- Sample Curing Test

The UV curable paint material used in this test is provided by Red Spot Paint & Varnish Corporation. This formulation is typically utilized as a protective clearcoat for parts made out of polycarbonate. In this test, the paint is applied to some plastic substrates through an adjustable micrometer film applicator. The substrate and the applicator are illustrated in Figure 3.28.

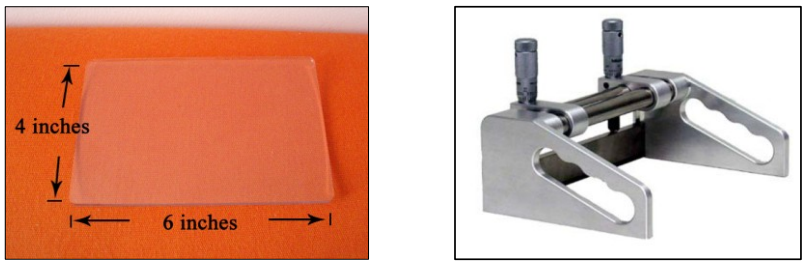

(a) Substrate (b) Film Applicator

Figure 3.28 The substrate and the film applicator

The objective of the sample curing test is to obtain the open-loop characteristics of the UV radiation and the photo-initiated polymerization. Two parameters that can significantly influence the curing performance are considered in this test: the curing time and the distance between the UV LED head and the painted substrate. The degree of cure conversion is evaluated through Fourier Transform Infrared (FTIR) Spectrometry [99]. The results of the sample curing test are given in Figure 3.29 ~ Figure 3.30.

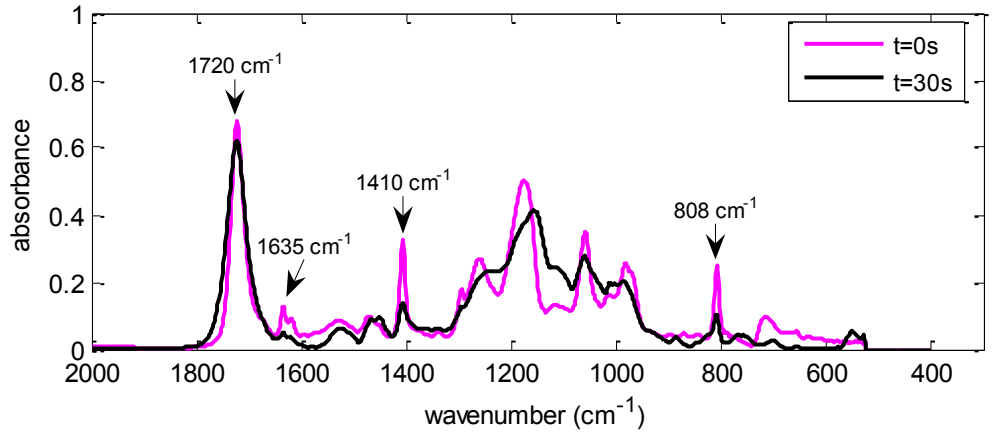

Figure 3.29 FTIR spectra of the painted samples (film thickness: 5 mils; distance to UV LED: 0.0254m) at different curing time (t=0s and t=30s)

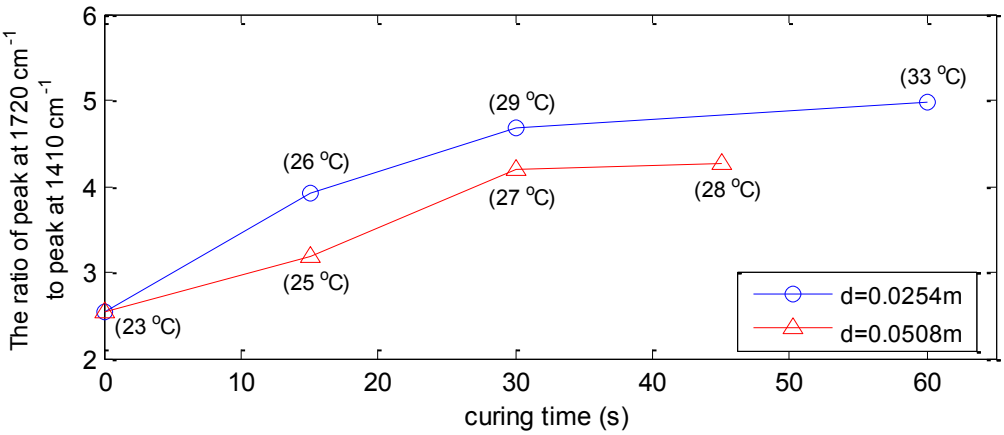

Figure 3.30 The degree of cure conversion versus curing time for different distances between the sample and the UV LED head (d=0.0254m and d=0.0508m)

Generally, the degree of cure conversion for acrylate materials can be obtained by monitoring the decrease of the peak of the absorbance band at 1635, 1410, and 808 cm^{-1} [100], using the IR spectra shown in Figure 3.29. In this test, the absorbance band at 1410 cm^{-1} is used to determine the degree of cure. The evolution of the relative absorbance (the ratio of peak at 1720 cm^{-1} to 1410 cm^{-1}) for different distances is shown in Figure 3.30. The associated temperature measurements are also indicated. It can be observed that a shorter distance results in a higher degree of cure conversion at the same curing time. Another observation from Figure 3.30 is that the major curing conversion occurs within the first 30 seconds during the curing process. Given the results of the sample curing test, the set-point for the temperature feedback control can be selected as 29 ° C, which gives an acceptable degree of cure conversion for the defined curing configuration (film thickness: 5 mils; distance to UV LED: 0.0254 m).

- Demonstration of the look-and-move strategy

The look-and-move strategy is selected for experimental demonstration because it is suitable for the relatively slow curing process (30s) in this particular application and paint specimen. The paint is applied to a rectangular plastic substrate and a straight-line path is designed for the PUMA560 manipulator to complete the curing task. This demonstration is performed on the developed experimental platform and the configuration of the actual curing system for the look-and-move strategy is illustrated in Figure 3.31.

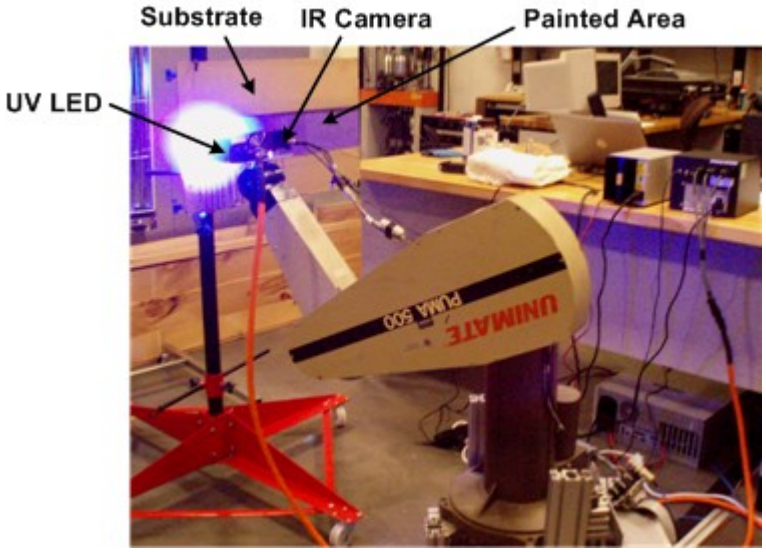

Figure 3.31 System configuration for the look-and-move strategy

The painted area along the path of the end effector is divided into six segments. The length of each segment is set as 0.09m, which is slightly shorter than the length of the UV LED head. This can help improve the cure uniformity at the intermediate area between two adjacent segments due to the overlap effect. The UV LED is turned off when it moves from one segment to the next. The curing duration for each segment is calculated online by the dSPACE controller that employs temperature feedback and the look-and-move strategy. The experimental results are illustrated in Figure 3.32.

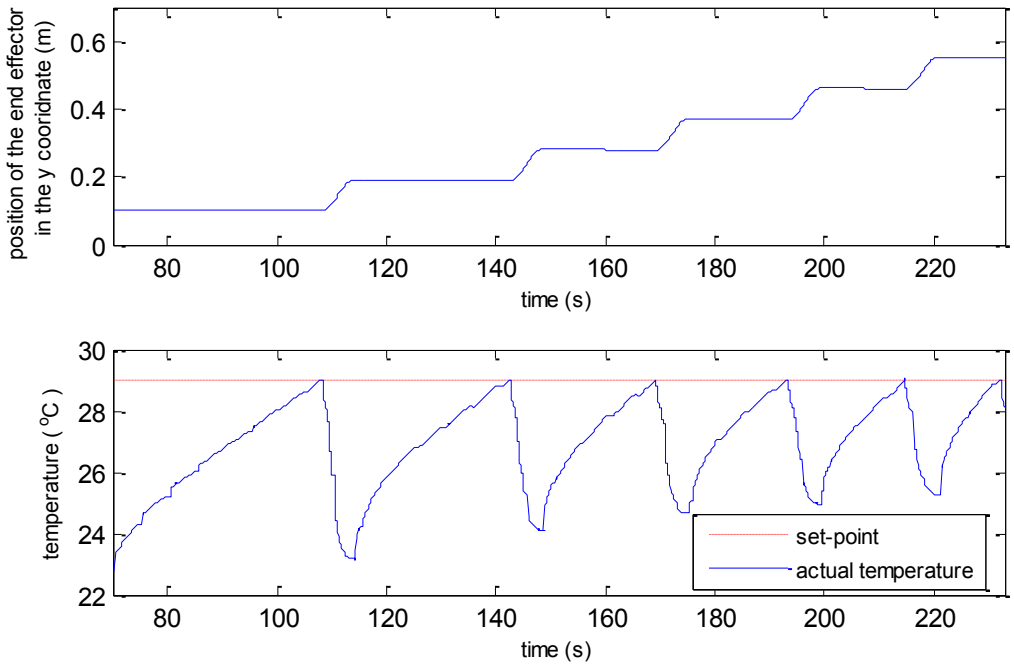

Figure 3.32 Trajectory of the end effector and time history of temperature signal

As shown in Figure 3.32, a curing cycle starts when the end effector just arrives at a segment to be cured. The curing of this segment is complete when the measured temperature level reaches the set-point. The decrease of curing duration from the first to the final segment can be explained by the fact that future segments have already received some UV radiation from the LED head which stays at the current location. Therefore, the controller reduces the curing duration gradually when the LED head processes the subsequent segments. This can help maintain the cure uniformity and improve curing quality.

Chapter Summary

This chapter discussed two important issues in developing closed-loop control approaches for practical robotic radiation-based processes: online trajectory generation

and process output feedback control. Two online trajectory generation strategies, using either the local or global measurement of some process outputs, were developed for two discrete process configurations. A basic output feedback control method was then developed to deal with the continuous process configuration by adjusting the power or the speed of the radiation actuator based on the combined local and global measurements. Both the online trajectory generation method and the output feedback control strategy were demonstrated on a robotic UV curing process through simulation. The results showed that these closed-loop approaches succeed in compensating for disturbances and maintaining process uniformity. The development of an experimental platform for demonstrating these methods and strategies was also discussed in this chapter.

It should be noted that although the online trajectory generation method and the output feedback control strategy were developed based on existing feedback control theories and methods, they focused on addressing the closed-loop control issue for a class of robotic radiation-based processes in a practical manner. The following chapters will discuss the estimation and coordination issues based on a more generic description of these robotic radiation-based processes.

CHAPTER FOUR

DISTRIBUTED STATE AND PARAMETER ESTIMATION

The online trajectory generation method and feedback control strategy discussed in the previous chapter assume that the measured process outputs (e.g. temperature) are highly relevant to the state variables to be controlled (e.g. cure-conversion level). Sometimes, the correlation between the output measurements and the controlled state variables may be influenced by disturbances. For example, the temperature change during the curing process is not only determined by the heat generated from the polymerization reaction, but it is also influenced by conductive and convective heat transfer components. Therefore, it is necessary to monitor the controlled state variables directly.

However, since the direct measurements of the controlled state variables are not always available due to the lack of robust and cost-effective sensing alternatives, state/parameter estimation is needed to obtain such information. For robotic radiation-based processes, two significant issues should be addressed in the development of an estimation scheme. First, these processes are typically described as distributed-parameter systems with a number of state variables. This may increase the computational cost for estimation. Second, with moving actuators, the observability depends on the motion and location of the actuator. This changing observability will have a significant influence on the estimation performance.

This chapter will discuss the estimation problem in consideration of the two issues described above, based on a generalized distributed-parameter description of these robotic radiation-based processes. In this formulation, these processes are simplified as a

1D scanning problem, in which the radiant actuator is modeled as a point source and the processed target is represented by a 1D strip. A distributed state and parameter estimation scheme that incorporates a dual extended Kalman filter (DEKF) is then developed. The implementation of the developed estimation scheme is also detailed, including the design of an activating policy for reducing computational cost and compensating for observability changes. The developed estimation scheme is finally demonstrated on a model of the robotic UV curing process.

4.1 Problem Formulation

Although most robotic radiation-based processes involve geometrically complex objects, such as aircrafts, automobiles, etc., the major process evolution considered here occurs in the direction of the movement of the actuator. In addition, the spatial path of the moving actuator is usually designed parallel to the geometric profile of the target, and the actuator itself is comparatively smaller than the processed target. With these assumptions, the actual process can be simply treated as a general 1D scanning problem illustrated in Figure 4.1.

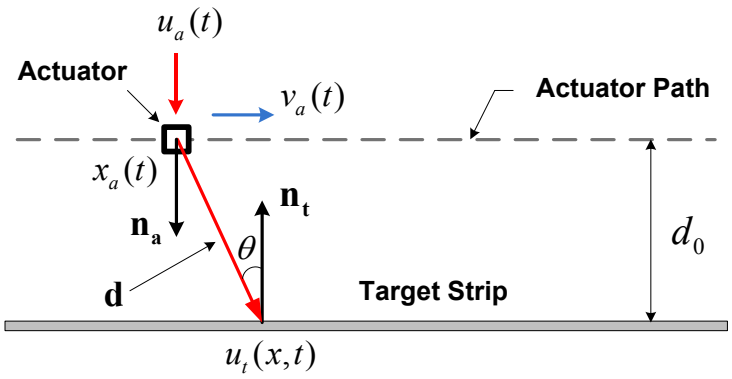

Figure 4.1 The general 1D scanning problem

As shown in Figure 4.1, the moving actuator is simplified as a point source. The spatial coordinate and the time are represented by x and t. The input power and the speed of the actuator are denoted by $u_a(t)$ and $v_a(t)$, respectively. The term $u_t(x,t)$ represents the distribution of the power density on the target strip. The two normal vectors ($\mathbf{n_a}$ and $\mathbf{n_t}$) and the position vector $\mathbf{d}$ characterize the relative geometric configuration between the actuator and the target strip. The normal distance between the path of the actuator and the target strip is denoted by d_0.

The 1D scanning problem illustrated in Figure 4.1 describes the energy transmission phase included in most robotic radiation-based processes. The mathematical description of this phase is given by a nonlinear function in equation (4.1). Similarly, the two other essential phases of these processes, namely state evolution and co-evolution, can be represented by equation (4.2) and equation (4.3).

$$u_t(x,t) = f_{ET}\left[u_a(t),\ v_a(t),\ \mathbf{p}_{ET}\right] \tag{4.1}$$

$$\frac{d\boldsymbol{\omega}(x,t)}{dt} = f_{ST}\left[\boldsymbol{\omega}(x,t),\ u_t(x,t),\ \mathbf{p}_{ST}\right] \tag{4.2}$$

$$\frac{d\boldsymbol{\zeta}(x,t)}{dt} = f_{CE}\left[\boldsymbol{\zeta}(x,t),\ \boldsymbol{\omega}(x,t),\ u_t(x,t),\ \mathbf{p}_{CE}\right] \tag{4.3}$$

Here, the nonlinear functions used to describe the energy transmission, the state evolution, and the co-evolution phases are denoted by $f_{ET}(\cdot)$, $f_{ST}(\cdot)$, and $f_{CE}(\cdot)$, respectively. The variables involved in the state evolution and the co-evolution phases are represented by the two vectors $\boldsymbol{\omega}(x,t)$ and $\boldsymbol{\zeta}(x,t)$. The parameters associated with the three phases are denoted by three vectors $\mathbf{p}_{ET}$, $\mathbf{p}_{ST}$, and $\mathbf{p}_{CE}$, respectively. In the

following subsections, two particular robotic radiation-based processes are provided as examples of the above general formulation of the 1D scanning problem.

4.1.1 Robotic UV Curing Process

The energy transmission phase of the UV curing process, namely the irradiation phase, has been discussed in Subsection 3.4.1 in Chapter 3. The 1D form of the model of the irradiation phase can be re-written as [97, 98]:

$$I(x,t) = k(x)\frac{\varphi(t)\left[\cos\theta(x,t)\right]^2}{\pi\left|\mathbf{d}(x,t)\right|^2} \tag{4.4}$$

Here, the irradiance distribution on the target strip is denoted by $I(x,t)$. The absorption coefficient and the radiant flux of the source are represented by $k(x)$ and $\varphi(t)$, respectively. The orientation angle and the position vector are denoted by $\theta(x,t)$ and $\mathbf{d}(x,t)$, respectively. Given the geometric configuration shown in Figure 4.1, the irradiance distribution can be further described by:

$$I(x,t) = k(x)\frac{\varphi(t)d_0^2}{\pi\left\{\left[x_a(t)-x\right]^2+d_0^2\right\}^2} = k(x)\frac{\varphi(t)d_0^2}{\pi\left\{\left[\int_0^t v_a(\tau)d\tau - x\right]^2+d_0^2\right\}^2} \tag{4.5}$$

In equation (4.5), the oriental angle $\theta(x,t)$ and the position vector $\mathbf{d}(x,t)$ are represented by the normal distance (d_0) between the path of the actuator and the target strip, and the current position ($x_a(t)$) of the actuator that can be further represented by the integral of the actuator's speed $v_a(t)$. The UV irradiation on the target strip initiates

the state evolution phase of the curing process, which can be characterized by the following equations [101, 102].

$$\frac{d[PI](x,t)}{dt} = -\phi\varepsilon[PI](x,t)I(x,t) \tag{4.6}$$

$$\frac{d[M](x,t)}{dt} = -\kappa\left(\phi\varepsilon\right)^{0.5}[M](x,t)\left\{[PI](x,t)I(x,t)\right\}^{0.5} \tag{4.7}$$

$$\kappa = k_p / k_t^{0.5} \tag{4.8}$$

Equation (4.6) describes initiation kinetics of the UV induced polymerization, in which the photo-initiators absorb the UV irradiation and form a few free radicals to induce the crosslink reaction. The photo-initiator concentration is denoted by $[PI](x,t)$. The two coefficients ϕ and ε represent the quantum yield of initiation and the molar absorptivity, respectively. The kinetics of the propagation and termination of the polymerization are described by equation (4.7), where the monomer concentration is denoted by $[M](x,t)$. The coefficient κ is composed of the propagation rate constant k_p and the termination rate constant k_t. The differential equation in (4.6) can be solved to obtain the following explicit expression of the photo-initiator concentration $[PI](x,t)$.

$$[PI](x,t) = [PI](x,t_0)\, e^{-\phi\varepsilon\int_0^t I(x,\tau)d\tau} \tag{4.9}$$

Substituting equation (4.9) into equation (4.7) yields:

$$\frac{d[M](x,t)}{dt} = -\kappa\left\{\phi\varepsilon[PI](x,t_0)\right\}^{0.5}[M](x,t)\left[I(x,t)\, e^{-\phi\varepsilon\int_0^t I(x,\tau)d\tau}\right]^{0.5} \tag{4.10}$$

The co-evolution phase of the UV curing process involves the temperature increase of the target strip due to the accumulated radiation energy and the heat generated from polymerization reaction. A general thermal dynamic equation can be used to describe the co-evolution phase [102].

$$\rho c \frac{\partial T(x,t)}{\partial t} = \frac{\partial}{\partial x}\left[\lambda \frac{\partial T(x,t)}{\partial x}\right] - \Delta H \frac{d[M](x,t)}{dt} - h\left[T(x,t) - T_{\infty}\right] + \varepsilon [PI](x,t_0)\, e^{-\phi\varepsilon \int_0^t I(x,\tau)d\tau} I(x,t) \tag{4.11}$$

Here, the temperature distribution along the target strip is represented by $T(x,t)$. The density and specific heat capacity are denoted by ρ and c, respectively. The right hand side of equation (4.11) considers both the conductive and convective heat transfer, the heat generation from the polymerization, and the radiation from the UV source. The conductive and convective heat coefficients are represented by λ and h. The polymerization enthalpy and the ambient temperature are denoted by ΔH and T_{∞}, respectively. The term $d[M](x,t)/dt$ can be eliminated by substituting equation (4.10) into equation (4.11).

Combing equations (4.5), (4.10), and (4.11), we can describe the robotic UV curing process in the form of the general 1D scanning problem discussed above:

$$I(x,t) = f_{ET}\left[\varphi(t),\ v_a(t),\ \{k(x),\ d_0\}^{\mathbf{T}}\right] \tag{4.12}$$

$$\frac{d[M](x,t)}{dt} = f_{ST}\left[[M](x,t),\ I(x,t),\ \{\kappa,\ \phi,\ \varepsilon,\ [PI](x,t_0)\}^{\mathbf{T}}\right] \tag{4.13}$$

$$\frac{dT(x,t)}{dt} = f_{CE}\left[T(x,t),\ [M](x,t),\ I(x,t),\ \{\rho,\ c,\ \lambda,\ h,\ \Delta H,\ \phi,\ \varepsilon,\ [PI](x,t_0)\}^{\mathbf{T}}\right] \tag{4.14}$$

It should be noted that the key states of the three essential phases of the UV curing process vary with both time and spatial coordinate. The spatial distribution of these state variables is significantly influenced by the movement of the actuator along the target strip. The estimation scheme to be developed should take into account this distributed characteristic.

4.1.2 Robotic IR Drying Process

The energy transmission phase of the IR drying process can be described in a similar way. Instead of using a UV source, the IR drying process employs a high-temperature lamp or LED to deliver energy to the target through thermal radiation. This thermal radiation process can be modeled as follows, according to the Stefan–Boltzmann Law [98] and Lambert's Cosine Law [97].

$$P(x,t) = \frac{\varepsilon_a \sigma A_a \left\{ \left[T_a(t) \right]^4 - T_\infty^4 \right\} \left[\cos\theta(x,t) \right]^2}{\pi \left| \mathbf{d}(x,t) \right|^2} \tag{4.15}$$

In equation (4.15), the power density (W/m^2) on the target strip is denoted by $P(x,t)$. The surface area and temperature of the IR source are represented by A_a and $T_a(t)$, respectively. The ambient temperature is represented by T_∞, and σ is the Stefan–Boltzmann constant. The emissivity factor of the IR source is denoted by ε_a. Using the moving speed ($v_a(t)$) and the normal distance between the source and the target (d_0), we can rewrite equation (4.15) as:

$$P(x,t)=\frac{\varepsilon_a \sigma A_a \left\{\left[T_a(t)\right]^4 - T_\infty^4\right\} d_0^2}{\pi\left\{\left[\int_0^t v_a(\tau)d\tau - x\right]^2 + d_0^2\right\}^2} \tag{4.16}$$

The thermal energy arriving at the target strip is mainly used to remove the moisture. The governing equation of the state evolution phase of the IR drying process can be expressed as [103, 104]:

$$\frac{\partial C_M(x,t)}{\partial t}=\frac{\partial}{\partial x}\left[D(C_M,T)\frac{\partial C_M(x,t)}{\partial x}\right]-S\left[C_M(x,t)-C_{Me}\right] \tag{4.17}$$

Here, the moisture concentration is represented by $C_M(x,t)$. The effective diffusion coefficient is denoted by $D(C_M,T)$, which is a function of the moisture concentration and temperature. The surface emission coefficient and the equilibrium moisture concentration are represented by S and C_{Me}, respectively. The co-evolution phase of the IR drying process can be described by the following energy balance equation:

$$\begin{aligned}\rho c\frac{\partial T(x,t)}{\partial t}=\frac{\partial}{\partial x}\left[\lambda\frac{\partial T(x,t)}{\partial x}\right]-h\left[T(x,t)-T_\infty\right]+P(x,t)\\ +L_v\frac{\partial C_M(x,t)}{\partial t}-\varepsilon_t\sigma\left\{\left[T(x,t)\right]^4-T_\infty^4\right\}\end{aligned} \tag{4.18}$$

In equation (4.18), the density ρ and the specific heat capacity c change with the varying moisture concentration. The conductive and convective heat transfer coefficients are denoted by λ and h, respectively. The latent heat of vaporization is represented by L_v, and the emissivity factor of the target strip is denoted by ε_t.

The three fundamental phases of the IR drying process can also be summarized in the general form described above:

$$P(x,t) = f_{ET}\left[T_a(t),\ v_a(t),\ \{\varepsilon_a,\ d_0\}^{\mathrm{T}}\right] \tag{4.19}$$

$$\frac{dC_M(x,t)}{dt} = f_{ST}\left[C_M(x,t),\ \{D(C_M,T),\ S\}^{\mathrm{T}}\right] \tag{4.20}$$

$$\frac{dT(x,t)}{dt} = f_{CE}\left[T(x,t),\ C_M(x,t),\ P(x,t),\ \{\rho,\ c,\ \lambda,\ h,\ L_v,\ \varepsilon_t\}^{\mathrm{T}}\right] \tag{4.21}$$

The above two examples (robotic UV curing and IR drying) illustrate how these robotic radiation-based processes are simplified as a general 1D scanning problem described by equations (4.1) ~ (4.3). The following section details the development of a distributed state and parameter estimation scheme that uses the dual extended Kalman filter (DEKF) based on this general formulation.

4.2 Dual Extended Kalman Filter Design

In this section, a distributed state and parameter estimation scheme is presented based on the generalized 1D formulation describing various robotic radiation-based processes. The proposed estimation scheme is based on the dual extended Kalman filtering (DEKF) theory reviewed in Chapter 2. The general structure of the DEKF estimation scheme designed for this problem is illustrated in Figure 4.2.

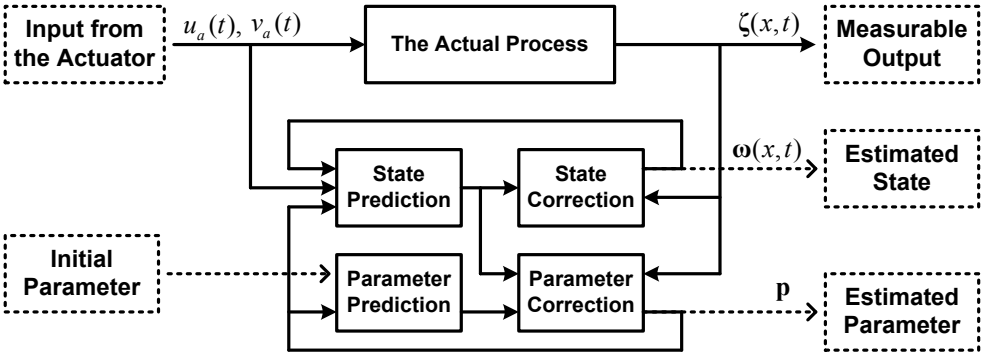

Figure 4.2 The structure of the DEKF estimation scheme

Here, the input power and the speed of the actuator are denoted by u_a and v_a, respectively. The state vector of the co-evolution phase (represented by $\boldsymbol{\zeta}(x,t)$) is taken as the measurable output of the process. The state estimation is applied to the state evolution phase of the process, and the state vector to be estimated is denoted by $\boldsymbol{\omega}(x,t)$. The parameter estimation may be applied to any of the three fundamental phases, and the parameter vector to be estimated (represented by $\mathbf{p}$) may include some unknown or uncertain components of parameter vectors ($\mathbf{p}_{ET}$, $\mathbf{p}_{ST}$, and $\mathbf{p}_{CE}$) associated with the energy transmission, state evolution and the co-evolution phases.

4.2.1 Development of the DEKF Estimation Scheme

The three fundamental phases described by equations (4.1) ~ (4.3) can be integrated into the following nonlinear discrete state-space form:

$$\mathbf{x}(j) = F\left[\mathbf{x}(j-1), \mathbf{u}(j-1), \mathbf{p}\right] + \mathbf{n}_{\mathbf{s}}(j-1) \tag{4.22}$$

$$\mathbf{y}(j) = C\mathbf{x}(j) + \mathbf{n}_{\mathbf{m}}(j-1) \tag{4.23}$$

$$\begin{aligned} &\mathbf{x}(j) = \left\{\boldsymbol{\omega}_1(j), \boldsymbol{\omega}_2(j), \cdots \qquad\qquad \cdots\right. \\ &\mathbf{u}(j-1) = \left\{u_a(j-1),\ v_a(j-1)\right\}^{\mathbf{T}},\ \mathbf{p} = \left\{\mathbf{p}_{ET}, \mathbf{p}_{ST}, \mathbf{p}_{CE}\right\}^{\mathbf{T}} \end{aligned} \tag{4.24}$$

Here, the process state at time j is represented by $\mathbf{x}(j)$, which is determined from the previous process state and input based on a nonlinear function $F(\cdot)$. The vector $\mathbf{x}(j)$ is formed by combining the state vectors of both the state evolution and the co-evolution phases. The two vectors ($\boldsymbol{\omega}(x,t)$ and $\boldsymbol{\zeta}(x,t)$) are discretized in both the temporal and spatial domains in equation (4.24). The target strip is divided into a series of spatial units, and the number of these units is denoted by N. The measured process output at time j is represented by $\mathbf{y}(j)$, which is a linear combination of the elements in the state vector $\mathbf{x}(j)$ through the matrix C. The vectors $\mathbf{n_s}(j-1)$ and $\mathbf{n_m}(j-1)$ denote the process and measurement noise, respectively. Here, they are assumed to be white and with normal probability distributions.

Given the above description of the process and associated measurement, the detailed DEKF estimation procedure for this problem is outlined as follows [105, 106].

Parameter Prediction:
$$\hat{\mathbf{p}}^{-}(j) = \hat{\mathbf{p}}(j-1) \tag{4.25}$$

State Prediction:
$$\hat{\mathbf{x}}^{-}(j) = F\left[\hat{\mathbf{x}}(j-1), \mathbf{u}(j-1), \hat{\mathbf{p}}(j-1)\right] \tag{4.26}$$

State Correction:
$$\hat{\mathbf{x}}(j) = \hat{\mathbf{x}}^{-}(j) + K_s\left[\mathbf{y}(j) - C\hat{\mathbf{x}}^{-}(j)\right] \tag{4.27}$$

Parameter Correction:
$$\hat{\mathbf{p}}(j) = \hat{\mathbf{p}}^{-}(j) + K_p\left[\mathbf{y}(j) - C\hat{\mathbf{x}}^{-}(j)\right] \tag{4.28}$$

Generally, the state and parameter estimation using the DEKF is performed through a two-step prediction/correction approach. The prediction step for the state and parameter is described in equations (4.25) and (4.26), respectively. The parameter prediction at time j ($\hat{\mathbf{p}}^{-}(j)$) is simply obtained by using the previous parameter estimate

($\hat{\mathbf{p}}(j-1)$). The state prediction at time j ($\hat{\mathbf{x}}^{-}(j)$) is achieved by calculating from the previous state estimate ($\hat{\mathbf{x}}(j-1)$) and the predicted parameter ($\hat{\mathbf{p}}^{-}(j)$) based on the nonlinear process model $F(\cdot)$. In the correction step, the final state and parameter estimates are obtained by correcting the predicted state and parameter, using the current process output measurement and online determined gain matrices. The two gain matrices (K_s and K_p) are calculated in an optimal manner to minimize the estimated error covariance for both states and parameters. The time-updated equations for calculating the gain matrices K_s and K_p are given by [105, 106]:

Update K_s *:*

$$\hat{P}_s^{-}(j) = \Phi \hat{P}_s(j-1)\Phi^{\mathrm{T}} + Q \tag{4.29}$$

$$K_s(j) = \hat{P}_s^{-}(j)C^{\mathrm{T}}\left[C\hat{P}_s^{-}(j)C^{\mathrm{T}} + R\right]^{-1} \tag{4.30}$$

$$\hat{P}_s(j) = \left[I - K_s(j)C\right]\hat{P}_s^{-}(j) \tag{4.31}$$

Update K_p*:*

$$\hat{P}_p^{-}(j) = \hat{P}_p(j-1) \tag{4.32}$$

$$K_p(j) = \hat{P}_p^{-}(j)H^{\mathrm{T}}\left[H\hat{P}_p^{-}(j)H^{\mathrm{T}} + R\right]^{-1} \tag{4.33}$$

$$\hat{P}_p(j) = \left[I - K_p(j)H\right]\hat{P}_p^{-}(j) \tag{4.34}$$

Here, the predicted error covariance matrices at time j for state and parameter vectors are denoted by $\hat{P}_s^{-}(j)$ and $\hat{P}_p^{-}(j)$, respectively. The specified constant covariance matrices for process noise and measurement noise are represented by Q and R. The two gain matrices (K_s and K_p) are updated by using the predicted error covariance matrices

($\hat{P}_s^-(j)$ and $\hat{P}_p^-(j)$). These error covariance matrices are then corrected by using the gain matrices. Φ and H are two Jacobian matrices defined as follows:

$$\Phi = \left.\frac{\partial F}{\partial \mathbf{x}}\right|_{\hat{\mathbf{x}}(j-1)}, \quad H = C\left.\frac{\partial F}{\partial \mathbf{p}}\right|_{\hat{\mathbf{p}}(j-1)} \tag{4.35}$$

The DEKF-based state and parameter estimation scheme described above is developed following the basic theory of the Kalman filtering method. However, the implementation of the developed estimation scheme to the robotic radiation-based processes is different from other applications due to the distributed characteristics of these processes, and this issue is discussed in the following subsection.

4.2.2 Discussion on the Implementation of the DEKF Estimation Scheme

Two challenges should be addressed when implementing the developed DEKF estimation scheme to robotic radiation-based processes. First, since most of these processes involve spatially large objects that should be modeled as distributed-parameter systems, the dimension of the state vectors in the DEKF increases with the size of the target. This in turn increases the computational burden for real-time implementation. Second, the spatial movement of the radiant actuator has significant influences on the observability of the system and thereby the performance of the estimator. The following discusses the two issues in detail.

- Reduction of the DEKF

Since the moving radiative actuator is smaller than the processed target in these robotic radiation-based processes, it can only influence the local process state near the current position. This makes it possible to reduce a large central DEKF into a group of

distributed DEKFs with smaller or manageable dimensions. Each DEKF only deals with the local state and parameter estimation within its own region. On the other hand, these local DEKFs can operate sequentially corresponding to the movement of the actuator instead of staying active throughout the whole process. This is because only the area within the actuator's current processing range is affected the most and should be considered for state and parameter estimation. Other areas of the target strip are affected less since they are far away from the actuator. Therefore, the local DEKFs for these areas can be frozen to reduce the computational cost. The operation mechanism of these local DEKFs is illustrated in Figure 4.3.

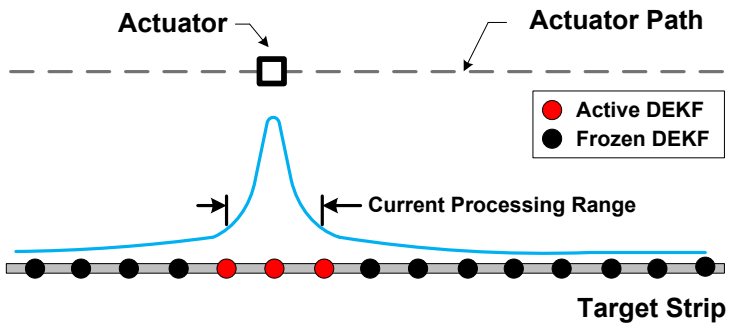

Figure 4.3 The operation mechanism of distributed local DEKFs

- Observability Analysis

The low-order subsystems corresponding to these distributed local DEKFs depicted in Figure 4.3 can be described by:

$$\mathbf{x}_i(j) = F_i\left[\mathbf{x}_i(j-1), \mathbf{u}(j-1), \mathbf{p}\right] \tag{4.36}$$

$$\mathbf{y}_i(j) = C_i\mathbf{x}_i(j), \quad i = 1, 2, \cdots \tag{4.37}$$

$$\mathbf{x}_i(j) = \left\{ \boldsymbol{\omega}_p(j), \boldsymbol{\omega}_{p+1}(j), \cdots \quad \cdots \right.$$
$$\left. p = 1 + (i-1)\frac{N}{G}, \;\; q = p + \frac{N}{G} - 1 \right. \tag{4.38}$$

Here, the number of the distributed local DEKFs and the number of the discretized units describing the target strip are denoted by G and N, respectively. Then the original state vector ($\mathbf{x}(j)$) can be divided into G segments and each segment is represented by $\mathbf{x}_i(j)$. The nonlinear governing equation for each state segment is denoted by $F_i(\cdot)$. The corresponding measurement equation is described in equation (4.37), in which the local process output $\mathbf{y}_i(j)$ is a linear combination of the corresponding state segment $\mathbf{x}_i(j)$ through C_i.

The observability for each subsystem can be approximately evaluated by analyzing the following observability matrix:

$$O_i = \begin{bmatrix} C_i \\ C_i\Phi_i \\ \vdots \\ C_i\left(\Phi_i\right)^{N/G-1} \end{bmatrix} \quad \Phi_i = \left.\frac{\partial F_i}{\partial \mathbf{x}_i}\right|_{\mathbf{x}_i(j-1)} \tag{4.39}$$

If the rank of the observability matrix defined in equation (4.39) is equal to the order of the subsystem (N/G), then the subsystem is fully observable. However, since the Jacobian matrix Φ_i is calculated from the previous state $\mathbf{x}_i(j-1)$ and input $\mathbf{u}(j-1)$, the observability for each subsystem will change with time due to the local state change caused by the movement of the actuator. Therefore, the activating policy for these distributed local DEKFs should be carefully designed to ensure that each of them

operates under good observability. The detailed observability analysis is provided with a demonstrative example in the next section.

4.3 Demonstrative Example on Robotic UV Curing

In this section, a detailed discussion is presented to illustrate the implementation of the developed DEKF estimation scheme to the robotic UV curing process described in Subsection 4.1.1. In this example, the original process model has been reduced to a series of low-order subsystems, and the distributed DEKF strategy is used for state and parameter estimation based on available measurements of the process output [107, 108].

4.3.1 Reduction of the UV Curing Model

Assuming that the photo-initiated curing (monomer consumption) is rapid and occurs before any significant diffusion of monomer takes place, the evolution of monomer concentration can be assumed to be independent for each point on the target strip. In addition, considering a substrate and film with much lower thermal conductivity compared to the exothermic polymerization, it is possible to ignore the diffusion term in the thermal dynamics equation. Further, the temperature change caused by the directly absorbed UV irradiation is negligible compared to the heat generation from the polymerization. Given these assumptions and considerations, the original curing model described in Subsection 4.1.1 can be further reduced and represented in the following discrete form [108]:

$$I(z,j) = k(z)\frac{\varphi(j)d_0^2}{\pi\left\{\left[\sum_{n=1}^{j} v_a(n)\Delta t - z\Delta x\right]^2 + d_0^2\right\}^2}, \quad z = 1,2,\cdots \tag{4.40}$$

$$[M](z,j)=\left(-\kappa\left\{\phi\varepsilon[PI]_0\right\}^{0.5}\left[I(z,j-1)\,e^{-\phi\varepsilon\sum_{m=1}^{j-1}I(z,m)\Delta t}\right]^{0.5}\Delta t+1\right)[M](z,j-1) \tag{4.41}$$

$$T(z,j)=-\frac{\Delta H}{\rho c}\left\{[M](z,j)-[M](z,j-1)\right\}+\left[-\frac{h}{\rho c}\Delta t+1\right]T(z,j-1)+\frac{h}{\rho c}\Delta t T_{\infty} \tag{4.42}$$

Here, the indexes j and z denote the j^{th} time step and the z^{th} spatial unit from the left-end of the target strip. The number of these units is represented by N. The temporal and spatial steps are denoted by Δt and Δx, respectively. Grouping some of the coefficients and variables, we obtain:

$$I(z,j)=k(z)\varphi(j)\Upsilon(v_a,z,j) \tag{4.43}$$

$$[M](z,j)=\left(\eta_1\left[I(z,j-1)\,e^{\eta_2\sum_{m=1}^{j}I(z,m)\Delta t}\right]^{0.5}+1\right)[M](z,j-1) \tag{4.44}$$

$$T(z,j)=\eta_3\eta_1\left[I(z,j-1)\,e^{\eta_2\sum_{m=1}^{j}I(z,m)\Delta t}\right]^{0.5}[M](z,j-1)+\left(\eta_4+1\right)T(z,j-1)-\eta_4 T_{\infty} \tag{4.45}$$

$$\Upsilon(v_a,z,j)=\frac{d_0^2}{\pi\left\{\left[\sum_{n=1}^{j}v_a(n)\Delta t-z\Delta x\right]^2+d_0^2\right\}^2} \tag{4.46}$$

$$\eta_1=-\kappa\left\{\phi\varepsilon[PI]_0\right\}^{0.5}\Delta t,\quad \eta_2=-\phi\varepsilon,\quad \eta_3=-\frac{\Delta H}{\rho c},\quad \eta_4=-\frac{h}{\rho c}\Delta t \tag{4.47}$$

If the composite input term $\left[I(z, j-1)\, e^{\eta_2 \sum_{m=1}^{j-1} I(z,m)\Delta t} \right]^{0.5}$ is replaced by a simplified one $u\left[z, j-1, \varphi(j-1), v_a(j-1), k(z)\right]$, then equations (4.44) and (4.45) can be expressed as:

$$[M](z, j) = f_1 = \left\{\eta_1 u\left[z, j-1, \varphi(j-1), v_a(j-1), k(z)\right] + 1\right\}[M](z, j-1) \tag{4.48}$$

$$\begin{aligned} T(z, j) &= f_2 \\ &= \eta_3 \eta_1 u\left[z, j-1, \varphi(j-1), v_a(j-1), k(z)\right][M](z, j-1) + \left(\eta_4 + 1\right) T(z, j-1) - \eta_4 T_\infty \end{aligned} \tag{4.49}$$

Given the simplified curing process model described in the above equations, the objective of this estimation problem can be outlined as follows. 1) To estimate the monomer concentration distribution along the target strip by using the process model and the temperature measurements; 2) To estimate some of the unknown or uncertain parameters of the process model in parallel to improve the accuracy of the state estimation. In this example, the distributed values of the UV absorption coefficient and the convective heat transfer coefficient are selected for demonstrating the parameter estimation.

4.3.2 Design of the Distributed Local DEKFs

As pointed out in Subsection 4.1.2, a number of distributed local DEKFs will be used for state and parameter estimation instead of using a central large-dimensional one. In addition, only those around the current position of the actuator are activated during the curing process to reduce the computational cost.

To implement the distributed estimation structure and the activating policy, the following vectors and matrices are used to store the key variables and parameters of these distributed DEKFs.

$$\hat{\mathbf{X}}(j)=\begin{Bmatrix}[\hat{M}](g_1,j)\\ \hat{T}(g_1,j)\\ [\hat{M}](g_2,j)\\ \hat{T}(g_2,j)\\ \vdots\\ [\hat{M}](g_G,j)\\ \hat{T}(g_G,j)\end{Bmatrix},\ \hat{\mathbf{P}}(j)=\begin{Bmatrix}\hat{k}(g_1,j)\\ \hat{\eta}_4(g_1,j)\\ \hat{k}(g_2,j)\\ \hat{\eta}_4(g_2,j)\\ \vdots\\ \hat{k}(g_G,j)\\ \hat{\eta}_4(g_G,j)\end{Bmatrix},\ \hat{\mathbf{U}}(j)=\begin{Bmatrix}\hat{u}_{g_1}(j)\\ \hat{u}_{g_2}(j)\\ \vdots\\ \hat{u}_{g_i}(j)\\ \vdots\\ \hat{u}_{g_G}(j)\end{Bmatrix},\ \mathbf{Y}(j)=\begin{Bmatrix}T_m(g_1,j)\\ T_m(g_2,j)\\ \vdots\\ T_m(g_i,j)\\ \vdots\\ T_m(g_G,j)\end{Bmatrix} \tag{4.50}$$

$$\hat{u}_{g_i}(j)=u\left[g_i,j,\varphi(j),v_a(j),\hat{k}(g_i,j)\right] \tag{4.51}$$

$$\mathbf{F}\left[\hat{\mathbf{X}}(j-1),\hat{\mathbf{U}}(j-1),\hat{\mathbf{P}}(j-1)\right]=\begin{Bmatrix}f_{1,g_1}\\ f_{2,g_1}\\ \vdots\\ f_{1,g_i}\\ f_{2,g_i}\\ \vdots\\ f_{1,g_G}\\ f_{2,g_G}\end{Bmatrix},\ \mathbf{C}=\begin{bmatrix}0 & 1 & & & & \\ & & 0 & 1 & & \\ & & & & \ddots & \\ & & & & 0 & 1\end{bmatrix}_{G\times 2G} \tag{4.52}$$

$$\begin{aligned}f_{1,g_i}&=\left[\eta_1\hat{u}_{g_i}(j-1)+1\right][\hat{M}](g_i,j-1)\\ f_{2,g_i}&=\eta_3\eta_1\hat{u}_{g_i}(j-1)[\hat{M}](g_i,j-1)+\left[\hat{\eta}_4(j-1)+1\right]\hat{T}(g_i,j-1)-\hat{\eta}_4(j-1)T_\infty\end{aligned} \tag{4.53}$$

$$\mathbf{\Phi}(j)=\mathbf{diag}\left\{\left.\frac{\partial\mathbf{F}}{\partial\mathbf{X}}\right|_{g_1,j-1},\cdots\left.\frac{\partial\mathbf{F}}{\partial\mathbf{X}}\right|_{g_i,j-1}\cdots\left.\frac{\partial\mathbf{F}}{\partial\mathbf{X}}\right|_{g_G,j-1}\right\} \tag{4.54}$$

$$\left.\frac{\partial \mathbf{F}}{\partial \mathbf{X}}\right|_{g_i,j-1} = \begin{bmatrix} \left.\dfrac{\partial f_{1,g_i}}{\partial [M]}\right|_{j-1} & \left.\dfrac{\partial f_{1,g_i}}{\partial T}\right|_{j-1} \\ \left.\dfrac{\partial f_{2,g_i}}{\partial [M]}\right|_{j-1} & \left.\dfrac{\partial f_{2,g_i}}{\partial T}\right|_{j-1} \end{bmatrix} = \begin{bmatrix} \eta_1 \hat{u}_{g_i}(j-1)+1 & 0 \\ \eta_3 \eta_1 \hat{u}_{g_i}(j-1) & \hat{\eta}_4(j-1)+1 \end{bmatrix} \tag{4.55}$$

$$g_i = \frac{N}{G} i, \quad i = 1, 2, \cdots \tag{4.56}$$

Here, the vectors for saving the predicted states, parameters, the composite inputs, and the measured outputs are denoted by $\hat{\mathbf{X}}(j)$, $\hat{\mathbf{P}}(j)$, $\hat{\mathbf{U}}(j)$, and $\mathbf{Y}(j)$ respectively. The index g_i represents the spatial position of the i^{th} local DEKF on the target strip. The number of the distributed local DEKFs and the number of the discretized units that constitutes the target strip are denoted by G and N (setting $N = 2G$ in this example). The nonlinear state transition vector and the measurement matrix are defined by $\mathbf{F}$ and $\mathbf{C}$, respectively. The Jacobian matrix $\mathbf{\Phi}$ is calculated based on the first-order Taylor Series approximation. Additional vectors and matrices are defined below for saving the error covariance, the Kalman gains, and other information for these distributed local DEKFs.

$$\begin{aligned} \mathbf{P}_s(j) &= \mathbf{diag}\left\{ P_{s,g_1}(j), \cdots \quad \cdots \right. \\ \mathbf{P}_p(j) &= \mathbf{diag}\left\{ P_{p,g_1}(j), \cdots \quad \cdots \right. \end{aligned} \tag{4.57}$$

$$P_{s,g_i}(j) = \begin{bmatrix} e_{s,[M]}(g_i, j) & 0 \\ 0 & e_{s,T}(g_i, j) \end{bmatrix}, \quad P_{p,g_i}(j) = \begin{bmatrix} e_{p,k}(g_i, j) & 0 \\ 0 & e_{p,\eta_4}(g_i, j) \end{bmatrix} \tag{4.58}$$

$$\mathbf{K}_s(j)=\begin{Bmatrix} K_{s,[M]}(g_1,j) \\ K_{s,T}(g_1,j) \\ K_{s,[M]}(g_2,j) \\ K_{s,T}(g_2,j) \\ \vdots \\ K_{s,[M]}(g_G,j) \\ K_{s,T}(g_G,j) \end{Bmatrix},\quad \mathbf{K}_p(j)=\begin{Bmatrix} K_{p,k}(g_1,j) \\ K_{p,\eta_4}(g_1,j) \\ K_{p,k}(g_2,j) \\ K_{p,\eta_4}(g_2,j) \\ \vdots \\ K_{p,k}(g_G,j) \\ K_{p,\eta_4}(g_G,j) \end{Bmatrix} \tag{4.59}$$

$$\mathbf{H}(j)=\begin{bmatrix} \left.\frac{\partial f_{2,g_1}}{\partial k}\right|_{j-1} & \left.\frac{\partial f_{2,g_1}}{\partial \eta_4}\right|_{j-1} & & & & \\ & & \ddots & & & \\ & & & \left.\frac{\partial f_{2,g_i}}{\partial k}\right|_{j-1} & \left.\frac{\partial f_{2,g_i}}{\partial \eta_4}\right|_{j-1} & \\ & & & & \ddots & \\ & & & & \left.\frac{\partial f_{2,g_G}}{\partial k}\right|_{j-1} & \left.\frac{\partial f_{2,g_G}}{\partial \eta_4}\right|_{j-1} \end{bmatrix} \tag{4.60}$$

$$\left.\frac{\partial f_{2,g_i}}{\partial k}\right|_{j-1}=\eta_3\eta_1[\hat{M}](g_i,j-1)\left.\frac{\partial u_{g_i}}{\partial k}\right|_{j-1},\quad \left.\frac{\partial f_{2,g_i}}{\partial \eta_4}\right|_{j-1}=\hat{T}(g_i,j-1)-T_\infty \tag{4.61}$$

$$\begin{aligned}\left.\frac{\partial u_{g_i}}{\partial k}\right|_{j-1}=e^{\frac{1}{2}\eta_2\hat{k}(g_i,j-1)\sum_{m=1}^{j-1}\varphi(m)\Upsilon(v_a,g_i,m)\Delta t}&\left\{\frac{1}{2}\hat{k}(g_i,j-1)^{-0.5}\left[\varphi(j-1)\Upsilon(v_a,g_i,j-1)\right]^{0.5}\right.\\ &\left.+\left[\hat{k}(g_i,j-1)\varphi(j-1)\Upsilon(v_a,g_i,j-1)\right]^{0.5}\left[\frac{1}{2}\eta_2\sum_{m=1}^{j-1}\varphi(m)\Upsilon(v_a,g_i,m)\Delta t\right]\right\}\end{aligned} \tag{4.62}$$

$$\Upsilon(v_a,g_i,m)=\frac{d_0^2}{\pi\left\{\left[\sum_{n=1}^{m}v_a(n)\Delta t-g_i\Delta x\right]^2+d_0^2\right\}^2},\quad m=1,2,\cdots \tag{4.63}$$

Here, the two error covariance matrices (denoted by $\mathbf{P}_s(j)$ and $\mathbf{P}_p(j)$) are used to save the time-varying state and parameter error covariances for these distributed local

DEKFs. The time-varying Kalman gains for these DEKFs are stored in two gain matrices ($\mathbf{K}_s(j)$ and $\mathbf{K}_p(j)$). The calculation of the Jacobian matrix for measurement ($\mathbf{H}(j)$) is outlined by equations (4.61) ~ (4.63). It should be noted that the derivative of function f_2 with respect to the absorption coefficient k is given by a highly nonlinear expression.

Process and measurement noise terms are added to the UV curing process model in a linear manner. Two constant matrices are defined below to represent the covariance of the process and measurement noise for these distributed local DEKFs. The two terms (Q_{g_i} and R_{g_i}) defined in equation (4.65) denote the significant tunable factors that can influence the estimation performance of each DEKF.

$$\mathbf{Q} = \begin{bmatrix} Q_{g_1} & & & \\ & \ddots & & \\ & & Q_{g_i} & \\ & & & \ddots \\ & & & & Q_{g_G} \end{bmatrix}, \quad \mathbf{R} = \begin{bmatrix} R_{g_1} & & & \\ & \ddots & & \\ & & R_{g_i} & \\ & & & \ddots \\ & & & & R_{g_G} \end{bmatrix} \tag{4.64}$$

$$Q_{g_i} = \begin{bmatrix} \sigma^2_{g_i,[M]} & \\ & \sigma^2_{g_i,T} \end{bmatrix}, \quad R_{g_i} = \tau^2_{g_i} \tag{4.65}$$

In summary, the above formulations (denoted by equations (4.50) ~ (4.65)) represent the design of these distributed local DEKFs in an integral matrix form. Now the activation policy can be easily designed by implementing the general DEKF estimation scheme (described in equations (4.25) ~ (4.35)) to selected subsystems of this integral matrix form. Given the mechanism illustrated in Figure 4.3, only the DEKFs around the

moving actuator will be activated to perform the state and parameter estimation. The mathematical description of the state and parameter estimation with the activating policy is presented as follows.

sub: denoting the i_L th ~ i_R th elements (rows and columns) of each vector (matrix) (4.66)

i_L, i_R: determined by the activating policy (4.67)

Parameter Prediction:
$$\hat{\mathbf{P}}^{-}_{sub}(j) = \hat{\mathbf{P}}_{sub}(j-1) \tag{4.68}$$

State Prediction:
$$\hat{\mathbf{X}}^{-}_{sub}(j) = \mathbf{F}_{sub}\left[\hat{\mathbf{X}}_{sub}(j-1), \hat{\mathbf{U}}_{sub}(j-1), \hat{\mathbf{P}}_{sub}(j-1)\right] \tag{4.69}$$

State Correction:
$$\hat{\mathbf{X}}_{sub}(j) = \hat{\mathbf{X}}^{-}_{sub}(j) + \mathbf{K}_{s,sub}(j)\left[\mathbf{Y}_{sub}(j) - \mathbf{C}_{sub}\hat{\mathbf{X}}^{-}_{sub}(j)\right] \tag{4.70}$$

Parameter Correction:
$$\hat{\mathbf{P}}_{sub}(j) = \hat{\mathbf{P}}^{-}_{sub}(j) + \mathbf{K}_{p,sub}(j)\left[\mathbf{Y}_{sub}(j) - \mathbf{C}_{sub}\hat{\mathbf{X}}^{-}_{sub}(j)\right] \tag{4.71}$$

The subscript "*sub*" denotes the i_L th ~ i_R th elements (rows and columns) of each vector (matrix) shown in equations (4.68) ~ (4.71). The two boundary indexes (i_L and i_R) are determined by the current position of the moving actuator and the width of a spatial window that contains the activated DEKFs. The simulation results of the above distributed DEKF formulation are discussed in the next subsection.

4.3.3 Results and Discussion

The simulation of the UV curing process is performed by using the full model described in equations (4.5), (4.10), and (4.11). The reduced process model characterized by equations (4.40) ~ (4.42) is used in the design of the distributed DEKF estimation scheme. The spatially distributions of the two parameters to be estimated in this example are defined as follows: 1) The UV absorption coefficient decreases from the left-end to

the right-end of the target strip; 2) Two different convective heat transfer coefficients are applied to the left and right parts of the target strip, respectively. In these examples, the UV source will move through the target strip with constant speed and radiant power. Most of the chemical, thermal and material parameters used in this simulation are obtained from the references [101, 102]. The configurations of this simulation scenario are summarized in Table 4.1.

Table 4.1 Simulation configurations

Description	**Notation**	**Value and unit**
Length of the target strip	L	1.4 m
Paint film thickness	d_p	0.0001 m
Time step of the simulation	Δt	0.01 s
Length of a discretized unit	Δx	0.01m
Number of discretized units	N	140
Moving range of the UV source	-	[0.2 1.2] m
Speed of the UV source	v_a	0.1 m/s
Radiant power of the UV source	φ	10.2 W
Normal distance	d_0	0.03 m
Distributed UV absorption coefficient	$k(x)$	$k(x) = -2x/7 + 0.8,\ x \in [0,\ 1.4\ \text{m}]$
Distributed effective convective heat transfer coefficient	$h_e(x)$	$h_e(x) = \begin{cases} 23.1/d_p, x \in [0,\ 0.7\ \text{m}] \\ 28.9/d_p, x \in (0.7,\ 1.4\ \text{m}] \end{cases}$ W/(m^3 °C)
Initial values of estimated absorption coefficient	$\hat{k}(x)_0$	$\hat{k}(x)_0 = 0.6,\ x \in [0,\ 1.4\ \text{m}]$
Initial values of estimated convective coefficient	$\hat{h}_e(x)_0$	$\hat{h}_e(x)_0 = 26/d_p,\ x \in [0,\ 1.4\ \text{m}]$
System noise for each unit	$\mathbf{n}_s$	$E[\mathbf{n}_s] = \begin{bmatrix} 0 & \\ & 0 \end{bmatrix}, \sigma[\mathbf{n}_s] = \begin{bmatrix} 0.1\mathbf{mol/L} & \\ & 0.01^\circ \end{bmatrix}$
Measurement noise for each unit	$\mathbf{n}_m$	$E[\mathbf{n}_m] = 0,\ \sigma[\mathbf{n}_m] = 0.001^\circ$

The effective convective heat transfer coefficient $h_e(x)$ is defined as follows. Considering the fundamental thermal dynamics:

$$dV\rho c\frac{\partial T(x,t)}{\partial t}=dV\frac{\partial}{\partial x}\left[\lambda\frac{\partial T(x,t)}{\partial x}\right]+dA\,h\left[T(x,t)-T_{\infty}\right] \tag{4.72}$$

It can be re-written as:

$$\begin{aligned}\rho c\frac{\partial T(x,t)}{\partial t}&=\frac{\partial}{\partial x}\left[\lambda\frac{\partial T(x,t)}{\partial x}\right]+\frac{h}{dV/dA}\left[T(x,t)-T_{\infty}\right]\\&=\frac{\partial}{\partial x}\left[\lambda\frac{\partial T(x,t)}{\partial x}\right]+\frac{h}{d_p}\left[T(x,t)-T_{\infty}\right]\end{aligned} \tag{4.73}$$

The term dV/dA is equal to the thickness (denoted by d_p) of the paint film on the target strip. Then, the new coefficient h/d_p is defined as the effective convective heat transfer coefficient and is represented by h_e in Table 4.1.

The major parameters of the UV curing process model are listed in Table 4.2.

Table 4.2 Parameters of the UV curing process model

Description	**Notation**	**Value and unit**
Initial distribution of the photo-initiator concentration	$[PI]_0(x)$	$[PI]_0(x)=0.16$ mol/L, $x\in[0,\ 1.4\text{ m}]$
Initial distribution of the monomer concentration	$[M]_0(x)$	$[M]_0(x)=2.5$ mol/L, $x\in[0,\ 1.4\text{ m}]$
Quantum yield for initiation	ϕ	2.18×10^{-4} mol/Einstein
Molar absorptivity	ε	188.2 L/(mol cm)
Composite reaction factor	$\kappa=k_p/k_t^{0.5}$	4.22 [L/(mol s)]$^{0.5}$
Polymerization enthalpy	ΔH	39.71 kJ/mol
Density	ρ	1.14 g/cm^3
Specific heat capacity	c	1.98 kJ/(kg °C)
Thermal conductivity	λ	0.19 W/(m °C)
Ambient temperature	T_{∞}	25 °C

The design parameters for the distributed DEKF estimation scheme are presented in Table 4.3.

Table 4.3 Design parameters of the distributed DEKF estimation scheme

Description	**Notation**	**Value and unit**
Number of all distributed DEKFs	G	70
Number of DEKFs in the activating window	G_a	25
System covariance matrix for each DEKF	Q_{g_i}	$Q=\begin{bmatrix} 0.01(\mathbf{mol/L})^2 & \\ & 1\times10^{-4}(\circ\smile) \end{bmatrix}$
Initial measurement covariance matrix for each DEKF	$R_{g_i,0}$	$R_0=9.5\times10^{-8}(\circ\smile)$
Adjusted measurement covariance matrices for DEKFs in the activating window	R'_{g_i}	$R'_{g_i}=[4+0.4(i-i_L)]\times10^{-8}(\circ\smile),\ i=i_L\sim i_M-1$ $R'_{g_i}=[8+6(i-i_M)]\times10^{-8}(\circ\smile),\ i=i_M\sim i_R$
Initial state error covariance matrix for each DEKF	$P_{s,g_i}(0)$	$P_{s,g_i}(0)=\begin{bmatrix} 0.01(\mathbf{mol/L})^2 & \\ & 1\times10^{-4}(\circ\smile) \end{bmatrix}$
Initial parameter error covariance matrix for each DEKF	$P_{p,g_i}(0)$	$P_{p,g_i}(0)=\begin{bmatrix} 1.1\times10^{-5} & \\ & 4\times10^{-6} \end{bmatrix}$
		(k and η_4 are dimensionless)

In Table 4.3, the indexes of the first, the middle, and the last DEKFs within the current activating window are denoted by i_L, i_M, and i_R, respectively. The index g_i represents the spatial position of the i^{th} DEKF on the target strip.

The simulation results are presented in Figure 4.4 ~ Figure 4.6.

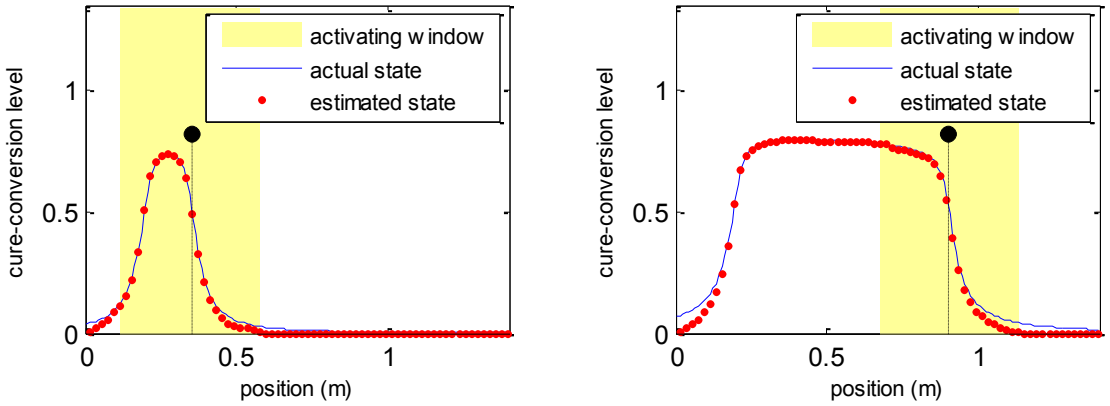

Figure 4.4 Cure-conversion level distributions when the actuator crosses different positions on the target strip: (a) x_a=0.35m, (b) x_a=0.9m

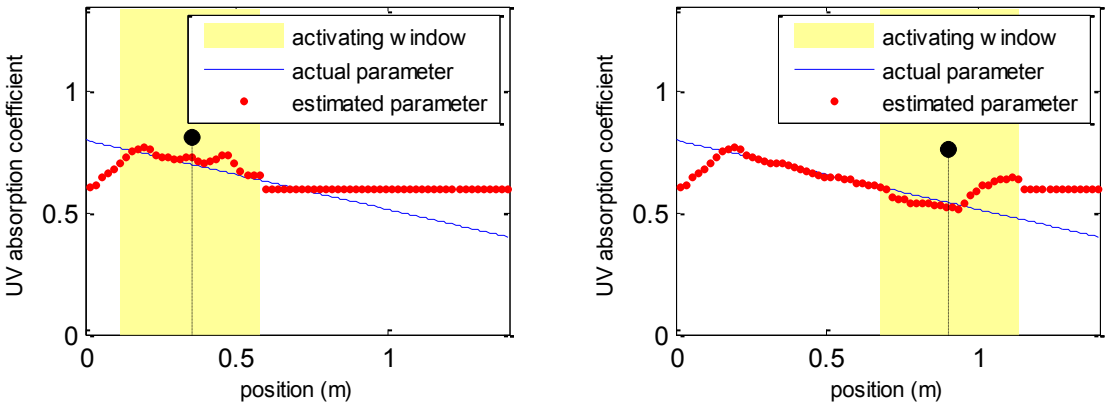

Figure 4.5 UV absorption coefficient distributions when the actuator crosses different positions on the target strip: (a) x_a=0.35m, (b) x_a=0.9m

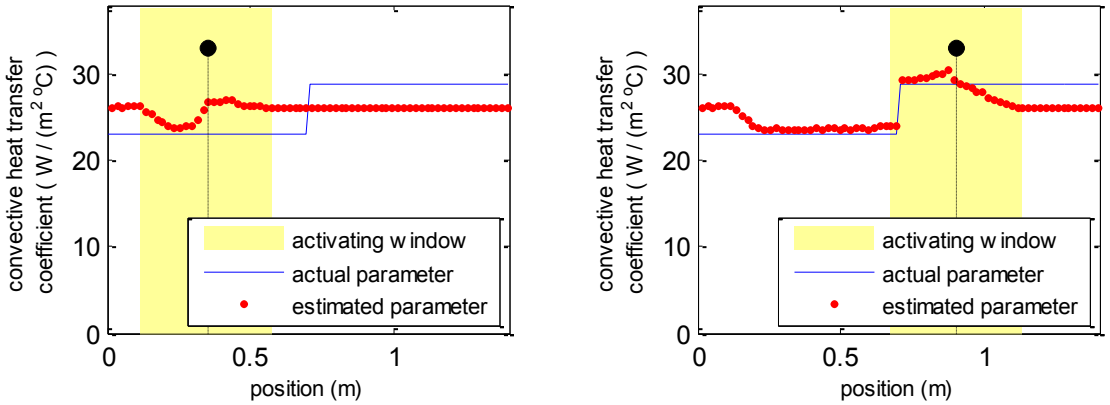

Figure 4.6 Convective heat transfer coefficient distributions when the actuator crosses different positions on the target strip: (a) x_a=0.35m, (b) x_a=0.9m

The solid ball shown in Figure 4.4 ~ Figure 4.6 denotes the UV actuator that moves along the target strip. The state estimation results are presented in Figure 4.4, where the estimated cure-conversion distributions are compared with the actual values. The cure-conversion level, denoted by $\alpha(x,t)$, is calculated from the initial and current monomer concentrations ($[M]_0(x)$ and $[M](x,t)$) as follows:

$$\alpha(x,t) = \frac{[M]_0(x) - [M](x,t)}{[M]_0(x)} \tag{4.74}$$

In the simulations, the initial monomer concentration (included in Table 4.2) is set as constant for all discretized units on the target strip. The comparison is performed when the actuator crosses different positions (x_a=0.35, 0.9m) on the target strip. The shaded area represents the activating window containing the currently activated DEKFs. The results in Figure 4.4 show that the estimated state (cure-conversion level) distribution has a good match to the time-varying spatial distribution of the actual process state.

The estimation results for the UV absorption coefficient distribution are shown in Figure 4.5. Figure 4.5(a) gives the comparison of the estimated and actual distributions of the absorption coefficient when the actuator crosses the position (x_a =0.35) near the starting point. It shows that the activated DEKFs within the activating window are performing the estimation of the absorption coefficient for the covered locations, while the remaining DEKFs stay inactive and the corresponding absorption coefficients of these locations keep the initial values. It can be observed from Figure 4.5(b) that the estimated distribution of the absorption coefficient matches the actual distribution well when the actuator is close to the end point.

Figure 4.6 illustrates the estimation results for the convective heat transfer coefficient distribution. Similar comparisons of the estimated and actual distributions of the convective heat transfer coefficient are given in Figure 4.6(a) and (b), respectively. It can be observed that estimated distribution of the convective heat transfer coefficient for the locations which the actuator has passed shows a good match to the actual distribution. For those locations which haven't yet been illuminated by the actuator, the associated DEKFs will start the estimation once they enter the activating window with the approach of the actuator.

In addition to these spatial distributions shown in Figure 4.4 ~ Figure 4.6, time history plots of the states and parameters for selected positions on the target strip are also provided in Figure 4.7 ~ Figure 4.9 for further analysis.

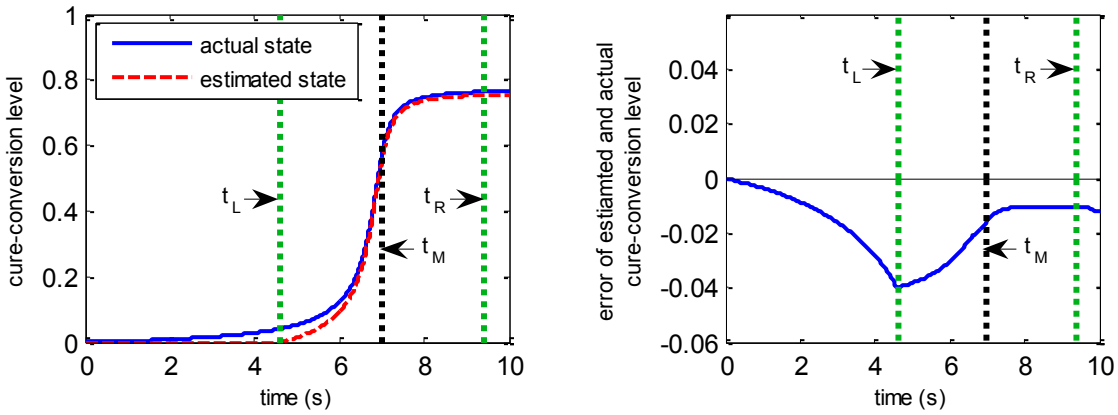

(a) **(b)**

Figure 4.7 (a) Time history of the cure-conversion level at x=0.9m (b) Time history of the error of the actual and estimated cure-conversion level at x=0.9m

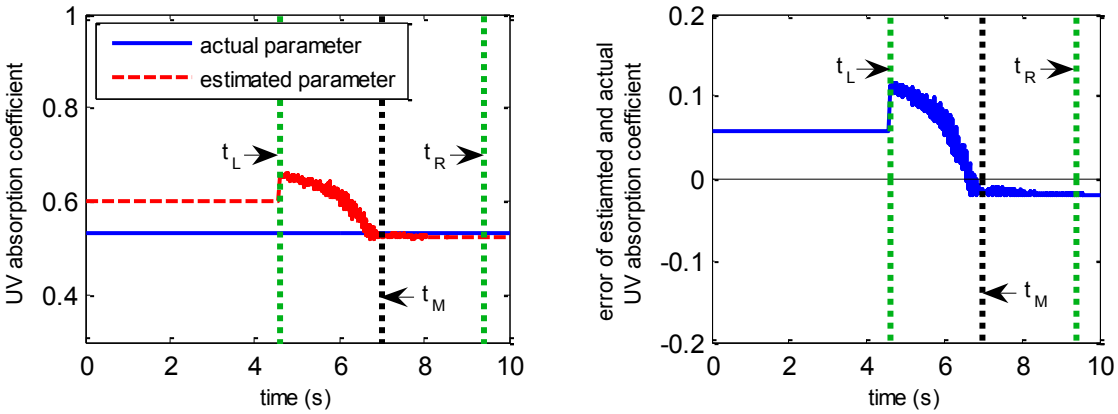

(a) **(b)**

Figure 4.8 (a) Time history of the UV absorption coefficient at x=0.9m (b) Time history of the error of the actual and estimated absorption coefficient at x=0.9m

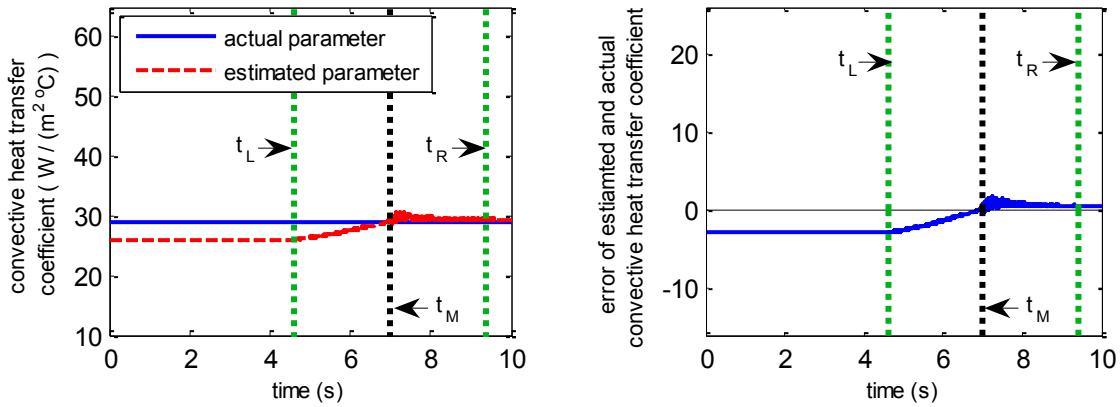

Figure 4.9 (a) Time history of the convective heat transfer coefficient at x=0.9m (b) Time history of the error of the actual and estimated heat transfer coefficient at x=0.9m

Three time indexes, denoted by t_L, t_M, and t_R in Figure 4.7 ~ Figure 4.9, are used to represent the time when the DEKF (at x=0.9m) is activated, when the actuator is exactly crossing this position (x=0.9m), and when the DEKF (at x=0.9m) is frozen again, respectively. Figure 4.7(a) shows the time history of the estimated and actual cure-conversion level at the selected position (x=0.9m). The associated error dynamics is illustrated in Figure 4.7(b). It can be observed that the error of estimated and actual cure-conversion level begins to converge once the local DEKF (at x=0.9m) is activated ($t > t_L$). Then the error is further pulled closed to zero after the actuator crosses this position ($t > t_M$) and the estimated cure-conversion level also has a good match to the actual value.

Figure 4.8 shows the time history of the estimated and actual UV absorption coefficient at the selected position (x=0.9m). In Figure 4.8(a), the estimated UV absorption coefficient first keeps its initial value before the associated DEKF is activated ($t < t_L$). Once it has been activated ($t > t_L$), the estimation starts but the result shows little

match to the actual value due to the fact that the actuator is still not close enough to provide necessary observability. This can be explained by checking the corresponding observability matrix presented below for this parameter.

$$\left.\frac{\partial f_{2,g_i}}{\partial k}\right|_{j-1} = \eta_3\eta_1[\hat{M}](g_i, j-1)\left.\frac{\partial u_{g_i}}{\partial k}\right|_{j-1} \tag{4.75}$$

When the actuator is far away, the term $\frac{\partial u_{g_i}}{\partial k}$ is close to zero due to the low UV irradiation given the complete expression described in equations (4.62) and (4.63). Then, the observability matrix shown in equation (4.75) is also close to zero, which means the current observability of the subsystem is not good enough to support the estimation of the UV absorption coefficient.

The estimation performance is improved when the actuator crosses the current position (x=9m, $t > t_M$) since the actuator's approach improves the observability, and thus the error of the estimated and actual values depicted in Figure 4.8(b) converges to zero very quickly.

Similar observations can be found in Figure 4.9 which depicts the time history of the estimated and actual convective heat transfer coefficients at the selected position (x=0.9m). The beginning stage of the estimation shows poor performance because the actuator is still far away although the DEKF associated with this position (x=0.9m) has already been activated. This can also be explained by using the following observability matrix corresponding to the convective heat transfer coefficient.

$$\left.\frac{\partial f_{2,g_i}}{\partial \eta_4}\right|_{j-1} = \hat{T}(g_i, j-1) - T_\infty \tag{4.76}$$

When the actuator is far away from the selected position, the temperature at this position is almost the same as the ambient temperature (T_∞) since there is litter polymerization taking place. Therefore, the observability matrix described in equation (4.76) is close to zero, which means the convective heat transfer coefficient cannot be estimated well under this condition. Once the actuator crosses the selected position (x=0.9m), the observability of the system is greatly improved due to the temperature increase caused by the heat generation from the polymerization. Therefore, the corresponding estimation performance is improved and the estimation error converges to zero quickly.

The above example of state and parameter estimation for the UV curing process demonstrates that the developed distributed DEKF estimation scheme can give an acceptable estimation of the cure-conversion level distribution by using the temperature measurements and the reduced curing process model with some parameters (UV absorption coefficient and convective heat transfer coefficient) adaptively updated for improved model accuracy and estimation performance.

Chapter Summary

This chapter presented a distributed state and parameter estimation scheme that can be used for monitoring and control of robotic radiation-based processes. This distributed estimation scheme was developed based on a generalized 1D scanning formulation and the dual extended Kalman filtering (DEKF) approach. In this scheme,

the state and parameter estimations are performed in parallel by a group of distributed local DEKFs with a designed activating policy corresponding to the spatial movement of the actuator. The change of system observability due to the moving actuator and the associated influences on the estimation performance were also discussed. The developed distributed state and parameter estimation scheme was then implemented to a robotic UV curing process through simulation. The results demonstrated that the developed scheme can provide a good estimation of the distributed process states in the presence of unknown process parameters and varying observability.

CHAPTER FIVE

COORDINATED CONTROL AND PROCESS OPTIMIZATION

Most robotic radiation-based processes involve the use of multiple manipulated variables. The two major variables, which have significant influences on the final quality of these processes, are the power and the speed of the moving radiant actuator. Process control by manipulating either of the two variables has been discussed in Chapter 3. To achieve improved process quality and energy efficiency, a framework for coordinating multiple manipulated variables and realizing process optimization is highly needed.

In this chapter, the coordinated control problem is addressed at three different levels by using the generalized 1D scanning formulation described in Chapter 4. First, open-loop coordination is used to determine the optimal nominal radiant power and speed of the actuator in consideration of the energy cost and process efficiency. Second, a basic coordinated feedback control strategy is developed, which uses some designed control rules and distributed process state information through online estimation as outlined in Chapter 4. In this rule-based coordination, the radiant power and the speed of the actuator are adjusted around nominal values obtained from the open-loop coordination. Third, a distributed model predictive control (MPC) strategy, which incorporates online process estimation, prediction and optimization, is developed to achieve optimal coordination of the radiant power and the speed of the moving actuator for improved process quality and energy efficiency.

5.1 Open-loop Coordination

The objective of the open-loop coordination is to find the optimal nominal radiant power and speed of the moving actuator that can be applied in an open-loop manner without updates during the process. Generally, the open-loop coordination can be described as the following static optimization problem:

$$\min \quad J(v_a, u_a) = q_1 u_a^2 + q_2 \frac{1}{v_a^2} \tag{5.1}$$

$$\text{subject to } f_q(v_a, u_a) = 0,\ v_{lb} \le v_a \le v_{ub},\ u_{lb} \le u_a \le u_{ub} \tag{5.2}$$

Here, the cost function $J(v_a, u_a)$ is composed of two terms: the square of the radiant power (related to energy cost), and the reciprocal of the speed (related to process efficiency or productivity). q_1 and q_2 are weighting coefficients for the two terms in the cost function. The equality constraint function f_q describes the relationship of the speed v_a and the radiant power u_a that can drive the process state to the desired level. In the two inequality constraints, the lower and upper boundaries of the speed are denoted by v_{lb} and v_{ub}, respectively. Similarly, u_{lb} and u_{ub} represent the corresponding boundaries for the radiant power. An example of this open-loop coordination for the robotic UV curing process will be presented later in Section 5.4.

5.2 Rule-Based Coordinated Control

Although the open-loop coordination provides the optimal combination of the radiant power and speed that can help achieve the desired process quality under ideal conditions, closed-loop control is still needed to compensate for various disturbances in

practical processes. In this section, a rule-based feedback control strategy is developed to coordinate the radiant power and the speed of the moving actuator based on process state feedback obtained from the distributed DEKF estimators and the optimization results from the open-loop coordination. The general structure of the rule-based coordinated control is illustrated in Figure 5.1.

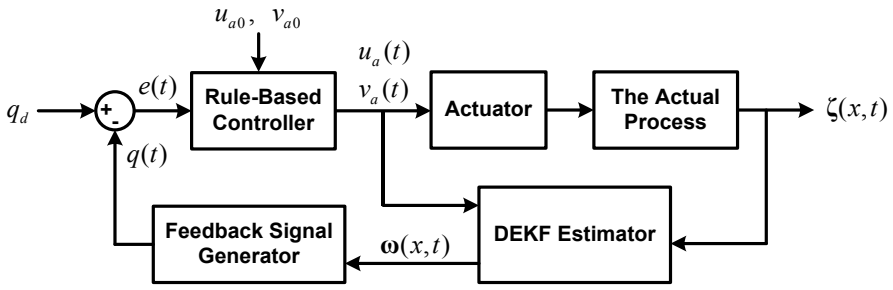

Figure 5.1 The general structure of the rule-based coordinated control

Here, the nominal radiant power and speed determined by the open-loop coordination are denoted by u_{a0} and v_{a0}, respectively. The measured process outputs and the estimated process states are represented by $\boldsymbol{\zeta}(x,t)$ and $\boldsymbol{\omega}(x,t)$, respectively. The actual process quality level $q(t)$ is generated from the estimated process states $\boldsymbol{\omega}(x,t)$, and compared with the desired process quality level (set-point) q_d. The error signal $e(t)$ is then sent to the rule-based controller, which determines the control inputs ($u_a(t)$ and $v_a(t)$) based on some designed rules. The following subsections detail the generation of the feedback signal and the design of the control rules.

5.2.1 Local Feedback Signal Generation

Recall that, in the distributed estimation scheme, only those DEKFs around the current position of the moving actuator need to be activated for state/parameter

estimation. Likewise, the generation of the feedback signal for the closed-loop control also needs to be performed locally, associated with the spatial movement of the actuator. Here, the local feedback signal is generated from the estimated process states within some defined sampling windows illustrated in Figure 5.2.

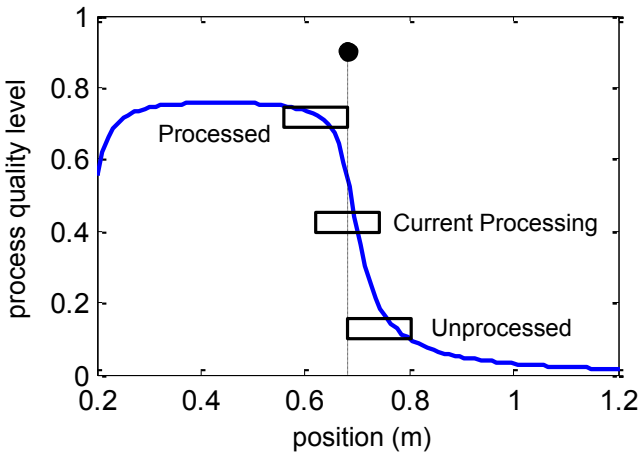

Figure 5.2 Sampling windows used for local feedback signal generation

The solid ball in Figure 5.2 represents the moving actuator. Three sampling windows, namely "Processed", "Current Processing", and "Unprocessed", are defined to obtain process information from the different positions on the target strip. The final feedback signal is then generated by calculating the average process information within the three sampling windows in the following manner [108].

$$q(j) = \sum_{u=1}^{3} \lambda_u \left(\frac{1}{Z_u} \sum_{i=i_0}^{i_0+Z_u-1} \frac{\boldsymbol{\omega}_0 - \boldsymbol{\omega}(i,j)}{\boldsymbol{\omega}_0} \right) \tag{5.3}$$

$$i_0 = i_a + \frac{u-3}{2} Z_u, \quad \lambda_u \in [0,1], \ \sum_{u=1}^{3} \lambda_u = 1, \quad u = 1,\ 2,\ 3 \tag{5.4}$$

Here, the estimated process states are normalized with respect to the initial value $\boldsymbol{\omega}_0$. The index of the three sampling windows is denoted by u ($u = 1, 2, 3$ corresponding to "Processed", "Current Processing", and "Unprocessed", respectively). The width of each sampling window is represented by Z_u , which is defined as the number of discretized units included in the sampling window. λ_u is the weighting coefficient for each sampling window.

5.2.2 Design of the Control Rules

The coordinated control rules are designed based on some natural characteristics of these robotic radiation-based processes. First, at the beginning of the process, the actuator should stay at the initial position and apply the maximum radiant power to the target strip to drive the local process state close to the desired level as soon as possible. Then, the actuator starts moving and the associated radiant power should be reduced to avoid over-processing in those areas close to the initial position. Once the actuator moves away from the initial position, both the radiant power and speed of the actuator should be adjusted around the nominal values to maintain process uniformity in the presence of disturbances. The detailed control rules will be developed later and applied to the UV curing process for illustration.

It should be noted that the rule-based coordinated control is not necessarily optimal although it uses the off-line optimal nominal radiant power and speed obtained from the open-loop coordination. To achieve closed-loop optimal coordination, a distributed model predictive control (MPC) strategy is developed and applied to these

robotic radiation-based processes described by the 1D scanning formulation. This distributed MPC framework is detailed in the next section.

5.3 Distributed Model Predictive Control

In this section, the model predictive control (MPC) method is used to achieve the online optimal coordination of the radiant power and the speed of the actuator for these robotic radiation-based processes. Compared to typical MPC applications in industry, the development of the distributed MPC strategy poses two major challenges. First, these radiation-based processes are comparatively fast in addition to being distributed-parameter processes and thus require particular attention to the computation time of the online optimization. Second, the movement of the actuator has significant effect on the process and should be incorporated into the control design. The following subsections detail the development of the distributed MPC strategy for robotic radiation-based processes in consideration of these issues.

5.3.1 Model Simplification and Linearization

The generalized 1D scanning model described in Chapter 4 will be used to develop the distributed MPC formulation. However, the major process dynamics described by equations (4.1) and (4.2) are highly nonlinear, which may increase the computation burden when implementing the MPC strategy. Therefore, the nonlinear process model should be simplified and linearized before it is used to develop the MPC strategy.

- Simplification of the Energy Transmission Model

The energy transmission model (equation (4.1)) describes the relationship between the two manipulated variables (the radiant power and the speed) of the actuator and the power distribution on the target strip. To simplify the energy transmission model, the spatial distribution of the radiant power on the target strip can be approximated by using a triangular model illustrated in Figure 5.3.

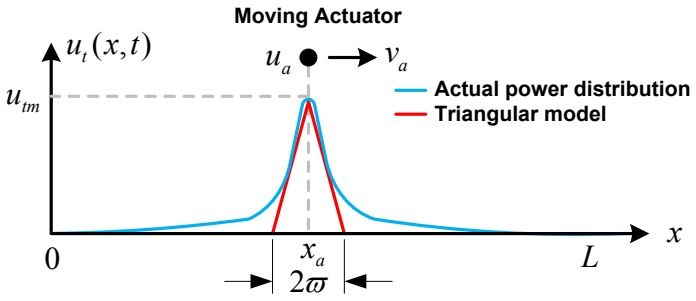

Figure 5.3 The simplified energy transmission model

In Figure 5.3, the height and half width of the triangle are denoted by u_{tm} and ϖ, respectively. The current position of the moving actuator is represented by x_a. The length of the target strip is denoted by L. Assuming that the height of the triangle (u_{tm}) is directly determined by the radiant power u_a, then the triangular model can be mathematically described as follows [109]:

$$u_t(x,t) = 0, \quad x \in [0, x_a - \varpi] \text{ or } x \in [x_a + \varpi, L] \tag{5.5}$$

$$u_t(x,t) = \left(1 + \frac{x}{\varpi}\right) u_{tm} - \frac{u_{tm}}{\varpi} x_a, \quad x \in (x_a - \varpi, x_a) \tag{5.6}$$

$$u_t(x,t) = \left(1 - \frac{x}{\varpi}\right) u_{tm} + \frac{u_{tm}}{\varpi} x_a, \quad x \in (x_a, x_a + \varpi) \tag{5.7}$$

The above triangular model varies with the radiant power (u_a, determining u_{tm}) and the position (x_a) of the moving actuator. Given the triangular model, the small variation of the power distribution from the previous value can be described by retaining first-order terms in the Taylor series expansion of the above equations. The discrete form of this approximation is presented below.

$$\Delta u_t(z,j) = 0, \quad z\Delta x \in \left[0, x_a(n-1) - \varpi\right] \quad \text{or} \quad z\Delta x \in \left[x_a(n-1) + \varpi, L\right] \tag{5.8}$$

$$\Delta u_t(z,j) = \left[1 + \frac{z\Delta x}{\varpi} - \frac{x_a(n-1)}{\varpi}\right]\Delta u_{tm}(j) - \frac{u_{tm}(n-1)}{\varpi}\Delta x_a(j), \quad z\Delta x \in \left(x_a(n-1) - \varpi, x_a(n-1)\right) \tag{5.9}$$

$$\Delta u_t(z,j) = \left[1 - \frac{z\Delta x}{\varpi} + \frac{x_a(n-1)}{\varpi}\right]\Delta u_{tm}(j) + \frac{u_{tm}(n-1)}{\varpi}\Delta x_a(j), \quad z\Delta x \in \left(x_a(n-1), x_a(n-1) + \varpi\right) \tag{5.10}$$

$$j = n,\ n+1,\ \cdots \quad , \tag{5.11}$$

Here, the spatial and temporal indexes are denoted by z and j, respectively. The previous position of the actuator is represented by $x_a(n-1)$, and the previous peak power density on the target strip is denoted by $u_{tm}(n-1)$, corresponding to the previous radiant power of the actuator ($u_a(n-1)$). The spatial step is denoted by Δx. Here, the range of the approximation is taken as the prediction horizon (H_p) that will be discussed later. The definitions of $\Delta u_t(z,j)$, $\Delta u_{tm}(j)$, and $\Delta x_a(j)$ are given below:

$$\Delta u_t(z,j) = u_t(z,j) - u_t(z,n-1) \tag{5.12}$$

$$\Delta u_{tm}(j) = u_{tm}(j) - u_{tm}(n-1) \tag{5.13}$$

$$\Delta x_a(j) = x_a(j) - x_a(n-1) \tag{5.14}$$

$$j = n,\ n+1,\ \cdots \quad , \tag{5.15}$$

The matrix forms of equations (5.8) ~ (5.10) can be represented as follows:

$$\begin{aligned} \Delta \mathbf{u}_t(j) &= \mathbf{u}_t(j) - \mathbf{u}_t(n-1) \\ &= B_a\ \Delta \mathbf{u}_a(j) \end{aligned} \tag{5.16}$$

$$\Delta \mathbf{u}_t(j) = \begin{bmatrix} \Delta u_t(1,j) \\ \vdots \\ \Delta u_t(z,j) \\ \vdots \\ \Delta u_t(N,j) \end{bmatrix}, \quad \Delta \mathbf{u}_a(j) = \begin{bmatrix} \Delta u_{tm}(j) \\ \Delta x_a(j) \end{bmatrix} \tag{5.17}$$

In equation (5.16), the matrix B_a is calculated from the previous peak power density ($u_{tm}(n-1)$) and the position of the actuator ($x_a(n-1)$) by using equations (5.8) ~ (5.10). Since B_a can be treated as a constant matrix within the range of approximation ($j = n,\ n+1,\ \cdots$,), the nonlinear energy transmission model can be linearized by using the above approximation around the previous point.

- Linearization of the State Evolution Model

The state evolution model (equation (4.2)) can also be linearized, using the first-order Taylor series approximation around the previous point. The linearized state evolution model can be represented in the following discrete matrix form:

$$\begin{aligned}\boldsymbol{\omega}(j) &= F_{ST}\left[\boldsymbol{\omega}(j-1),\ \mathbf{u}_t(j-1),\ \mathbf{p}_{ST}\right] \\ &\approx F_{ST}\left[\boldsymbol{\omega}(n-1),\ \mathbf{u}_t(n-1),\ \mathbf{p}_{ST}\right] + \left.\frac{\partial F_{ST}}{\partial \boldsymbol{\omega}}\right|_{n-1}\left[\boldsymbol{\omega}(j-1)-\boldsymbol{\omega}(n-1)\right] \\ &\quad + \left.\frac{\partial F_{ST}}{\partial \mathbf{u}_t}\right|_{n-1}\left[\mathbf{u}_t(j-1)-\mathbf{u}_t(n-1)\right]\end{aligned} \tag{5.18}$$

Substituting equation (5.16) into equation (5.18) yields:

$$\begin{aligned}\boldsymbol{\omega}(j) &\approx F_{ST}\left[\boldsymbol{\omega}(n-1),\ \mathbf{u}_t(n-1),\ \mathbf{p}_{ST}\right] + \left.\frac{\partial F_{ST}}{\partial \boldsymbol{\omega}}\right|_{n-1}\left[\boldsymbol{\omega}(j-1)-\boldsymbol{\omega}(n-1)\right] \\ &\quad + \left.\frac{\partial F_{ST}}{\partial \mathbf{u}_t}\right|_{n-1} B_a\ \Delta\mathbf{u}_a(j-1) \\ &= A\boldsymbol{\omega}(j-1) + B\Delta\mathbf{u}_a(j-1) + B_0\end{aligned} \tag{5.19}$$

$$A = \left.\frac{\partial F_{ST}}{\partial \boldsymbol{\omega}}\right|_{n-1}, \quad B = \left.\frac{\partial F_{ST}}{\partial \mathbf{u}_t}\right|_{n-1} B_a, \quad j = n+1,\ n+2,\ \cdots \quad , \tag{5.20}$$

$$B_0 = F_{ST}\left[\boldsymbol{\omega}(n-1),\ \mathbf{u}_t(n-1),\ \mathbf{p}_{ST}\right] - \left.\frac{\partial F_{ST}}{\partial \boldsymbol{\omega}}\right|_{n-1}\boldsymbol{\omega}(n-1) \tag{5.21}$$

Equations (5.19) ~ (5.21) give the linearization of the nonlinear state evolution model around the previous point. It should be noted that the coefficient matrixes A, B, and B_0 will be updated periodically by using the estimated process states and applied control inputs to maintain the accuracy of the linearized model. This model can be used for predicting future process states within the MPC strategy.

5.3.2 Mathematical Formulation of the Distributed MPC

The fundamental task of MPC is to perform moving finite-horizon optimization to determine the control inputs that should be applied to the process. The optimization is based on predicted future process states within a defined time horizon given current

measurements or estimates of process states. The basic operation mechanism of MPC is illustrated in Figure 5.4 [110].

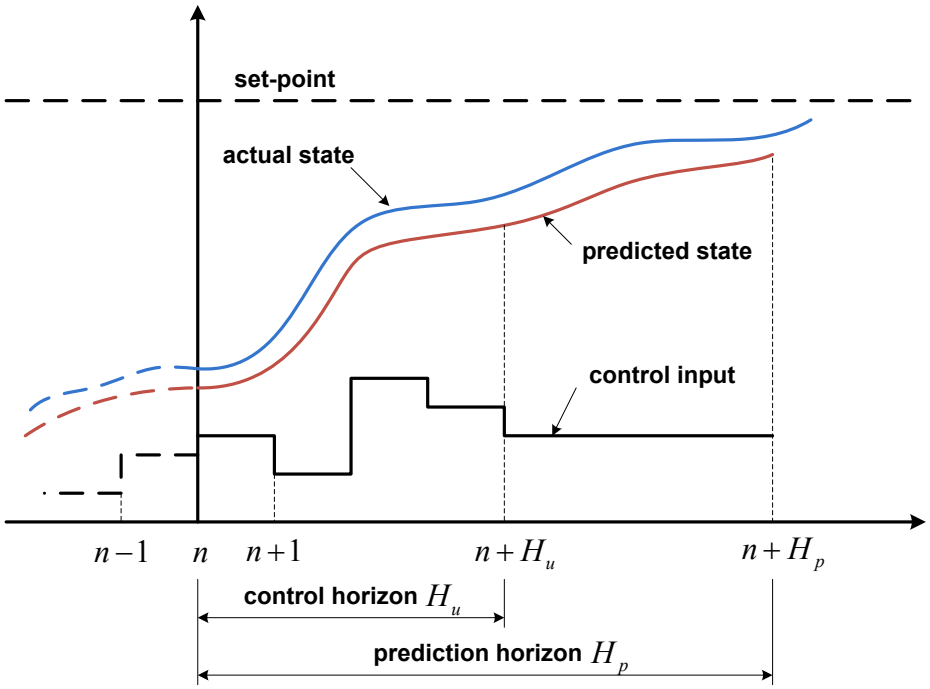

Figure 5.4 The basic operation mechanism of MPC

Here, the previous and current time indexes are denoted by $n-1$ and n, respectively. The prediction horizon H_p defines the time range where the state prediction is performed. The control horizon H_u determines the duration on which the candidate control input is allowed to change in suitably parameterized form (often in discrete steps) so as to achieve a predefined performance objective. The prediction and optimization performed at time n provide the open-loop optimal sequence of control inputs over the current control horizon H_u. These control inputs will be implemented to the system until the next sampling time $(n+1)$. The optimization process is then repeated by using the new measurements or estimates at the next sampling time.

Assuming the process state at time n have been obtained through the DEKF estimation, then the future states starting from time n can be predicted by using the linearized process model described by equations (5.19) ~ (5.21). The following prediction formulation is adapted for this problem from the original version described in [111].

$$\boldsymbol{\omega}(n+1) = A\boldsymbol{\omega}(n) + B\Delta\mathbf{u}_a(n) + B_0 \tag{5.22}$$

$$\begin{aligned}\boldsymbol{\omega}(n+2) &= A\boldsymbol{\omega}(n+1) + B\Delta\mathbf{u}_a(n+1) + B_0 \\ &= A\left[A\boldsymbol{\omega}(n) + B\Delta\mathbf{u}_a(n) + B_0\right] + B\left[\Delta\mathbf{u}_a(n) + \Delta\mathbf{u}_a(n+1\,|\,n)\right] + B_0 \\ &= A^2\boldsymbol{\omega}(n) + \left(AB+B\right)\Delta\mathbf{u}_a(n) + B\Delta\mathbf{u}_a(n+1\,|\,n) + AB_0 + B_0 \\ &= A^2\boldsymbol{\omega}(n) + \left\{\left(AB+B\right), B\right\}\left\{\Delta\mathbf{u}_a(n), \Delta\mathbf{u}_a(n+1\,|\,n)\right\}^{\mathbf{T}} + \left(A+I\right)B_0\end{aligned} \tag{5.23}$$

$$\vdots$$

$$\boldsymbol{\omega}(n+H_u) = A^{H_u}\boldsymbol{\omega}(n) + \Gamma_0\left\{\Delta\mathbf{u}_a(n), \cdots \quad + H_u - 1\,|\,n+H_u-2)\right\}^{\mathbf{T}} + \Theta_0 B_0 \tag{5.24}$$

$$\boldsymbol{\omega}(n+H_u+1) = A^{H_u+1}\boldsymbol{\omega}(n) + \Gamma_1\left\{\Delta\mathbf{u}_a(n), \cdots \quad + H_u - 1\,|\,n+H_u-2)\right\}^{\mathbf{T}} + \Theta_1 B_0 \tag{5.25}$$

$$\vdots$$

$$\boldsymbol{\omega}(n+H_p) = A^{H_p}\boldsymbol{\omega}(n) + \Gamma_\delta\left\{\Delta\mathbf{u}_a(n), \cdots \quad + H_u - 1\,|\,n+H_u-2)\right\}^{\mathbf{T}} + \Theta_\delta B_0 \tag{5.26}$$

$$\delta = H_p - H_u \tag{5.27}$$

The definitions of $\Gamma_0 \sim \Gamma_\delta$ and $\Theta_0 \sim \Theta_\delta$ are given by:

$$\Gamma_0 = \left\{\sum_{i=0}^{H_u-1} A^i B,\ \sum_{i=0}^{H_u-2} A^i B,\ \cdots \qquad \cdots \right. \tag{5.28}$$

$$\Gamma_1 = \left\{\sum_{i=0}^{H_u} A^i B,\ \sum_{i=0}^{H_u-1} A^i B,\ \cdots \qquad \cdots \right. \tag{5.29}$$

$$\vdots$$

$$\Gamma_\delta = \left\{\sum_{i=0}^{H_p-1} A^i B,\ \sum_{i=0}^{H_p-2} A^i B,\ \cdots \qquad \cdots \right. \tag{5.30}$$

The control input increments shown in the above equations are defined as follows:

$$\Delta \mathbf{u}_a(n) = \mathbf{u}_a(n) - \mathbf{u}_a(n-1) \tag{5.31}$$

$$\begin{aligned} \Delta \mathbf{u}_a(n+1) &= \mathbf{u}_a(n+1) - \mathbf{u}_a(n-1), \\ \Delta \mathbf{u}_a(n+1 \mid n) &= \mathbf{u}_a(n+1) - \mathbf{u}_a(n) \end{aligned} \tag{5.32}$$

$$\vdots$$

$$\begin{aligned} \Delta \mathbf{u}_a(n+H_u-1) &= \mathbf{u}_a(n+H_u-1) - \mathbf{u}_a(n-1), \\ \Delta \mathbf{u}_a(n+H_u-1 \mid n+H_u-2) &= \mathbf{u}_a(n+H_u-1) - \mathbf{u}_a(n+H_u-2) \end{aligned} \tag{5.33}$$

The matrix form of the above prediction formulation can be represented as:

$$\mathbf{W}_f = \gamma \boldsymbol{\omega}(n) + \xi \, \Delta \mathbf{U}_a + \eta B_0 \tag{5.34}$$

$$\mathbf{W}_f = \begin{bmatrix} \boldsymbol{\omega}(n+1) \\ \boldsymbol{\omega}(n+2) \\ \vdots \\ \boldsymbol{\omega}(n+H_u) \\ \boldsymbol{\omega}(n+H_u+1) \\ \vdots \\ \boldsymbol{\omega}(n+H_p) \end{bmatrix}, \quad \Delta \mathbf{U}_a = \begin{bmatrix} \Delta \mathbf{u}_a(n) \\ \Delta \mathbf{u}_a(n+1 \mid n) \\ \vdots \\ \Delta \mathbf{u}_a(n+H_u-1 \mid n+H_u-2) \end{bmatrix} \tag{5.35}$$

$$\gamma = \begin{bmatrix} A \\ A^2 \\ \vdots \\ A^{H_u} \\ A^{H_u+1} \\ \vdots \\ A^{H_p} \end{bmatrix}, \quad \xi = \begin{bmatrix} B & 0 & \cdots & 0 \\ (A+I)B & B & \cdots & 0 \\ \vdots & \vdots & \ddots & \vdots \\ \sum_{i=0}^{H_u-1} A^i B & \sum_{i=0}^{H_u-2} A^i B & \cdots & B \\ \sum_{i=0}^{H_u} A^i B & \sum_{i=0}^{H_u-1} A^i B & \cdots & \vdash I)B \\ \vdots & \vdots & \ddots & \vdots \\ \sum_{i=0}^{H_p-1} A^i B & \sum_{i=0}^{H_p-2} A^i B & \cdots & {}^{-H_u} A^i B \end{bmatrix}, \quad \eta = \begin{bmatrix} I \\ A+I \\ \vdots \\ \sum_{i=0}^{H_p-1} A^i \end{bmatrix} \tag{5.36}$$

Equation (5.34) shows that the future states ($\mathbf{W}_f$) over the prediction horizon are calculated from the estimated state at time n ($\boldsymbol{\omega}(n)$) and the sequence of control input

increments ($\Delta\mathbf{U}_a$) to be determined over the control horizon. Given the prediction formulation described in equations (5.34) ~ (5.36), the optimization objective can be represented as follows:

$$\min \quad V(\Delta\mathbf{U}_a) = \left(\mathbf{W}_f - \mathbf{W}_{f0}\right)^{\mathbf{T}} Q\left(\mathbf{W}_f - \mathbf{W}_{f0}\right) + \left(\Delta\mathbf{U}_a\right)^{\mathbf{T}} R_1\left(\Delta\mathbf{U}_a\right) + \left(\mathbf{U}_a\right)^{\mathbf{T}} R_2\left(\mathbf{U}_a\right) \tag{5.37}$$

$$\text{subject to} \quad \mathbf{W}_f = \gamma\boldsymbol{\omega}(n) + \xi\,\Delta\mathbf{U}_a + \eta B_0, \quad \mathbf{U}_a = \Upsilon\mathbf{u}_a(n-1) + \Psi\Delta\mathbf{U}_a \tag{5.38}$$

$$\mathbf{W}_{f,lb} \le \mathbf{W}_f \le \mathbf{W}_{f,ub}, \ \Delta\mathbf{U}_{a,lb} \le \Delta\mathbf{U}_a \le \Delta\mathbf{U}_{a,ub}, \ \mathbf{U}_{a,lb} \le \mathbf{U}_a \le \mathbf{U}_{a,ub} \tag{5.39}$$

$$\Upsilon = \begin{bmatrix} I \\ I \\ \vdots \\ I \end{bmatrix} \quad \text{and} \quad \begin{bmatrix} I & 0 & \cdots & \\ I & I & \cdots & \vdots \\ \vdots & \vdots & \ddots & \\ I & \cdots & & \end{bmatrix} \quad \begin{bmatrix} 1 & 0 \\ 0 & 1 \end{bmatrix} \tag{5.40}$$

Here, the three positive semi-definite matrices Q , R_1 and R_2 denote the weighting coefficients which penalize the state error, control input change, and control input, respectively. Substituting the two equality constraints described in equation (5.38) into equation (5.37), we can express the cost function in the following form:

$$\begin{aligned} V(\Delta\mathbf{U}_a) = &\left(\xi\,\Delta\mathbf{U}_a + \mathbf{E}_{\boldsymbol{\omega}}\right)^{\mathbf{T}} Q\left(\xi\,\Delta\mathbf{U}_a + \mathbf{E}_{\boldsymbol{\omega}}\right) + \left(\Delta\mathbf{U}_a\right)^{\mathbf{T}} R_1\left(\Delta\mathbf{U}_a\right) \\ &+ \left(\mathbf{D}_{\mathbf{u}} + \Psi\Delta\mathbf{U}_a\right)^{\mathbf{T}} R_2\left(\mathbf{D}_{\mathbf{u}} + \Psi\Delta\mathbf{U}_a\right) \end{aligned} \tag{5.41}$$

$$\mathbf{E}_{\boldsymbol{\omega}} = \gamma\boldsymbol{\omega}(n) + \eta B_0 - \mathbf{W}_{f0}, \quad \mathbf{D}_{\mathbf{u}} = \Upsilon\mathbf{u}_a(n-1) \tag{5.42}$$

Equation (5.41) can be reduced to:

$$V(\Delta\mathbf{U}_a) = Z_1\left(\Delta\mathbf{U}_a\right) + \left(\Delta\mathbf{U}_a\right)^{\mathbf{T}} Z_2\left(\Delta\mathbf{U}_a\right) + Z_3 \tag{5.43}$$

$$Z_1 = 2\left[\left(\mathbf{E}_{\boldsymbol{\omega}}\right)^{\mathbf{T}} Q\xi + \left(\mathbf{D}_{\mathbf{u}}\right)^{\mathbf{T}} R_2\Psi\right], \ Z_2 = \xi^{\mathbf{T}} Q\xi + R_1 + \Psi^{\mathbf{T}} R_2\Psi \tag{5.44}$$

$$Z_3 = \left(\mathbf{E}_{\boldsymbol{\omega}}\right)^{\mathrm{T}} Q\mathbf{E}_{\boldsymbol{\omega}} + \left(\mathbf{D}_{\mathbf{u}}\right)^{\mathrm{T}} R_2\mathbf{D}_{\mathbf{u}} \tag{5.45}$$

Here, Z_3 is a constant during the current optimization cycle, and thus it can be eliminated from the cost function. The inequality constraints described in equation (5.39) can also be represented in terms of $\Delta\mathbf{U}_a$:

$$\xi^{-1}\left[\mathbf{W}_{f,\,lb} - \gamma\boldsymbol{\omega}(n) - \eta B_0\right] \le \Delta\mathbf{U}_a \le \xi^{-1}\left[\mathbf{W}_{f,\,ub} - \gamma\boldsymbol{\omega}(n) - \eta B_0\right] \tag{5.46}$$

$$\Delta\mathbf{U}_{a,\,lb} \le \Delta\mathbf{U}_a \le \Delta\mathbf{U}_{a,\,ub} \tag{5.47}$$

$$\Psi^{-1}\left[\ \mathbf{U}_{a,\,lb} - \Upsilon\mathbf{u}_a(n-1)\right] \le \Delta\mathbf{U}_a \le \Psi^{-1}\left[\mathbf{U}_{a,\,ub} - \Upsilon\mathbf{u}_a(n-1)\right] \tag{5.48}$$

Given the above transformations, the original optimization problem described in equations (5.37) ~ (5.39) can be reduced to a quadratic programming (QP) problem summarized as follows:

$$\min \quad V'(\Delta\mathbf{U}_a) = Z_1\left(\Delta\mathbf{U}_a\right) + \left(\Delta\mathbf{U}_a\right)^{\mathrm{T}} Z_2\left(\Delta\mathbf{U}_a\right) \tag{5.49}$$

$$\text{subject to} \quad \ell \qquad\qquad \ell \tag{5.50}$$

$$\ell \qquad \left\{\xi^{-1}\left[\mathbf{W}_{f,\,lb} - \gamma\boldsymbol{\omega}(n) - \eta B_0\right],\ \Delta\mathbf{U}_{a,\,lb},\ \Psi^{-1}\left[\ \mathbf{U}_{a,\,lb} - \Upsilon\mathbf{u}_a(n-1)\right]\right\} \tag{5.51}$$

$$\ell \qquad \left\{\xi^{-1}\left[\mathbf{W}_{f,\,ub} - \gamma\boldsymbol{\omega}(n) - \eta B_0\right],\ \Delta\mathbf{U}_{a,\,ub},\ \Psi^{-1}\left[\ \mathbf{U}_{a,\,ub} - \Upsilon\mathbf{u}_a(n-1)\right]\right\} \tag{5.52}$$

The solution of the above QP problem $\Delta\mathbf{U}_a^*$ gives the sequence of the optimal control input increments that can achieve the defined performance objective over the prediction horizon. Then, the actual control input that will be applied to the process during the time $\left[n,\ n+1\right]$ is obtained by:

$$\begin{aligned}\mathbf{u}_a^*(n) &= \mathbf{u}_a(n-1) + \Delta\mathbf{u}_a^*(n) \\ &= \mathbf{u}_a(n-1) + \Delta\mathbf{U}_a^*\left(1 : N_{\mathbf{u}_a}\right)\end{aligned} \tag{5.53}$$

Here, $N_{\mathbf{u}_a}$ denotes the number of manipulated variables included in the control input vector $\mathbf{u}_a$. The optimal control input solved at time n ($\mathbf{u}_a^*(n)$) will be applied to the process until the next sampling time ($n+1$). Then, with the new state estimates at time $n+1$, the above optimization will be repeated.

The dimension of the predicted future state vector $\mathbf{W}_f$ should be reduced as much as possible when implementing the above MPC strategy to the distributed-parameter radiation-based processes. A subsystem, which includes the states of the areas on the target strip dominantly illuminated by the moving actuator, is selected to perform the above prediction and optimization. This is consistent with the activating policy used in the DEKF estimation scheme as discussed in Chapter 4. In other words, the prediction and optimization are only performed on those discretized units that are included in the activating window.

5.4 Simulation Results

In this section, a simulation study of the robotic UV curing process is presented to illustrate the coordinated control and process optimization methods described in the previous sections. First, the open-loop coordination is implemented to determine the optimal nominal radiant power and speed of the moving actuator. This is followed by the implementation of a rule-based feedback control to the curing process to achieve closed-

loop coordination. Finally, the distributed MPC strategy developed in Section 5.3 will be applied and verified.

In this simulation study, the robotic UV curing process is described by the 1D nonlinear model that has been used in Chapter 4. The associated process parameters remain the same as those listed in Table 4.1 and Table 4.2. The distributed DEKF estimation scheme is also used in this simulation to provide essential state estimation for the rule-based coordinated control and the distributed MPC.

5.4.1 Results of the Open-loop Coordination

The open-loop coordination problem described by equations (5.1) and (5.2) is adapted for the robotic UV curing process as follows:

$$\min \quad J(v_a, \varphi) = q_1 \varphi^2 + q_2 \frac{1}{v_a^2} \tag{5.54}$$

$$\text{subject to} \quad f_q(v_a, \varphi) = \alpha_d - \left[1 - e^{f_2}\right] = 0 \tag{5.55}$$

$$v_{lb} \le v_a \le v_{ub}, \quad \varphi_{lb} \le \varphi \le \varphi_{ub} \tag{5.56}$$

$$f_2 = \eta_1' \left(\frac{k}{\pi}\right)^{0.5} \frac{\varphi^{0.5}}{v_a} \left(2 \arctan \frac{L_t}{2d_0}\right) e^{\eta_2' \frac{k}{2\pi} \frac{\varphi}{v_a} \left[\frac{1}{d_0}\left(\arctan \frac{L_t}{2d_0}\right) + \frac{2L_t}{(L_t)^2 + 4d_0^2}\right]} \tag{5.57}$$

$$\eta_1' = -\kappa \left\{\phi \varepsilon [PI](x, t_0)\right\}^{0.5}, \quad \eta_2' = -\frac{1}{2} \phi \varepsilon \tag{5.58}$$

The derivation of the equality constraint equation $f_q(v_a, \varphi) = 0$ is detailed in Appendix-A. In this open-loop coordination, the chemical and material parameters of the UV curing process are listed in Table 4.2. Other parameters associated with the above optimization problem are listed in Table 5.1.

Table 5.1 Parameters associated with the open-loop coordination

Description	**Notation**	**Value and unit**
Total moving distance	L_t	1 m
Normal distance	d_0	0.03 m
UV absorption coefficient	k	1
Desired cure-conversion level	α_d	0.85
Lower boundary of speed	v_{lb}	0.02 m/s
Upper boundary of speed	v_{ub}	0.1 m/s
Lower boundary of radiant power	φ_{lb}	10 W
Upper boundary of radiant power	φ_{ub}	50 W

The results of the open-loop coordination for the robotic UV curing process are given in Table 5.2.

Table 5.2 Optimization results for different weighting coefficients

Weighting coefficients	**Optimal radiant power (W)**	**Optimal speed (m/s)**
$q_1 = 10,\ \ q_2 = 1$	10.0	0.022
$q_1 = 5,\ \ q_2 = 1$	12.5	0.025
$q_1 = 1,\ \ q_2 = 1$	21.6	0.032
$q_1 = 1,\ \ q_2 = 5$	37.1	0.041
$q_1 = 1,\ \ q_2 = 15$	50.0	0.046

The results in Table 5.2 show that the lower boundary (10 W) of the radiant power is reached when we use a set of weighting coefficients that penalizes energy cost more than process efficiency. On the other hand, the maximum radiant power (50 W) is used to achieve the highest process efficiency. These are as should be expected. The other listed weighting coefficient combinations reflect the trade-off between energy cost and

process efficiency and give corresponding optimal values for the radiant power and the speed.

5.4.2 Results of the Rule-based Coordinated Control

In this subsection, the rule-based coordinated control strategy is implemented to the robotic UV curing process. The coordination of the radiant power and the speed is performed around the nominal values determined by the open-loop coordination, based on the estimated process state and some designed rules presented in Table 5.3 [108].

Table 5.3 The control coordination rules

Error ($e=\alpha-\alpha_d$)	**Control rules**
$c_2<\lvert e\rvert\le\lvert e\rvert_m$	$v_a=0,\ \varphi=\varphi_m$
$c_1<\lvert e\rvert\le c_2$	$v_a=v_{a0}+K_p'e,\ \varphi=\frac{1}{2}\varphi_m$
$\lvert e\rvert\le c_1$	$v_a=v_{a0}+\left(K_{pv}e+K_{iv}\int edt+K_{dv}\right.$

Here, the error of the actual and desired cure-conversion levels (denoted by α and α_d, respectively) is the major factor that is considered in designing these control rules [112, 113]. As shown in Table 5.3, the range of the absolute value of the error is divided into three zones: $[0,c_1]$, $(c_1,c_2]$, and $\left(c_2,\lvert e\rvert_m\right]$. The maximum value of $\lvert e\rvert$ is represented by $\lvert e\rvert_m$, which usually occurs at the beginning of the process. The nominal values of the radiant power and the speed are denoted by φ_0 and v_{a0}, respectively. The maximum radiant power is represented by φ_m. The designed control rules can be explained as follows.

When $|e|$ is located in the zone $\left(c_2, |e|_m\right]$, for example, at the beginning of the curing process, the actuator stays at its original position and applies the maximum radiant power to reduce the error quickly. After the error has been brought to the zone $\left(c_1, c_2\right]$, the radiant power is cut to half of its maximum value and the actuator begins to move. In the mean time, a proportional controller is used to adjust the speed of the actuator. Once the error further falls to the zone $\left[0, c_1\right]$, the speed of the actuator is adjusted by a new PID controller around its nominal value and the radiant power is regulated by another PID controller.

The simulation parameters associated with the rule-based coordinated control for the UV curing process are listed in Table 5.4. The chemical parameters, estimation-related parameters and other parameters are as listed in Table 4.1 ~ Table 4.3.

Table 5.4 Parameters associated with the rule-based coordinated control

Description	**Notation**	**Value and unit**
Desired cure-conversion level	α_d	0.85
Nominal speed	v_{a0}	0.041 m/s
Nominal radiant power	φ_0	37.1 W
Maximum radiant power	φ_m	50 W
Sampling window width	Z_u	$Z_1 = Z_2 = Z_3 = 6$ (discretized units)
Sampling window weight coefficient	λ_u	$\lambda_1 = \frac{1}{3},\ \lambda_2 = \frac{1}{3},\ \lambda_3 = \frac{1}{3}$ (actuator rests) $\lambda_1 = \frac{1}{2},\ \lambda_2 = \frac{1}{3},\ \lambda_3 = \frac{1}{6}$ (actuator moves)
Feedback signal	α	$\alpha(j) = \sum_{u=1}^{3} \lambda_u \left(\frac{1}{Z_u} \sum_{i=i_0}^{i_0+Z_u-1} \frac{[M]_0 - [M](i,j)}{[M]_0} \right)$

		$i_0 = i_a + \frac{u-3}{2} Z_u,\ u = 1,\ 2,\ 3$
Error signal	e	$e = \alpha - \alpha_d$
Error signal threshold	$c_1,\ c_2$	$c_1 = 0.04,\ c_2 = 0.25$
Control gains (speed control)	$K'_p, K_{pv}, K_{iv}, K_{dv}$	$K'_p = 0.085,$ $K_{pv} = 0.35, K_{iv} = 0.05, K_{dv} = 0.07$
Control gains (power control)	$K_{p\varphi}, K_{i\varphi}, K_{d\varphi}$	$K_{p\varphi} = 100, K_{i\varphi} = 10, K_{d\varphi} = 5$
Disturbance (UV absorption)	$k(x)$	$k(x) = -2x/7 + 0.8$ (Scenario-1) $k(x) = \begin{cases} 0.8, x \in [0,\ 0.7\ \text{m}] \\ 0.4, x \in (0.7,\ 1.4\ \text{m}] \end{cases}$ (Scenario-2)

Two simulation scenarios (Scenario-1 and -2) are considered in order to demonstrate the developed rule-based coordinated control strategy. In Scenario-1, the disturbance is introduced by defining a tilted distribution of the UV absorption coefficient on the target strip ($k(x) = -2x/7 + 0.8$). For Scenario-2, an uneven distribution of the UV absorption is characterized by a step function defined in the last row of Table 5.4. The simulation results for Scenario-1 are illustrated in Figure 5.5 ~ Figure 5.6.

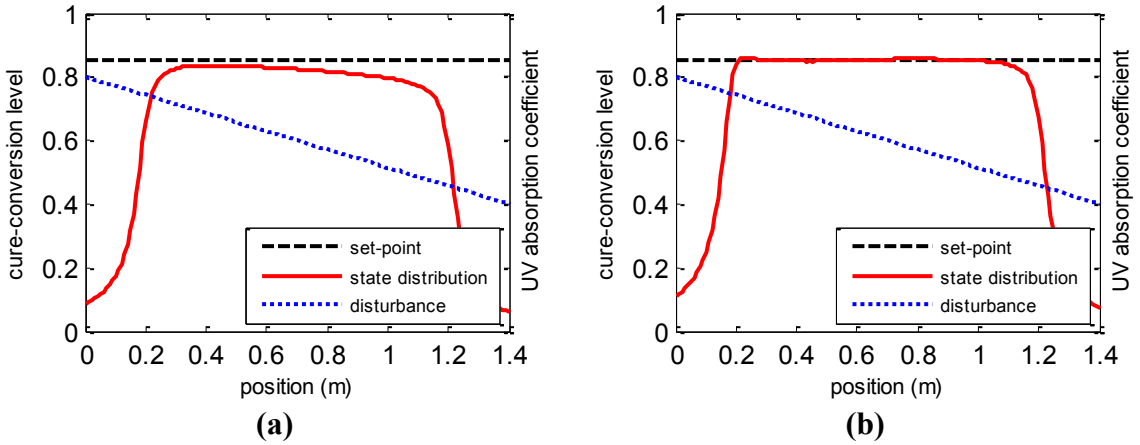

Figure 5.5 Cure-conversion level distributions on the target strip (Scenario-1): (a) open-loop curing; (b) rule-based coordinated control

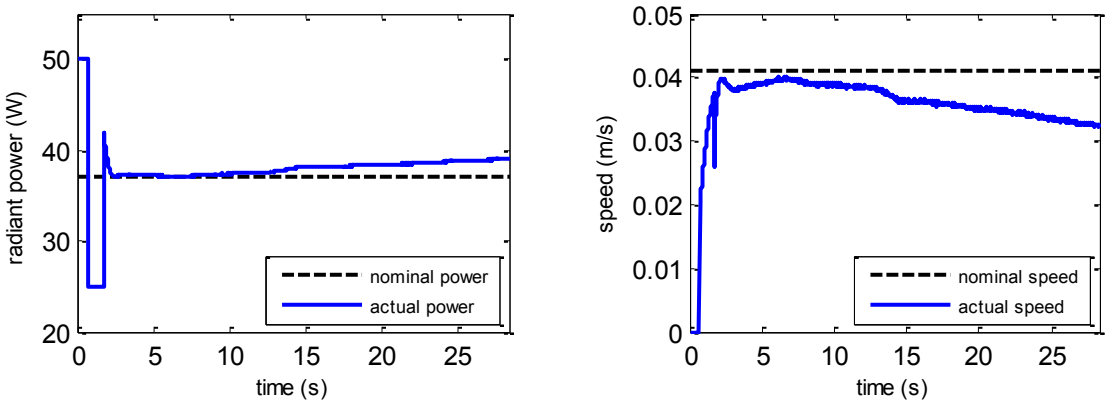

Figure 5.6 Time history of control signals (Scenario-1): (a) radiant power; (b) speed

The result in Figure 5.5(a) shows that a deviation of the distribution of cure-conversion level from the set-point occurs when the nominal radiant power and speed obtained from the open-loop coordination are applied. This is caused by the tilted uneven distribution of the UV absorption coefficient illustrated by the blue dot line. As shown in Figure 5.5(b), the cure quality is improved by implementing the closed-loop rule-based coordinated control strategy. The time history of control signals depicted in Figure 5.6 show that the radiant power is increased and the speed is reduced following the online estimated process state and the designed control rules. The adjusted radiant power and speed (around the nominal values) are able to compensate for the tilted disturbance and maintain cure uniformity, compared to the open-loop approach.

The simulation results of Scenario-2 are given in Figure 5.7 ~ Figure 5.8.

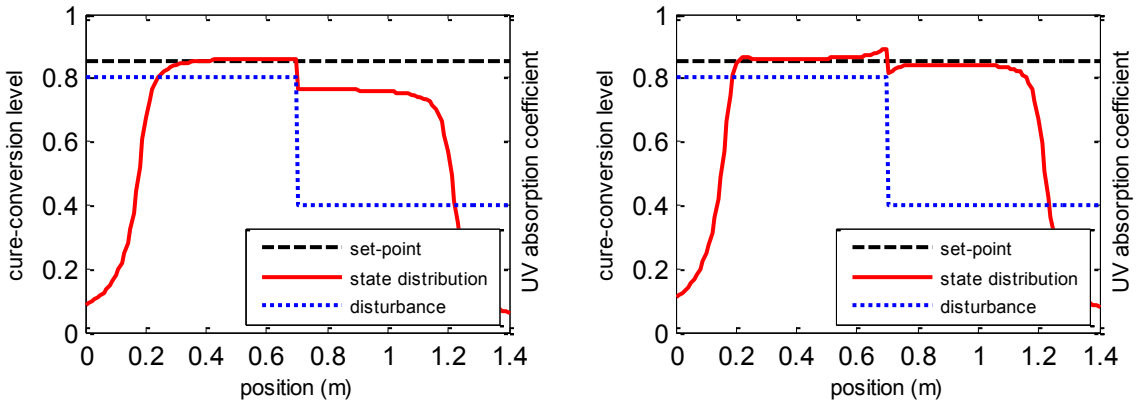

Figure 5.7 Cure-conversion level distributions on the target strip (Scenario-2): (a) open-loop curing; (b) rule-based coordinated control

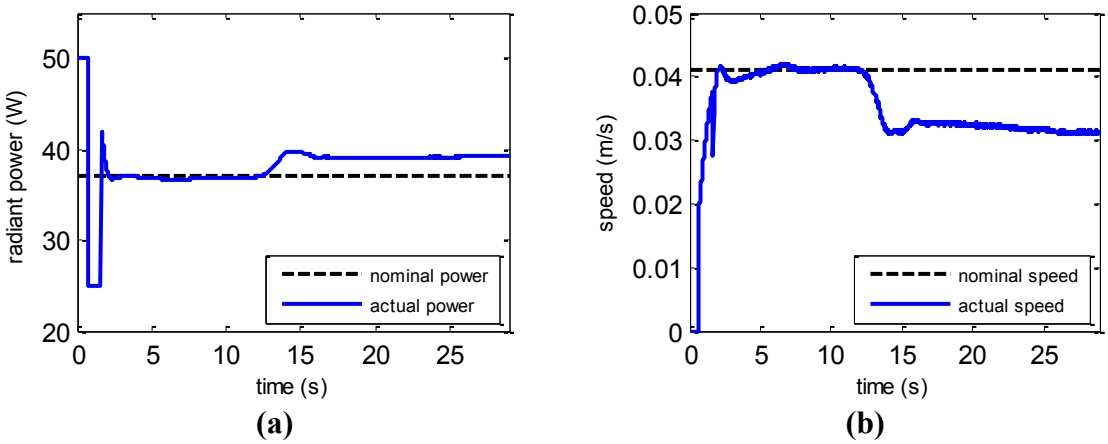

Figure 5.8 Time history of control signals (Scenario-2): (a) radiant power; (b) speed

Similarly, the open-loop curing cannot maintain cure uniformity in the presence of the stepped disturbance in UV absorption, as shown in Figure 5.7(a). The unevenness of cure-conversion level distribution has been improved by using the same rule-based coordination control strategy as used in Scenario-1. In this case, the radiant power and the speed are adjusted to mitigate the effect of the stepped disturbance on cure uniformity.

The results for the two scenarios demonstrate that the closed-loop rule-based coordinated control of the robotic UV curing process can significantly improve the cure quality in the presence of different types of disturbances which the open-loop curing fails to compensate for.

5.4.3 Results of the Distributed MPC

This subsection discusses the implementation of the distributed MPC strategy to the UV curing process. The control input is determined in an optimal manner, using the online state estimation and the designed moving finite-horizon optimization algorithm. The simulation parameters are listed in Table 5.5.

Table 5.5 Simulation parameters for the distributed MPC

Description	**Notation**	**Value and unit**
Time step of simulation	dt	0.01 s
MPC calculation period	T_{MPC}	0.07 s
Prediction horizon	H_p	0.56 s ($8T_{MPC}$)
Control horizon	H_c	0.42 s ($6T_{MPC}$)
Dimension of the MPC	-	30 (discretized units)
Input constraints	$\mathbf{u}_{a,\,lb}$, $\mathbf{u}_{a,\,ub}$	$\mathbf{u}_{a,\,lb}=\begin{bmatrix}0\\0.2\end{bmatrix}$, $\mathbf{u}_{a,\,ub}=\begin{bmatrix}50\\1.2\end{bmatrix}$ (W) (m)
Input change constraints	$\Delta\mathbf{u}_{a,\,lb}$, $\Delta\mathbf{u}_{a,\,ub}$	$\Delta\mathbf{u}_{a,\,lb}=\begin{bmatrix}-10\\-0.1\end{bmatrix}$, $\Delta\mathbf{u}_{a,\,ub}=\begin{bmatrix}10\\0.1\end{bmatrix}$ (W/s) (m/s)

The performance of the controller is mainly influenced by the three weighting matrices: Q, R_1, and R_2, which penalize the state error, control input change, and control input, respectively. The last two matrices are treated as constant during the whole process.

The matrix Q varies with the movement of the actuator, and the generation of this matrix is detailed in Table 5.6 below.

Table 5.6 The generation of the weighting matrix Q (Example)

Actuator's position x_a (m)	**Weighting matrix** Q: $Q = \underset{i=1,2,\cdots}{\mathbf{diag}}\{Q_i\},\ Q_i = \underset{\cdots}{\mathbf{diag}}\{q_z\}$
$x_a = 0.2$	$q_z = \begin{cases} 8\times10^{-6},\ 1 \le z < X_a - 4 \\ 2\times10^{-3},\ X_a - 4 \le z \le X_a + 4 \\ 8\times10^{-6},\ X_a + 4 < z \le N \end{cases}$
$0.2 < x_a \le 0.26$	$q_z = \begin{cases} 8\times10^{-6},\ 1 \le z < X_a - 4 \\ 2\times10^{-3},\ X_a - 4 \le z \le X_a - 1 \\ 7\times10^{-3},\ X_a \le z \le X_a + 4 \\ 8\times10^{-6},\ X_a + 4 < z \le N \end{cases}$
$0.26 < x_a \le 1.2$	$q_z = \begin{cases} 8\times10^{-6},\ 1 \le z < X_a - 4 \\ 1.3\times10^{-2},\ X_a - 4 \le z \le X_a - 1 \\ 2\times10^{-3},\ X_a \le z \le X_a + 4 \\ 8\times10^{-6},\ X_a + 4 < z \le N \end{cases}$

Here, Q_i denotes the sub-matrices that constitute the weight matrix Q, and q_z represents the elements of each sub-matrix. The dimension of these sub-matrices is denoted by N, which is equal to the total number of discretized units that comprise the target strip. X_a represents the index of the element that is corresponding to the actuator's position x_a. As shown in Table 5.6, these sub-matrices Q_i are designed in a symmetric manner at the beginning ($x_a = 0.2\,\text{m}$). This will make the radiant actuator continue curing the area around the initial position without moving. Once the cure-conversion level of this area is close to the set-point (determined from the error signal), asymmetric sub-

matrices (penalize more on uncured areas) are used to initialize the movement of the actuator. After the normal gradient of monomer concentration has been established (the actuator travels a certain distance away from the initial position), the direction of the asymmetry is reversed. In this case, the weighting matrix will penalize more on cured areas to maintain the uniformity of the error signal.

The selection of weighting matrices R_1 and R_2 influences the balance in minimizing the state error, and the corresponding costs for the control input and control input change. The following values of R_1 and R_2 are chosen for the simulations by considering the trade-off among these factors.

Table 5.7 The selection of weighting matrices R_1 and R_2 (Example)

Weighting matrix	Value
R_1	$R_1 = \underset{i=1,2,\cdots}{\mathbf{diag}}\{R_{1,i}\},\ R_{1,i} = \begin{bmatrix} 2.4\times10^3 & \\ & 3.6\times10^3 \end{bmatrix}$
R_2	$R_2 = \underset{i=1,2,\cdots}{\mathbf{diag}}\{R_{2,i}\},\ R_{2,i} = \begin{bmatrix} 33.6 & \\ & 0 \end{bmatrix}$

The same simulation scenarios used in the previous subsection are considered for demonstrating the distributed MPC strategy. The corresponding results for Scenario-1, in comparison with those of the open-loop coordination and rule-based coordinated control, are presented in Figure 5.9 ~ Figure 5.10.

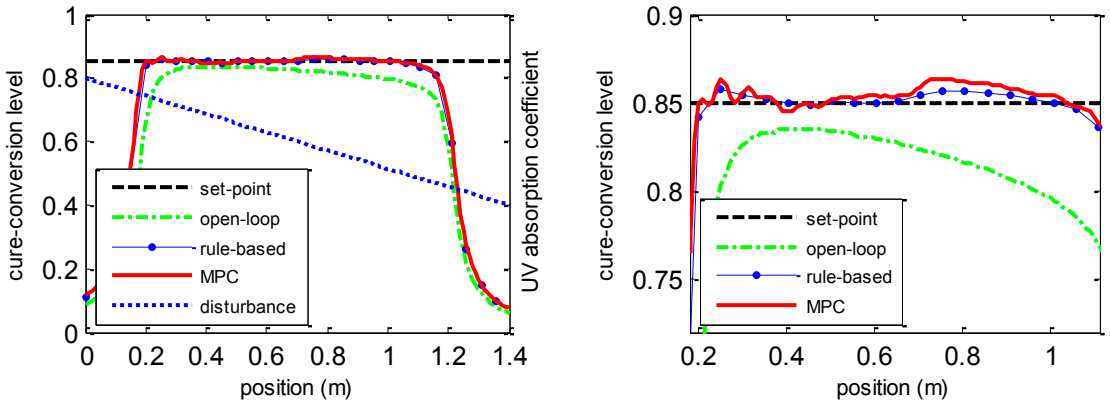

Figure 5.9 Cure-conversion level distributions for three curing methods (Scenario-1): (a) Full-range view (b) Zoomed around the set-point

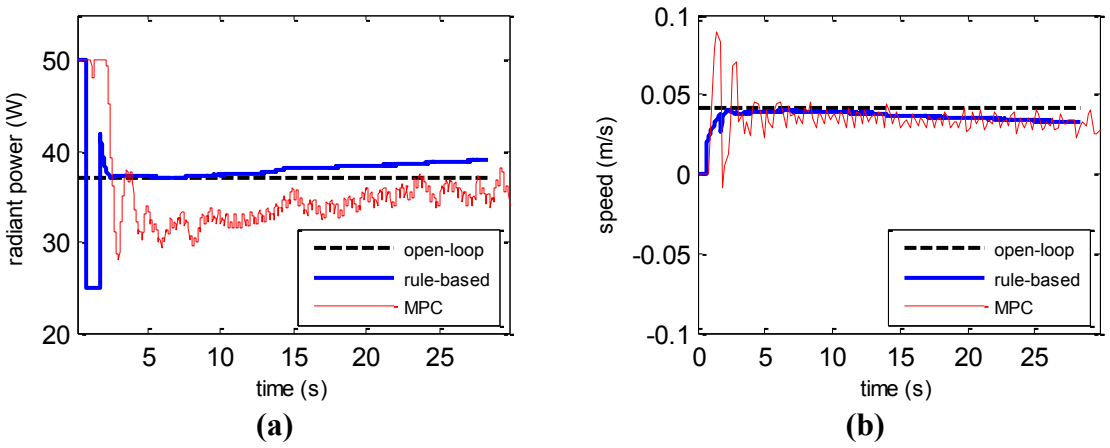

Figure 5.10 Time history of control signals for three curing methods (Scenario-1): (a) radiant power; (b) speed

As shown in Figure 5.9, both the MPC and rule-based control methods are able to maintain the cure uniformity in the presence of decreasing UV absorption coefficient, compared to the open-loop coordination. This is because both of the two closed-loop approaches use estimated process state as feedback to adjust the radiant power and the speed of the actuator online. The result in Figure 5.10(a) shows that the MPC approach implements lower radiant power than the rule-based coordinated control method for most

of the curing duration. This can be explained by the fact that the MPC approach has explicitly considered the minimization of both the state error and the control input costs along the prediction horizon during each calculation period. The speed profiles in Figure 5.10(b) show that the MPC strategy exposes more options through adjusting the speed of the actuator. The radiant actuator can even go back to previously cured area if necessary.

The simulation results of Scenario-2 are given in Figure 5.11 ~ Figure 5.12.

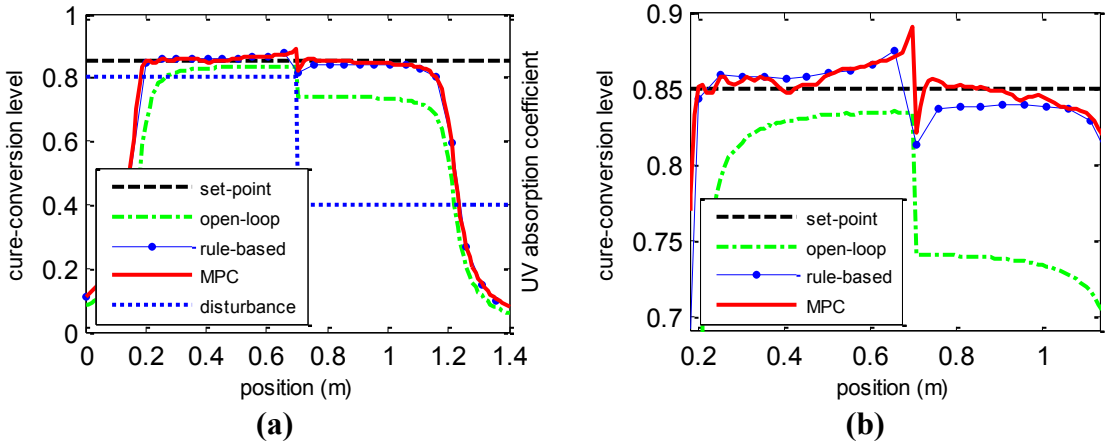

Figure 5.11 Cure-conversion level distributions for three curing methods (Scenario-2): (a) Full-range view (b) Zoomed around the set-point

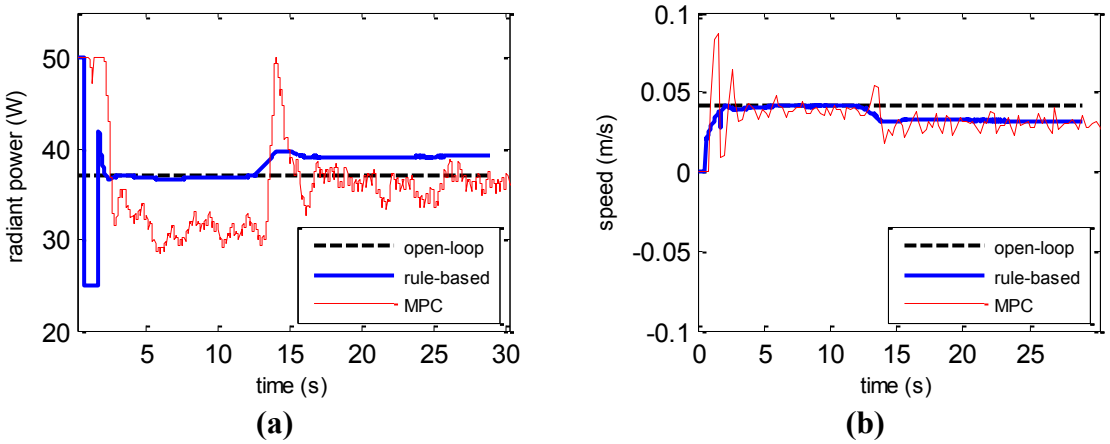

Figure 5.12 Time history of control signals for three curing methods (Scenario-2): (a) radiant power; (b) speed

In this scenario, the same MPC controller is used to control the curing process occurring on the target strip where the UV absorption coefficient has a step change between the left and right sides. This unevenness has also been successfully compensated for by applying either the rule-based coordinated control or the MPC strategy, as shown in Figure 5.11. Compared to the rule-based coordinated control, the MPC method gives a better match with the set-point after the actuator enters the area with lower UV absorption coefficient. This can be explained by the results shown in Figure 5.12(a). The MPC controller increases the radiant power more drastically than the rule-base coordinated controller does, when the actuator crosses the intermediate region between the low-absorption and high-absorption areas. The corresponding speed profiles illustrated in Figure 5.12(b) also show that the MPC controller reduces the speed of the actuator to compensate for the change in UV absorption coefficients between the left and right parts of the target strip. It is also observed that the MPC gives rather noisy actuation inputs as it seeks the optimal solutions at each calculation cycle.

The major difference between the rule-based coordinated control and the MPC approach can be described as follows. In the rule-based coordinated control approach, the radiant power and the speed are adjusted around nominal values obtained from the open-loop coordination. In the MPC approach, the online optimization algorithm directly determines the radiant power and the position (or speed), subject to the defined constraints on the control input and input change. In this case, although no nominal radiant power and speed are applied, the MPC strategy still succeeds in maintaining the cure uniformity in the presence of different types of disturbances in UV absorption

coefficient. The simulation results also show that the MPC approach can be designed for achieving lower power use than the rule-based coordinated control method by selecting appropriate weighting matrices for the cost function of the online optimization algorithm.

Chapter Summary

This chapter discussed the coordination of two major manipulated variables (radiant power and speed of the moving actuator) of robotic radiation-based processes. First, the coordination was addressed for the open-loop case, in which the radiant power and the speed were treated as constants during the process. A static optimization algorithm was developed to determine the values of the radiant power and the speed that can minimize the energy cost and processing time, subject to some defined state and input constraints. The results of the open-loop coordination were then incorporated into a closed-loop rule-based coordinated control strategy to achieve improved disturbance rejection performance. Given the online estimated process states, the radiant power and the speed of the actuator were coordinated by some designed rules around nominal values obtained from the open-loop coordination. Finally, a distributed model predictive control (MPC) strategy was developed to achieve online optimal coordination of the two manipulated variables. The distributed MPC strategy was formulated as a quadratic programming problem within a moving prediction horizon. Essential constraints on the control input and input change were also integrated into the MPC formulation. Simulation studies illustrated the implementation of the three coordination methods to a robotic UV curing process.

CHAPTER SIX

CONCLUSIONS AND FUTURE WORK

6.1 Conclusions

This dissertation presented a framework of control and estimation for processes actuated with moving radiant sources commonly applied in robotic configurations. The framework included three fundamental parts: 1) integration of trajectory generation with feedback control; 2) online state and parameter estimation; 3) multi-variable control coordination and process optimization. The framework provides a way to systematically address major challenges associated with these processes from both the theoretical and practical aspects.

A process-feature based online trajectory generation strategy was developed to deal with the time consuming calibration involved in traditional trial-and-error methods and the disturbance-rejection issue faced by most open-loop robotic radiation-based processes. In addition to a baseline trajectory design performed offline, the proposed trajectory generation strategy can adjust the motion of the robot manipulator in real time, using essential process features extracted from available measurements. Two practical approaches (named "look-and-move" and "run-by-run"), corresponding to different sensor configurations, were designed as the first sets of the online trajectory generation strategies. Moreover, an output feedback control method was proposed to enhance the online trajectory generation by continuously adjusting either the radiant power or the speed of the actuator, according to measured process outputs obtained from sensors either collocated or non-collocated with the actuator. Both the online trajectory generation and

the output feedback control strategies were then demonstrated through simulation studies on a robotic UV paint curing process. It was shown that these closed-loop control methods can successfully maintain temperature uniformity on the processed target in the presence of various disturbances. An experimental platform was also developed for further validation of these strategies and methods. Preliminary experiments implementing the "look-and-move" approach to the robotic UV curing process demonstrated the potential of the online trajectory generation strategy in maintaining temperature uniformity on the processed target.

Recognizing that robotic radiation-based processes are inherently and correctly modeled as distributed-parameter processes, further work was conducted posing the problems as such. A unified framework was first established for a 1D generalization of the processes in which the moving actuator was treated as a radiant point source operating on a spatially large strip-type target. It was shown how the generalized formulation could be utilized to describe different robotic radian-based processes (e.g. curing, drying) resolved into three simultaneous parts: energy transmission to target, state evolution for dominant process dynamics and co-evolution of measurable states.

Using the unified framework, a distributed state and parameter estimation scheme was proposed to compensate for the lack of direct sensing alternatives for some significant process states and parameters. In particular, a dual extended Kalman filter (DEKF) was developed to achieve online estimation of key process states and unknown parameters in parallel. To reduce the computational cost and take into account the changing observability distribution accompanying the actuator's movement, the

developed full-dimensional DEKF was further broken into a set of distributed local filters with an activating policy. These distributed local DEKFs were activated sequentially following the moving actuator to provide estimates of states and parameters of areas (on the target strip) where the dominant process evolution occurs. The distributed state and parameter estimation scheme was then demonstrated on a 1D robotic UV curing process and the simulation results showed that this scheme provided a good estimation of the actual process state in the presence of system and measurement noises, with the help of simultaneous estimation of unknown parameters and an appropriate design of the activating policy that compensates for the changing observability.

The dissertation also addressed the coordination of multiple manipulated variables for these robotic radiation-based processes to ensure quality and optimization. This issue was addressed progressively from three different levels, involving open-loop coordination, rule-based coordinated feedback control, and distributed-parameter model predictive control (MPC). In the open-loop coordination, the two major manipulated variables (speed and radiant power) were treated as constant during the process, and the values of the two variables were determined by solving a static optimization problem offline, considering energy cost, process efficiency and essential process and actuation constraints. A rule-based feedback control strategy was then developed to coordinate the radiant power and the speed of the actuator in a closed-loop manner, using the online estimated process states and some designed control rules. The two manipulated variables were adjusted simultaneously around the nominal values obtained from the open-loop coordination or static optimization.

Finally, a distributed model predictive control strategy was developed and investigated for systematically coordinating the manipulated variables in an online optimization framework using updated estimation of process states. The distributed MPC was formulated as a constrained quadratic programming problem, using future process states predicted from current state estimates and a linearized process model in order to determine the sequence of control input changes that can optimize the defined performance indexes.

Simulation studies were conducted on the robotic UV curing process to demonstrate the three coordination approaches. It was shown that the distributed MPC strategy integrated both the optimal and closed-loop characteristics from the other two approaches and enabled the effective coordination of these manipulated variables to achieve improved process performances and reduced control input costs.

6.2 Future Work

There are many possible future directions that can be pursued based on the formulation presented in this dissertation.

- This work focused on addressing state changes in the direction of the motion of the radiant actuator. The online trajectory generation and output feedback control strategies could be extended to the cross-directional case as well. Some work in this area has been discussed in [114] for cross-directional control of sheet and film processes. Such considerations for radiant source actuated processes have not yet been addressed.

- The distributed state and parameter estimation schemes could also be used for processes in which the diffusion terms are retained for both the state evolution and co-evolution phases. For these applications, two issues should be considered in designing the activating policy. First, any local DEKF within the activating window requires information from the adjacent DEKFs to perform the estimation due to the diffusion effect. This may be handled by incorporating off-diagonal terms into the state transition matrix of a subsystem consisting of those activated local DEKFs to address the diffusion effect. Second, the two boundaries (left and right) of the activating window have significant influences on the estimation accuracy of the DEKFs within the activating window. One possible approach is to set the left boundary as the previous estimates provided by the DEKF near the left end of the activating window, while to set the right boundary as the initial process state since the areas on the right of the activating window haven't yet been significantly illuminated by the radiant actuator.
- In this research, the process model was linearized for use in this first work on the distributed MPC strategy for processes employing moving radiant actuators. In future work, the nonlinear process models could be incorporated within a distributed (nonlinear) MPC framework and the solutions should be compared with the present work for any potential advantages.
- The moving radiant actuator considered in this first research was simplified to a single radiant point source. Future work can investigate the case where the moving actuator contains multiple radiant point sources (such as LEDs) that are

independently controllable. This new structure not only enables the manipulation of the total power level of the actuator, but it also gives the opportunity to control the spatial distribution of the radiant power emitted from the actuator. These potential advantages may help achieve even further flexibility in process control extending the estimation and control strategies developed in the present work.

APPENDIX A

Derivation of the Equality Constraint Equation for the Open-Loop Coordination Implemented to the 1D Robotic UV Curing Process

The objective of this appendix is to derive the equality constraint equation involved in the open-loop coordination to describe the relationship between the radiant power and the speed given the desired cure-conversion level. The following derivation will use both the energy transmission and state transition equations of the 1D robotic UV curing process.

The energy transmission phase of the robotic UV curing process can be represented as follows:

$$I(x,t) = \frac{k}{\pi}\varphi(t)\frac{d_0^2}{\left\{\left[\int_0^t v_a(\tau)d\tau - x\right]^2 + d_0^2\right\}^2} \tag{A.1}$$

In equation (A.1), the irradiance distribution on the target strip (I) is described as a nonlinear function of the radiant power (φ), the speed (v_a), and the absorption coefficient (k). In the open-loop coordination, since the radiant power and speed of the actuator is treated as constant during the whole process, equation (A.1) can be further simplified as:

$$I(x,t) = \frac{k}{\pi}\varphi\frac{d_0^2}{\left[\left(v_a t + x_0 - x\right)^2 + d_0^2\right]^2} \tag{A.2}$$

Here, x_0 denotes the initial position where the actuator starts moving. Then the associated energy distribution on the target strip can be calculated by:

$$\begin{aligned} E(x,t) &= \int_0^t \frac{k}{\pi}\varphi \frac{d_0^2}{\left[\left(v_a\tau - L_x\right)^2 + d_0^2\right]^2}\, d\tau \\ &= \frac{k}{2\pi}\frac{\varphi}{v_a}\left\{\frac{1}{d_0}\left(\arctan\frac{v_a t - L_x}{d_0} + \arctan\frac{L_x}{d_0}\right) + \frac{v_a t - L_x}{\left(v_a t - L_x\right)^2 + d_0^2} + \frac{L_x}{\left(L_x\right)^2 + d_0^2}\right\} \end{aligned} \tag{A.3}$$

$$L_x = x - x_0 \tag{A.4}$$

Given equation (4.10), the curing dynamics can be expressed as:

$$\begin{aligned} \frac{d[M](x,t)}{dt} &= \eta_1'[M](x,t)\left[I(x,t)\ \right]^{0.5} e^{\eta_2'\int_0^t I(x,\tau)d\tau} \\ &= \eta_1'[M](x,t)\left[I(x,t)\ \right]^{0.5} e^{\eta_2' E(x,t)} \end{aligned} \tag{A.5}$$

$$\eta_1' = -\kappa\left\{\phi\varepsilon[PI](x,t_0)\right\}^{0.5}, \quad \eta_2' = -\frac{1}{2}\phi\varepsilon \tag{A.6}$$

The differential equation in (A.5) can be further transformed into:

$$\frac{1}{[M](x,t)}d[M](x,t) = \eta_1'\left[I(x,t)\ \right]^{0.5} e^{\eta_2' E(x,t)}\ dt \tag{A.7}$$

Integrating both sides of equation (A.7) from 0 to t_f yields:

$$\begin{aligned} \ln\left(\frac{[M](x,t_f)}{[M](x,t_0)}\right) &= \int_0^{t_f} \eta_1'\left[I(x,t)\ \right]^{0.5} e^{\eta_2' E(x,t)}\ dt \\ &= \eta_1' f_1(x,t) e^{\eta_2' E(x,t)}\Big|_0^{t_f} - \eta_1'\int_0^{t_f} f_1(x,t) e^{\eta_2' E(x,t)} \eta_2' I(x,t)\ dt \end{aligned} \tag{A.8}$$

$$f_1(x,t) = \left(\frac{k}{\pi}\right)^{0.5} \frac{\varphi^{0.5}}{v_a}\left(\arctan\frac{v_a t - L_x}{d_0} + \arctan\frac{L_x}{d_0}\right) \tag{A.9}$$

In equation (A.9), $f_1(x,t)$ can be approximated by using the following piecewise function:

$$f_1(x,t) \approx \begin{cases} 0, & 0 \le t < \dfrac{L_x}{v_a} \\ \mu, & \dfrac{L_x}{v_a} \le t \le t_f \end{cases} \tag{A.10}$$

$$\mu = \left(\frac{k}{\pi}\right)^{0.5} \frac{\varphi^{0.5}}{v_a}\left(\arctan\frac{v_a t_f - L_x}{d_0} + \arctan\frac{L_x}{d_0}\right) \tag{A.11}$$

Given the above approximation of $f_1(x,t)$, the integral equation (A.8) can be calculated by:

$$\begin{aligned} &\ln\left(\frac{[M](x,t_f)}{[M](x,t_0)}\right) \\ &= \eta_1' f_1(x,t) e^{\eta_2' E(x,t)}\Big|_0^{t_f} - \eta_1' \int_0^{t_f} f_1(x,t) e^{\eta_2' E(x,t)} \eta_2' I(x,t)\, dt \\ &\approx \eta_1'\left[\mu e^{\eta_2' E(x,t_f)} - 0\right] - \eta_1'\left[\int_0^{L_x/v_a} 0 e^{\eta_2' E(x,t)} \eta_2' I(x,\tau)\, dt + \int_{L_x/v_a}^{t_f} \mu e^{\eta_2' E(x,t)} \eta_2' I(x,t)\, dt\right] \\ &= \eta_1' \mu e^{\eta_2' E(x,t_f)} - \eta_1'\left[0 + \mu e^{\eta_2' E(x,t)}\Big|_{L_x/v_a}^{t_f}\right] \\ &= \eta_1' \mu\left[e^{\eta_2' E(x,t_f)} - e^{\eta_2' E(x,t_f)} + e^{\eta_2' E(x,L_x/v_a)}\right] \\ &= \eta_1' \mu e^{\eta_2' E(x,L_x/v_a)} \end{aligned} \tag{A.12}$$

Then, the final monomer concentration distribution can be represented as:

$$[M](x,t_f) = [M](x,t_0) e^{f_2(x)} \tag{A.13}$$

$$f_2(x) = \eta_1' \mu e^{\eta_2' E(x,L_x/v_a)} = \eta_1'\left(\frac{k}{\pi}\right)^{0.5} \frac{\varphi^{0.5}}{v_a}\left(\arctan\frac{v_a t_f - L_x}{d_0} + \arctan\frac{L_x}{d_0}\right) e^{\eta_2' E(x,L_x/v_a)} \tag{A.14}$$

$$E(x, L_x / v_a) = \frac{k}{2\pi} \frac{\varphi}{v_a} \left[\frac{1}{d_0} \left(\arctan \frac{L_x}{d_0} \right) + \frac{L_x}{\left(L_x\right)^2 + d_0^2} \right] \tag{A.15}$$

The derivative of final monomer concentration distribution $[M](x, t_f)$ with respect to the spatial coordinate x can be represented as:

$$\frac{d[M](x, t_f)}{dx} = [M](x, t_0) e^{f_2(x)} \frac{df_2(x)}{dx} \tag{A.16}$$

$$\frac{df_2(x)}{dx} = \frac{d\left[\eta_1' \mu e^{\eta_2' E(x, L_x / v_a)} \right]}{dx} = \eta_1' e^{\eta_2' E(x, L_x / v_a)} \left[\frac{d\mu}{dx} + \mu \eta_2' \frac{dE(x, L_x / v_a)}{dx} \right] \tag{A.17}$$

$$\frac{d\mu}{dx} = \left(\frac{k}{\pi} \right)^{0.5} \frac{\varphi^{0.5}}{v_a} \left[\frac{-d_0}{\left(v_a t_f - L_x\right)^2 + d_0^2} + \frac{d_0}{\left(L_x\right)^2 + d_0^2} \right] \tag{A.18}$$

$$\frac{dE(x, L_x / v_a)}{dx} = \frac{k}{2\pi} \frac{\varphi}{v_a} \left[\frac{1}{\left(L_x\right)^2 + d_0^2} + \frac{d_0^2 - \left(L_x\right)^2}{\left[\left(L_x\right)^2 + d_0^2\right]^2} \right] \tag{A.19}$$

Equations (A.18) and (A.19) can be further represented as:

$$\frac{d\mu}{dx} = \left(\frac{k}{\pi} \right)^{0.5} \frac{\varphi^{0.5}}{v_a} \left[\frac{-\beta_1}{\frac{d_0}{\beta_1}\left(1 + \beta_1^2\right)} + \frac{\beta_2}{\frac{d_0}{\beta_2}\left(1 + \beta_2^2\right)} \right] \tag{A.20}$$

$$\frac{dE(x, L_x / v_a)}{dx} = \frac{k}{\pi} \frac{\varphi}{v_a} \left\{ \frac{\left(\frac{\beta_2}{d_0}\right)^2}{1 + \left(\beta_2\right)^2} + \frac{\left(\beta_2\right)^2 - 1}{\left(\frac{d_0}{\beta_2}\right)^2 \left[1 + \left(\beta_2\right)^2\right]^2} \right\} \tag{A.21}$$

$$\beta_1 = \frac{d_0}{v_a t_f - L_x}, \quad \beta_2 = \frac{d_0}{L_x} \tag{A.22}$$

Since the normal distance (d_0) between the actuator and the target strip is much smaller than the length of the target strip, the following conditions are usually fulfilled except that the actuator is closed to the initial (x_0) and final positions ($x_0 + v_a t_f$).

$$\beta_1 \ll \qquad \ll \tag{A.23}$$

Then, equation (A.20) and (A.21) can be further simplified as:

$$\frac{d\mu}{dx} = \left(\frac{k}{\pi}\right)^{0.5} \frac{\varphi^{0.5}}{v_a} \frac{\beta_2^2 - \beta_1^2}{d_0} \tag{A.24}$$

$$\frac{dE(x, L_x / v_a)}{dx} = \frac{k}{\pi} \frac{\varphi}{v_a} \left\{ \frac{\left(\frac{\beta_2}{d_0}\right)^2}{1} + \frac{-1}{\left(\frac{d_0}{\beta_2}\right)^2 1} \right\} = 0 \tag{A.25}$$

Then the derivative of $[M](x, t_f)$ with respect to x can be simplified as:

$$\begin{aligned} \frac{d[M](x,t_f)}{dx} &= [M](x,t_0) e^{f_2(x)} \frac{df_2(x)}{dx} \\ &\approx [M](x,t_0) e^{f_2(x)} \eta_1' e^{\eta_2' E(x, L_x/v_a)} \frac{d\mu}{dx} \\ &= [M](x,t_0) e^{f_2(x)} \eta_1' e^{\eta_2' E(x, L_x/v_a)} \left(\frac{k}{\pi}\right)^{0.5} \frac{\varphi^{0.5}}{v_a} \frac{\beta_2^2 - \beta_1^2}{d_0} \end{aligned} \tag{A.26}$$

$$\beta_1 = \frac{d_0}{v_a t_f - L_x}, \quad \beta_2 = \frac{d_0}{L_x} \tag{A.27}$$

Given the parameters listed in Table 4.2, the numerical value of the derivative term is small, so the final monomer concentration distribution is almost uniform under the open-loop curing with constant radiant power and speed. Therefore, the following

equation is used to describe the relationship between the desired cure-conversion level and the required radiant power and speed that can achieve this objective.

$$\alpha_d = \frac{[M](x_m, t_0) - [M](x_m, t_f)}{[M](x_m, t_0)} = \frac{[M]_0 - [M](x_m, t_f)}{[M]_0} = 1 - e^{f_2(x_m)} \tag{A.28}$$

$$f_2(x_m) = \eta_1' \mu e^{\eta_2' E(x_m, L_x / v_a)} = \eta_1' \left(\frac{k}{\pi}\right)^{0.5} \frac{\varphi^{0.5}}{v_a} \left(2 \arctan \frac{L_t}{2d_0}\right) e^{\eta_2' E(x_m, L_{x_m} / v_a)} \tag{A.29}$$

$$E(x_m, L_{x_m} / v_a) = \frac{k}{2\pi} \frac{\varphi}{v_a} \left[\frac{1}{d_0}\left(\arctan \frac{L_t}{2d_0}\right) + \frac{2L_t}{(L_t)^2 + 4d_0^2}\right] \tag{A.30}$$

Here, the desired cure-conversion level is denoted by α_d. It is calculated by using the monomer concentration at the position x_m, which is in the middle of the region $[x_0, x_0 + L_t]$ on the target strip. The total moving distance is represented by L_t ($L_t = v_a t_f$). Equations (A.28) ~ (A.30) describe the equality constraint for the radiant power (φ) and the speed (v_a) of the actuator under a certain desired cure-conversion level (α_d).

REFERENCES

1. U.S. Department of Energy, Energy Information Administration, 2008 Annual Energy Review, June, 2009.

2. U.S. Department of Energy, "Energy Information Administration, "Emissions of greenhouse gases in the United States 2008", December, 2009.

3. U.S. Environment Protection Agency, "Energy trends in selected manufacturing sectors: Opportunities and challenges for environmentally preferable energy outcomes", March, 2007.

4. Vogt, M., "Infrared drying lowers energy costs and drying times", *Plastics, Additives and Compounding*, 9(5), September/October, 2007, pp. 58-61.

5. Dhib, R., "Infrared drying: From process modeling to advanced process control", *Drying Technology*, 25(1), January 2007, pp. 97-105.

6. Zhang, M., Tang, J., Mujumdar, A.S., and Wang, S., "Trends in microwave-related drying of fruits and vegetables", *Trends in Food Science and Technology*, 17(10), October 2006, pp. 524-534.

7. Hagood, D., Kelly, M., "Extolling the advantages of UV-Curing processes", *Metal Finishing*, 106(4), April 2008, pp. 71-74.

8. Kinoshita, S., "Basics and applications of UV/EB curing technology", *Journal of Photopolymer Science and Technology*, 19(1), 2006, pp. 93-98.

9. Pasternack, G., "Curing at the speed of light: an end users guide for UV/EB technology", *Metal Finishing*, 103(1), January, 2005, pp 28-37.

10. Dworak, J., "Laser-welding technologies. Results of investigations and possible applications", *Welding International*, 21(1), January 2007, pp. 5-11.

11. Penasa, M. and Rivela, C., "State of the art applications of aluminum alloy laser welding", *Welding International*, 21(6), June 2007, pp. 404-411.

12. U.S. Department of Energy, Office of Industrial Technologies, Energy Efficiency and Renewable Energy, "Progressive powder coating: New infrared curing oven at metal finishing plant increases production by 50%" (BestPractices Case Study), 2003.

13. U.S. Department of Energy, Office of Industrial Technologies, Energy Efficiency and Renewable Energy, "UV-Curable coatings for aluminum can production" (Chemicals Project Fact Sheet), 1999.

14. Mills, P., "Robotic UV Curing Saves Time and Money". *Metal Finishing*, 104(4), April, 2006, pp. 43-49.

15. Raith, T., Bischof, M., Deger, M., and Gemmler, E., "3-D UV technology for OEM coatings". In RadTech Europe 2001 Conference Papers Archive, 2001.

16. Kang, H.-S., Suh, J., and Cho, T.-D., "Study on robot application technology for laser welding", in Proceedings of the 2008 International Conference on Smart Manufacturing Application, 2008, pp. 354-356.

17. Hardt, D.E., "Modeling and control of manufacturing processes: Getting more involved", *Transactions of the ASME. Journal of Dynamic Systems, Measurement and Control*, 115(2B), June 1993, pp. 291-300.

18. Butkovskii, A.G., Pustyl'nikova, E.I., "Theory of mobile control of distributed parameter systems", *Automation and Remote Control*, 41(6), pt.1, June 1980, pp. 741-747.

19. Butkovskii, A.G., Kubyshkin, V.A., Tverdokhlebov, E.S., and Chubarov, E.P., "The implementation of distributed control functions by using mobile control sources", *Automation and Remote Control*, 44(4), pt.1, April 1983, pp. 411-417.

20. Khapalov, A.Y., "Mobile point controls versus the locally distributed ones for the controllability of the semilinear parabolic equation", in Proceedings of the 2002 IEEE Conference on Decision and Control, v3, 2002, pp. 3384-3389.

21. Vayena, O., Doumanidis, H., Demetriou, M.A., "An LQR-based optimal actuator guidance in thermal processing of materials", in Proceedings of the 2000 American Control Conference, v4, 2000, pp. 2300-2304.

22. Demetriou, M.A. and Iftime, O.V., "Finite horizon optimal control of switched distributed parameter systems with moving actuators", in Proceedings of the 2005 American Control Conference, v6, 2005, pp. 3912-3917.

23. Demetriou, M.A., "Guidance of a moving collocated actuator/sensor for improved control of distributed parameter systems", in Proceedings of the 2008 IEEE Conference on Decision and Control, 2008, pp. 215-220.

24. Demetriou, M.A. and Kazantzis, N., "A new integrated output feedback controller synthesis and collocated actuator/sensor scheduling framework for distributed parameter processes", *Computers & Chemical Engineering*, 29(4), March 2005, pp. 867-876.

25. Demetriou, M.A., Paskaleva, A., Vayena, O., and Doumanidis, H., "Scanning actuator guidance scheme in a 1-D thermal manufacturing process", *IEEE Transactions on Control Systems Technology*, 11(5), September, 2003, pp. 757-764.

26. Huissoon, J.P., Strauss, D.L., Rempel, J.N., Bedi, S., and Kerr, H.W., "Multi-variable control of robotic gas metal arc welding", *Journal of Materials Processing Technology*, 43(1), Jun 1994, pp. 1-12.

27. Song, J.-B. and Hardt, D.E., "Closed-loop control of weld pool depth using a thermally based depth estimator", *Welding Research Supplement*, October, 1993, pp. 471-478.

28. Moore, K.L., Naidu, D.S., Yender, R., and Tyler, J., "Gas metal arc welding control: Part I : Modeling and analysis", *Nonlinear Analysis, Theory, Methods and Applications*, 30(5), December 1997, p 3101-3111.

29. Chen, H., Lv, F., Lin, T., and Chen, S., "Closed-loop control of robotic arc welding system with full-penetration monitoring", *Journal of Intelligent and Robotic Systems: Theory and Applications*, 56(5), 2009, pp. 565-578.

30. Doumanidis, C.C., "Multiplexed and distributed control of automated welding", *IEEE Control Systems Magazine*, 14(4), August, 1994, pp. 13-24.

31. Doumanidis, C.C. and Kwak, Y.-M., "Multivariable adaptive control of the bead profile geometry in gas metal arc welding with thermal scanning", *International Journal of Pressure Vessels and Piping*, 79(4), April, 2002, pp. 251-262.

32. Doumanidis, C.C. and Hardt, D.E., "Multivariable adaptive control of thermal properties during welding", *Transactions of the ASME. Journal of Dynamic Systems, Measurement and Control*, 113(1), March 1991, pp. 82-92.

33. Suzuki, A., Hardt, D.E., and Valavani, L., "Application of adaptive control theory to on-line GTA weld geometry regulation", *Transactions of the ASME. Journal of Dynamic Systems, Measurement and Control*, 113(1), March 1991, pp. 93-103.

34. Seelinger, M.J., Robinson, M., Dieck, Z., and Skaar, S.B., "A vision-guided, semi-autonomous system applied to a robotic coating application", in Proceedings of the SPIE - The International Society for Optical Engineering, v3209, 1997, p p. 133-144.

35. Omar, M., Viti, V., Saito, K., and Liu, J., "Self-adjusting robotic painting system", *Industrial Robot*, 33(1), 2006, pp. 50-55.

36. Jones, P.D.A., Duncan, S.R., Rayment, T., and Grant, P.S., "Control of temperature profile for a spray deposition process", *IEEE Transactions on Control Systems Technology*, 11(5), September, 2003, pp. 656-667.

37. Zeng, G. and Hemami, A., "An adaptive control strategy for robotic cutting", in Proceedings of the 1997 IEEE International Conference on Robotics and Automation, v1, 1997, pp. 22-27.

38. Liu, J. and Li, L., "In-time motion adjustment in laser cladding manufacturing process for improving dimensional accuracy and surface finish of the formed part", *Optics and Laser Technology*, 36(6), September 2004, pp. 477-483.

39. Allwood, J.M., Music, O., Raithathna, A., Duncan, S.R., "Closed-loop feedback control of product properties in flexible metal forming processes with mobile tools", *CIRP Annals - Manufacturing Technology*, 58(1), 2009, pp. 287-290.

40. Dochain, D., "State and parameter estimation in chemical and biochemical processes: a tutorial", *Journal of Process Control*, 13(8), 2003, pp. 801-818.

41. Rega, G., "Dimension reduction of dynamical systems: Methods, models, applications", *Nonlinear Dynamics*, 41(1-3), August, 2005, pp. 1-15.

42. Antoulas, A.C., Sorensen, D.C., and Gugercin, S., "A survey of model reduction methods for large scale systems", *Contemporary Mathematics*, v280, AMS Publications, 2001, pp. 193–219.

43. Rafaralahy, H., Boutayeb, M., Darouach, M., and Krzakala, G., "Exponential state observer for a class of distributed parameter systems via generalized orthogonal polynomials", in Proceedings of the 1993 IEEE Conference on Decision and Control, v2, 1993, pp. 1864-1865.

44. Lilly, J.H., "Finite-dimensional adaptive observers applied to distributed parameter systems", *IEEE Transactions on Automatic Control*, 38(3), March, 1993, pp. 469-474.

45. Alaeddine, M. and Doumanidis, C.C., "Distributed parameter thermal system control and observation by Green-Galerkin methods", *International Journal for Numerical Methods in Engineering*, 61(11), November, 2004, pp. 1921-1937.

46. Shvartsman, S.Y., Theodoropoulos, C., Rico-Martínez, R., Kevrekidis, I.G., Titi, E.S., and Mountziaris, T.J., "Order reduction for nonlinear dynamic models of distributed reacting systems", *Journal of Process Control*, 10(2), April, 2000, pp. 177-184.

47. Christofides, P.D. and Daoutidis, P., "Finite-dimensional control of parabolic PDE systems using approximate inertial manifolds", in Proceedings of the 1997 IEEE Conference on Decision and Control, v2, 1997, pp. 1068-1073.

48. Soroush, M., "State and parameter estimations and their applications in process control", *Computers & Chemical Engineering*, 23(2), 1998, pp. 229-245.

49. Soucy, K.A. and Holt, B.R., "Modeling, estimation and control of polymer composite processing", in Proceedings of the 1990 American Control Conference v2, 1990, pp. 1650-1655.

50. Olanrewaju, M.J. and Al-Arfaj, M.A., "Estimator-based control of reactive distillation system: Application of an extended Kalman filtering", *Chemical Engineering Science*, 61(10), May, 2006, pp. 3386-3399.

51. Xiong, R., Wissmann, P.J., and Gallivan, M.A., "An extended Kalman filter for in situ sensing of yttria-stabilized zirconia in chemical vapor deposition", *Computers & Chemical Engineering*, 30(10-12), September, 2006, pp. 1657-1669.

52. Velardi, S.A., Hammouri, H., and Barresi, A.A., "In-line monitoring of the primary drying phase of the freeze-drying process in vial by means of a Kalman filter based observer", *Chemical Engineering Research and Design*, 87(10), October, 2009, pp. 1409-1419.

53. Lendek, Z., Babuska, R., and De Schutter, B., "Distributed Kalman filtering for cascaded systems", *Engineering Applications of Artificial Intelligence*, 21(3), April, 2008, pp. 457-469.

54. Li, R., Corripio, A.B., Henson, M.A., and Kurtz, M.J., "On-line state and parameter estimation of EPDM polymerization reactors using a hierarchical extended Kalman filter", *Journal of Process Control*, 14(8), 2004, pp. 837-852.

55. Rezaei, N., Rahimpour, M.R., Khayatian, A., and Jahanmiri, A., "A new hybrid approach in the estimation of end-states of a tubular plug-flow reactor by Kalman filter", *Chemical Engineering & Processing: Process Intensification*, 47(5), May, 2008, pp. 770-779.

56. Dochain, D., Perrier, M., and Ydstie, B.E., "Asymptotic observers for stirred tank reactors", *Chemical Engineering Science*, 47(15-16), October-November, 1992, pp. 4167-4177.

57. Hulhoven, X., Vande Wouwer, A., and Bogaerts, Ph., "State observer scheme for joint kinetic parameter and state estimation", *Chemical Engineering Science*, 63(19), October,. 2008, pp. 4810-4819.

58. Haykin, Simon S., Kalman filtering and neural networks, John Wiley and Sons, 2001.

59. Moireau, P., Chapelle, D., and Le Tallec, P., "Joint state and parameter estimation for distributed mechanical systems", *Computer Methods in Applied Mechanics and Engineering*, 197(6-8), January, 2008, pp. 659-677.

60. Van Lint, H., Hegyi, A, and Hoogendoorn, S.P., "Dual EKF state and parameter estimation in multi-class first-order traffic flow models", in IFAC Proceedings Volumes, 17(1), 2008.

61. Wenzel, T.A., Burnham, K.J., Blundell, M.V., and Williams, R.A., "Dual extended Kalman filter for vehicle state and parameter estimation", Vehicle *System Dynamics*, 44(2), February, 2006, pp. 153-171.

62. Wan, E.A. and Nelson, A.T., "Neural dual extended Kalman filtering: Applications in speech enhancement and monaural blind signal separation", in Proceedings of the 1997 IEEE Signal Processing Society Workshop, 1997, pp. 466-475.

63. Chen, T., Morris, J., and Martin, E., "Particle filters for state and parameter estimation in batch processes", *Journal of Process Control*, 15(6), September, 2005, pp. 665-673.

64. Sawo, F., Klumpp, V., and Hanebeck, U.D., "Simultaneous state and parameter estimation of distributed-parameter physical systems based on sliced Gaussian mixture filter", in Proceedings of the 2008 International Conference on Information Fusion, 2008.

65. Damak, T., "Procedure for asymptotic state and parameter estimation of nonlinear distributed parameter bioreactors", *Applied Mathematical Modeling*, 31(7), July, 2007, pp. 1293-1307.

66. Dufour, P., Touré, Y., Blanc, D., and Laurent, P., "On nonlinear distributed parameter model predictive control strategy: On-line calculation time reduction and application to an experimental drying process", *Computers and Chemical Engineering*, 27(11), November, 2003, pp. 1533-1542.

67. Dufour, P., Michaud, D.J., Touré, Y., and Dhurjati, P.S., "A partial differential equation model predictive control strategy: Application to autoclave composite processing", *Computers and Chemical Engineering*, 28(4), April, 2004, pp 545-556.

68. Shang, H., Forbes, J. F., and Guay, M., "Characteristics-based model predictive control of distributed parameter systems", in Proceedings of the 2002 American Control Conference, v6, 2002, pp. 4383-4388.

69. Shang, H., Forbes, J.F., Guay, M., "Model Predictive Control for Quasilinear Hyperbolic Distributed Parameter Systems", *Industrial and Engineering Chemistry Research*, 43(9), April, 2004, pp. 2140-2149.

70. Aggelogiannaki, E. and Sarimveis, H., "Nonlinear model predictive control for distributed parameter systems using data driven artificial neural network models", *Computers and Chemical Engineering*, 32(6), June, 2008, pp 1233-1245.

71. Bernard, T., and Moghaddam, E. E., "Nonlinear model predictive control of a glass forming process based on a finite element model", in Proceedings of the 2006 IEEE International Conference on Control Applications, 2006, pp. 960-965.

72. Dubljevic, S., Christofides, P.D., and Kevrekidis, I.G., "Distributed nonlinear control of diffusion-reaction processes", *International Journal of Robust and Nonlinear Control*, 14(2), January, 2004, pp. 133-156.

73. Qian, K. and Zhang, Y., "Optimal model predictive control of plasma pipe welding process", in Proceedings of the 2008 IEEE Conference on Automation Science and Engineering, 2008, pp. 492-497.

74. Potocnik, P. and Grabec, I., "Nonlinear model predictive control of a cutting process", *Neurocomputing*, 43, 2002, pp. 107-126.

75. Chen, J., Ettelaie, R., Yang, H. and Yao, L., "A novel technique for in situ measurements of stress development within a drying film", *Journal of Food Engineering*, 92(4), June, 2009, pp. 383-388.

76. Maffezzoli, A., Quarta, E., Luprano, V.A.M., Montagna, G., and Nicolais, L., "Cure monitoring of epoxy matrices for composites by ultrasonic wave propagation", *Journal of Applied Polymer Science*, 73(10), September, 1999, pp. 1969-1977.

77. Biernacki, J.M., and Beall, F.C., "Acoustic monitoring of cold-setting adhesive curing in wood laminates", *International Journal of Adhesion and Adhesives*, 16(3), 1996, pp. 165-172.

78. Nakashima, Y., Kamimuki, K., Nakabayashi, T., and Yoshida, K, "Development of in-process monitoring technique in YAG laser welding", in Proceedings of the the International Society for Optical Engineering, v4831, 2003, pp. 160-164.

79. Zhang, Y., Wang, L., Wu, Q., and Hu, D., "Dynamic monitoring studies for high speed mechanical manufacturing process", in Proceedings of the International Society for Optical Engineering, v6279, January, 2007, p 62794Q-1-7.

80. Cusano, A., Breglio, G., Giordano, M., Calabro, A., Cutolo, A., and Nicolais, L., "Optoelectronic characterization of the curing process of thermoset-based composites", *Journal of Optics A: Pure and Applied Optics*, 3(2), March, 2001, pp. 126-130.

81. Kwon, J.W., Chin, W.S., and Lee, D.G., "In situ cure monitoring of adhesively bonded joints by dielectrometry", *Journal of Adhesion Science and Technology*, 17(16), 2003, pp. 2111-2130.

82. Bang, K.G., Kwon, J.W., Lee, D.G., and Lee, J.W., "Measurement of the degree of cure of glass fiber-epoxy composites using dielectrometry", *Journal of Materials Processing Technology*, 113(1-3), June, 2001, pp. 209-214.

83. Yasui, T., Yasuda, T., Sawanaka, K., and Araki, T., "Terahertz paintmeter for noncontact monitoring of thickness and drying progress in paint film", *Applied Optics*, 44(32), November, 2005, pp. 6849-6856.

84. Portoghese, F., Berruti, F., and Briens, C., "Continuous on-line measurement of solid moisture content during fluidized bed drying using triboelectric probes", *Powder Technology*, 181(2), February, 2008, pp. 169-177.

85. Decker, C. and Moussa, K., "Real-time monitoring of ultrafast curing by UV-radiation and laser beams", *Journal of Coatings Technology*, 62(786), July, 1990, pp. 55-61.

86. Scherzer, T., Mehnert, R., and Lucht, H., "On-line monitoring of the acrylate conversion in UV photopolymerization by near-infrared reflection spectroscopy", Macromolecular Symposia, v205, January, 2004, pp. 151-162.

87. Mirapeix, J., Cobo, A., Cubillas, A.M., Conde, O.M., and Lopez-Higuera, J.M., "Efficient processing technique based on plasma optical spectroscopy for on-line welding quality monitoring", in Proceedings of the International Society for Optical Engineering, v7003, 2008, p 70030Q-1-8.

88. BenAmor, S., Colombié, D., and McKenna, T., "Online reaction calorimetry. Applications to the monitoring of emulsion polymerization without samples or models of the heat-transfer coefficient", *Industrial and Engineering Chemistry Research*, 41(17), August, 2002, pp. 4233-4241.

89. Chen, J.H., Johnston, A., Petrescue, L., and Hojjati, M., "A novel calorimetry technique for monitoring electron beam curing of polymer resins", *Radiation Physics and Chemistry*, 75(2), February, 2006, pp. 336-349.

90. Wikle III, H.C, Chen, F., Nagarajan, S., and Chin, B.A, "Survey of infrared sensing techniques for welding process monitoring and control," *Journal of the Chinese Institute of Engineers*, 21(6), November, 1998, pp. 645-657.

91. Al-Habaibeh, A. and Parkin, R., "An autonomous low-cost infrared system for the on-line monitoring of manufacturing processes using novelty detection", *International Journal of Advanced Manufacturing Technology*, 22(3-4), 2003, pp. 249-258.

92. Zeng, F., Ayalew, B., and Omar, M. A., "Robotic automotive paint curing using thermal signature feedback", *Industrial Robot: An International Journal*, 36(4), 2009, pp. 389-395.

93. Zeng, F., Ayalew, B., and Omar, M. A., "Cure-feature based online trajectory generation in a robotic paint curing system", In Proceedings of the 2009 American Control Conference, 2009, pp. 2006-2011.

94. Paul, R.P., Robot Manipulators: Mathematics, Programming, and Control, MIT Press, Cambridge, MA, 1982.

95. Sciavicco, L., and Siciliano, B., Modeling and Control of Robot Manipulators, Springer, London, UK, 2001.

96. Zeng, F., Ayalew, B., and Omar, M. A., "Control of a robotic UV curing process with thermal vision feedback through two IR cameras", In Proceedings of the 2009 ASME International Mechanical Engineering Congress & Exposition, 10, 2009, pp. 217-225.

97. Ashdown, I., Radiosity: A Programmer's Perspective, John Wiley and Sons, New York, NY, 1994.

98. Modest, M.F., Radiative Heat Transfer, McGraw Hill, New York, NY, 1993.

99. Cañavate, J., Colom, X., Pagès, P., and Carrasco, F., "Study of the curing process of an epoxy resin by FTIR spectroscopy", *Polymer-Plastics Technology and Engineering*, 39(5), November, 2000, pp. 937-943.

100. Kim, H.D. and Kim, T.W., "Preparation and properties of UV-curable polyurethane acrylate ionomers", *Journal of Applied Polymer Science*, 67(13), March, 1998, pp. 2153-2162.

101. Hong, W., Lee, Y.T., and Gong, H., "Thermal analysis of layer formation in a stepless rapid prototyping process", *Applied Thermal Engineering*, 24(2-3), February, 2004, pp. 255-268.

102. Goodner, M.D. and Bowman, C.N., "Development of a comprehensive free radical photopolymerization model incorporating heat and mass transfer effects in thick films", *Chemical Engineering Science*, 57(5), March, 2002, pp. 887-900.

103. Lin, Y.L., Li, S.J., Zhu, Y., Bingol, G., Pan, Z., and McHugh, Tara H., "Heat and mass transfer modeling of apple slices under simultaneous infrared dry blanching and dehydration process", *Drying Technology*, 27(10), October, 2009, pp. 1051-1059.

104. Jia, D. and Afzal, M.T., Modeling of moisture diffusion in microwave drying of hardwood", *Drying Technology*, 25(3), March, 2007, pp. 449-454.

105. Haykin, S.S., Kalman filtering and neural networks, John Wiley and Sons, New York, NY, 2001.

106. Wan, E.A. and Nelson, A.T., "Neural dual extended Kalman filtering: applications in speech enhancement and monaural blind signal separation", Neural Networks for Signal Processing VII., in Proceedings of the 1997 IEEE Signal Processing Society Workshop, 1997, pp. 466-475.

107. Zeng, F., Ayalew, B., "Online distributed state and parameter estimation for feedback control of a curing process", American Control Conference, Baltimore, MD, USA, June 30-July 2, 2010 (in press).

108. Zeng, F. and Ayalew, B., "Estimation and coordinated control for distributed-parameter processes with a moving radiant actuator", *Journal of Process Control*, 20(6), 2010, pp. 743-753.

109. Zeng, F. and Ayalew, B., "Model predictive control of a distributed parameter process employing a moving radiant actuator", ASME Dynamic Systems and Control Conference, Cambridge, MA, USA, September 13-15, 2010 (accepted).

110. Camacho, E.F. and Bordons, C., Model Predictive Control, Springer, London, UK, 2004.

111. Maciejowski, J. M., Prediction Control: with Constraints. Prentice Hall, Upper Saddle River, NJ, USA, 2002.

112. Eduardo, G.-I. and Hiram, M.-R., "Fuzzy multivariable control of a class of a biotechnology process", in Proceedings of the IEEE International Symposium on Industrial Electronics, 1999, pp. 419-424.

113. Tsai, C.-H., Hou, K.-H., and Chuang, H.-T., "Fuzzy control of pulsed GTA welds by using real-time root bead image feedback", *Journal of Materials Processing Technology*, 176(1-3), June, 2006, pp. 158-167.

114. Braatz, R.D., VanAntwerp, J.G., Featherstone, A.P., and Ogunnaike, B.A., "Cross-directional control of sheet and film processes", *Automatica*, 43(2), February, 2007, pp. 191-211.